MODELLING EVAPORATION FROM WETLAND LICHEN AND MOSS TUNDRA IN CHURCHILL, MANITOBA

XIANG LIU

Modelling Evaporation from Wetland Lichen and Moss Tundra in Churchill, Manitoba

By

© Xiang Liu

Supervisor: Dr. Ken Snelgrove

A thesis submitted to the
School of Graduate Studies
in partial fulfilment of the
requirements for the degree of
Master of Engineering
Faculty of Engineering & Applied Science
Memorial University of Newfoundland
January 2009
St. John's Newfoundland

Abstract

Today northern subarctic terrestrial environments are receiving increased attention due to their hydrologic effects not only on subarctic terrain but on the whole global water cycle. Evaporation is a pronounced factor consisting of a portion of the energy and water balances. Predicting evaporation is becoming one of the most important fields of research in hydrological and climatological analysis. This thesis describes the simulation of evaporation from a wetland lichen and moss tundra in Churchill, Manitoba.

The models used are the Canadian Land Surface Scheme– CLASS and the Penman-Monteith model. In both models, the canopy resistance needs to be corrected to account for non-vascular vegetation, whose evapotranspiration depends only on canopy moisture. The plotted results show that both the modified models perform comparably in the simulation of the evaporation.

The data for the simulations are from two weather stations in Churchill: Fen and Rail Spur. All the components of the energy balance are modelled at Fen, and the results from CLASS show good fits to the measurements. Longwave radiation is successfully modelled at Rail Spur by associating the degree of cloud cover with weather conditions.

Acknowledgments

I hereby sincerely thank my supervisor Professor Ken Snelgrove. Dr. Snelgrove gave me great support in the entire research course, directing modelling, discussing results and revising the thesis. Additionally, he offered me funding from the ArcticNet Research during my studies. These greatly helped me to be committed to my research and finally finish this thesis.

Together, I would also like to acknowledge the contributions of the following individuals to the development of my thesis:

Dr. Tim Papakyriakou, Associate Professor of the University of Manitoba, provided all the data used for modelling, including the two weather stations: Fen and Rail Spur. He recommended a number of useful papers and to use reasonable methods for the comparison of results.

Dr. Richard Bello, Associate Professor of York University, provided important information for the non-vascular plants – lichens and mosses growing in the examined area.

Kyle Swystun, Masters Student of the University of Manitoba, provided detailed information on measurements, instruments, and field environments at the Fen site.

The people shown above as well as Dr. Snelgrove are working on ArcticNet Project 3.2: The Hudson Bay Coastal Zone in a Changing Climate System. Dr. Papakyriakou is the leader of this Project. They have given great help and support to my research.

Table of Contents

List of Figures

List of Tables

Symbols

α – reflectivity or surface albedo
Λ – vapour pressure gradient with temperature
Λe – air vapour pressure deficit
ΛS – storage change
ε – surface emissivity
γ – psychrometric constant
φ_s – soil moisture suction at saturation
λ_v – latent heat of vaporization
θ_{lim} – residual soil water content
θ_p – porosity
ρ_a – mass density of air
ρ_w – mass density of water
σ – Stefan-Boltzmann constant
ξ – absorptivity
ψ – transmissivity
b – soil texture parameter
C – the degree of cloud cover
c_a – heat capacity of air
C_{at} – atmospheric conductance for water vapour
C_{can} – canopy conductance
d – index of agreement
D – canopy dryness index
e^* – saturation vapour pressure
E – evapotranspiration
e_a – atmospheric vapour pressure
ET – evapotranspiration rate
k – ground coverage
k_s – hydraulic conductivity
K - shortwave radiation
K^* – net shortwave radiation
L – longwave radiation
L^* – net longwave radiation
m – average for the period of measurement
p – atmospheric pressure
P – precipitation

Q^* – net radiation
Q_E – sensible heat
Q_G – ground heat
Q_H – latent heat
r – stomatal resistance
R – runoff
R_a – gas constant for air
R_c – canopy resistance
S – actual amount of water stored in canopy
S_m – maximum amount of water hold in canopy
T – soil temperature
T_a – air temperature
v_a – wind speed, , and
W_a – relative humidity
z_0 – roughness height of the surface
z_d – zero-plane displacement
z_m – the height at which wind speed and air vapour pressure measured
z_{veg} – heith of vegetation
Z – soil layer thichness

Abbreviations

AGB – above ground biomass
ANUDEM – Australian National University Digital Elevation Model
BATS – Biosphere-Atmosphere Transfer Scheme
CLASS – Canadian Land Surface Scheme
CNSC – Churchill Northern Studies Center
CO_2 – carbon dioxide
CSAT3 – three-dimensional sonic anemometer
DEM – Digital Elevation Model
EGM – Earth Gravitational Model
EROS – Earth Resources Observation and Science
GCM - General Circulation Model
IRGA – infrared gas analyzer
LAI – leaf area index
LI – licor
MBE - mean bias error
NAD 27 – North American Datum of 1927
NAD 83 – North American Datum of 1983
NTDB – National Topographic Data Base
PAR – photosynthetically active radiation
RMSE – root mean square error
RTG – RiverTools grid
SiB – Simple Biosphere Scheme
SRTM – Shuttle Radar Topography Mission
USGS – U. S. Geological Survey
VPD – vapour pressure deficit
WGS 84 – World Geodetic System 1984
WSC – Water Survey of Canada

1. Introduction

A large proportion of land in the Northern Hemisphere is covered by wetland surfaces, 14% of the land area in Canada compared to less than 4% worldwide. A wetland is defined as an ecosystem where water persists at, near, or above the mineral soil surface for a long enough period of time to promote the development of particular soil and vegetation types adapted to the wet environment (Tarnocai, 1980). Vegetated wetlands are a common feature in the circumpolar tundra belt of the Northern Hemisphere, especially extensive in the Hudson Bay Lowland of Canada (Wessel and Rouse, 1994), where a present study area of about 54 000 km^2 has an almost continuous cover of forested and tundra wetland (Mortsch, 1990). Churchill, Manitoba, known as the accessible arctic, is located along the southern edge of Canada's arctic and is part of the Hudson Bay coastal lowlands (Figure 1.1) that are undergoing a detailed assessment of the impact of climate change on watershed processes (Papakyriakou, n.d.). The vegetation cover in Churchill is sparse and the predominant land types are grasses, sedges, shrubs, forest and tundra comprising more than 400 species of plants: vascular

and non-vascular (Town of Churchill, n.d.). Most wetlands are dominated by organic soils, principally peat, which is accumulated as the production of plant material exceeds the decomposition rate due to the high water content and cool temperatures, and contain a significant coverage of non-vascular plants.

Figure 1.1 Location of Churchill, Manitoba, in a general map of Northern Canada. From Geology.com (2008).

The impacts of climate change are potentially greatest in high latitudes (Kattenberg et al., 1996), and may be especially severe for the sensitive wetland ecosystems found in Canada's subarctic and Hudson Bay Lowland (Rizzo and Wiken, 1992; Rouse, 1998; Rouse et al., 1997). The current generation of global climate models indicates that this region will experience large increases in temperature, changes in precipitation amount, and patterns associated with elevated levels of greenhouse gas (Papakyriakou, n.d.). Therefore, it is important to begin testing and refining the ability of land surface models to simulate the exchanges of moisture and energy over these complex surfaces dominated by wetland tundra plants. Evaporation as a major component

of both the energy and water balances has prompted the development of physically-based models (Wessel and Rouse, 1994), such as Temperature-Based models (Hamon, 1963; Malmstrom, 1969; Thornthwaite, 1948), Radiation-Based models (Slatyer and McIlroy, 1961), Pan-Based models (Kohler et al., 1955; Linsley et al., 1982), and the Penman-Monteith combination model (Monteith, 1965; Penman, 1948). The primary advantage of these models is their potential to predict the hydrological, meteorological and physiological responses to a variety of hypothetical climate change scenarios (Wessel and Rouse, 1994). However, evaporation model estimates and field measurements vary widely as each model has their limitations and disadvantages in testing naturally vegetated areas, particularly for those areas lacking information concerning vegetation types. Intercomparison of simulation results becomes an effective approach to providing a better assessment of the model.

Reliable estimates of evaporation depend on accurate input parameters, which are observed and measured in the field, but not all the required parameters are available. The missing parameters are calculated to make them usable to the model. In Churchill, many types of equipment are installed for various research. The weather stations of interest to this thesis are Fen and Rail Spur (train mile marker 467), since they have adequate parameter datasets, but missing and unavailable data still exist at these sites. Hence, relatively continuous datasets from the Fen site were chosen, and the missing data are filled by linear interpolation. The longwave radiation fluxes that are not measured at the Rail Spur site, are obtained by combining the clear-sky longwave radiation calculations with the degree of cloud cover.

The purpose of this thesis is to model evaporation from the wetland non-vascular—lichen and moss—tundra, whose evapotranspiration does not rely on insolation, temperature, vapor pressure deficit, or carbon dioxide (CO_2) concentration, and is only a function of canopy moisture (Bello, November 5, 2007). This requires modifying the canopy resistance in the model to fit the characteristics of lichen and moss, in order to improve the understanding and the prediction of evapotranspiration in wetland tundra for the Churchill region.

The models used are the Canadian Land Surface Scheme (CLASS) for the energy balance and the Penman-Monteith model for evaporation. CLASS was developed in the late 1980s for the Canadian General Circulation Model (GCM), in response to the perceived need for a "second-generation" land surface model which would adequately treat the effects of vegetation, snow and soil on exchanges of heat and moisture with the atmosphere (Verseghy, 2000). To provide comparison with CLASS, measured data at Fen are used, and for Rail Spur, where the latent heat measurement is not available, the Penman-Monteith model is applied to intercompare the results. The Penman-Monteith combination model, developed by Penman (1948) and modified by Monteith (1965), simulates evaporation from a surface covered by a closed canopy of vascular plants treated as a single large leaf such that all stomata within the canopy act in parallel. Since CLASS does not take non-vascular plants into account, and neither does the Penman-Monteith model, a canopy resistance formula for lichens was added to run both models. However, this supplement needs to be further investigated in future work.

It is important that land surface parametrization schemes be assessed against a wide range of high quality field measurements in order to evaluate parameters that may be necessary to describe the soil and vegetation and to test the performance of the model under an ensemble of different conditions (Bailey et al., 2000). An examination of energy balance closure is an indispensable tool of evaluating data. As the measured energy balance at Fen is not closed because of measurement biases in each of the sensors, the Bowen-ratio approach (Bowen, 1926) is applied to calculate the heat flux terms. These fluxes are intercompared with the values from CLASS and the Penman-Monteith model. After testing at the Fen site, it is found that the result from CLASS is acceptable for representing the evaporation from the wetland tundra, although the Fen site is primarily composed of grass, while Rail Spur is made up of lichen and moss. Consequently, CLASS and the Penmen-Monteith model are compared with each other.

The remainder of this thesis includes six chapters. Chapter 2 demonstrates the three main models: energy balance, water balance, and CLASS. Chapter 3 introduces the Deer River basin and its watershed delineation. Chapter 4 illustrates the application of CLASS to the Fen site and the comparison of the results with the measurements. Chapter 5 discusses the determination of longwave radiation for the Rail Spur site based on the degree of cloud cover. Chapter 6 discusses the modified CLASS model for lichen and moss tundra. Chapter 7 gives a summary of this research and future work. The thesis closes with two appendixes. Appendix A shows a sample of data for CLASS, and Appendix B provides a set of comparative figures of soil temperatures for each soil layer.

2. Literature Review

Evapotranspiration is a collective term for all the processes by which water in the liquid or solid phase at or near the earth's land surfaces becomes atmospheric water vapor (Dingman, 2002). In the global water cycle, water is a medium that links the atmosphere and the earth, moving through various portions of the hydrologic cycle and transferring energy and heat from one physical phase to another. Evaporation, the main course of water transformation between the atmosphere and the surface, impacts regional cycles as well as the global cycle. There are two fundamental cycles of importance in understanding atmospheric systems (Oke, 1987): the cycles of solar energy and water, that is, energy and water balances. They will be described in detail in the following two sections, respectively.

The land surface areas of the Earth represent significant sources, sinks and reservoirs of heat and moisture with respect to the atmosphere; the evaluation of land-atmosphere transfers of energy and water is therefore an important component of any general circulation model (Verseghy, 1991). CLASS, which began in 1987, is a land

surface model that treats the effects of vegetation, snow and soil on exchanges of heat and moisture with the atmosphere (Verseghy, 2000). After decades of development it successfully estimates turbulent flux for several wetland types incorporating organic soil parameters. A general overview of CLASS including its history and future will be presented in the last section of this chapter.

2.1 Energy Balance

Radiation is the main form of energy emission from the Sun. This includes shortwave, longwave, microwave and other wavelengths. The processes by which solar radiation is transformed into earth radiation are the critical determinants of the earth's climate (Dingman, 2002). Most of the solar radiation is absorbed or reflected by the atmosphere, and only a very small portion, with wavelength approximately from 0.1 to 100 μm, is able to travel through the atmospheric system. During its passage through the atmosphere, solar radiation encounters clouds and other atmospheric constituents including water vapour, salt crystals, dust particles and various gases (Oke, 1987). The rest of the energy arriving at the surface is even smaller after the absorption and reflection. Hence, atmospheric scientists designated that incoming solar radiation is shortwave radiation (K) in the range 0.15 - 0.3 μm. On the other hand, the constituents of the atmosphere emit radiation as well, as all bodies whose temperatures are above absolute zero possess energy. The radiation emitted by atmospheric bodies is longwave radiation (L), in the range 3.0 - 100 μm.

The earth's surface can reflect and absorb the incident energy but there is no transmission through it. The proportions transmitted, reflected and absorbed, expressed as

ratios of the incident energy, are defined to be the transmissivity (ψ), the reflectivity (α) and the absorptivity (ξ). The total is unity.

$$\psi + \alpha + \xi = 1 \tag{2.1}$$

For the earth's surface, an opaque non-black body whose transmissivity is zero (i.e. $\psi = 0$),

$$\alpha + \xi = 1 \tag{2.2}$$

where α is referred to as the surface albedo, ranging from 0 to 1. It is low for water and high for snow. For wetland tundra, it is about 0.05 - 0.2.

According to Kirchhoff's Law, which holds that at the same temperature and wavelength good absorbers are good emitters (Oke, 1987), it was assumed that for an opacity $\xi = \varepsilon$, where ε is the surface emissivity. Finally,

$$\alpha + \varepsilon = 1 \quad \text{or} \quad \alpha = 1 - \varepsilon \tag{2.3}$$

If the incoming shortwave radiation $K_{\downarrow}$ is known, the outgoing radiation $K_{\uparrow}$ should be $\alpha K_{\downarrow}$, so the net shortwave radiation (K^*) is:

$$K^* = K_{\downarrow} - K_{\uparrow} = (1 - \alpha)\, K_{\downarrow} \tag{2.4}$$

The incoming longwave radiation emitted by the atmosphere ($L_{\downarrow}$) in the absence of cloud depends upon the bulk atmospheric temperature and emissivity in accordance with the Stefan-Boltzmann Law (Oke, 1987). Longwave radiation will be described in greater depth in Chapter 5: Modelling Longwave Radiation. Similarly, the outgoing longwave radiation from the surface ($L_{\uparrow}$) is dependent on its temperature and emissivity. The net longwave radiation (L^*) is the difference between $L_{\downarrow}$ and $L_{\uparrow}$:

$$L^* = L_{\downarrow} - L_{\uparrow} \tag{2.5}$$

The sum of the net longwave and shortwave radiation is called the net radiation (Q^*), which represents the limit to the available energy source or sink.

$$Q^* = K^* + L^* \tag{2.6}$$

The relationship between energy flow and the climate can be illustrated in a simple formula:

$$\text{Energy Input} = \text{Energy Output} \tag{2.7}$$

according to the First Law of Thermodynamics – conservation of energy – energy can be neither created nor destroyed, only converted from one form to another. In cases where there is a change in the net energy stored, the formula becomes:

$$\text{Energy Input} = \text{Energy Output} + \text{Energy Storage Change} \tag{2.8}$$

This equation is more suitable for most natural systems, especially for those over short periods. However, simulations for modelling natural climatology usually run over a longer period of time (e.g. a year or more), so that they can accurately represent the phenomena. The first equality is valid when values are integrated over a long time assuming no storage change, and when any differences are small, energy fluxes are compared instead of energy. For most energy balance models, the surface is assumed to be an infinitely thin layer that cannot store heat.

The earth-atmosphere system is a closed system, which indicates it is closed to the import or export of energy or mass, but there are exchanges of energy with the external space. The radiant energy emitted by the Sun is the sole input to the system. The net radiation flux is not the end result of the radiation budget but also the basic input to the surface energy balance (Oke, 1987). To make the system equivalent, there must be

energy being transferred away from the surface, that is, sensible (Q_H) or latent heat (Q_E) with the atmosphere, and ground heat (Q_G) with the soil. Sensible heat is a form of energy that can be sensed as a temperature change, while latent heat enables a substance to change the physical state by being released or absorbed at the same temperature, for example, water to water vapour. These are turbulent transfers: the parcels of air (eddies) in the atmosphere transport energy and mass from one location to another. This process is called convection. It provides the means of transport and mixing. Ground heat is the conductive exchange of sensible heat with the ground for warming or cooling the soil and melting the snow pack during the melt season. This belongs to thermal conduction: heat is transmitted within a substance by the collision of rapidly moving molecules. Thus the surface energy balance becomes:

$$Q^* = Q_H + Q_E + Q_G \quad (2.9)$$

$$\text{or} \quad K^* + L^* = Q_H + Q_E + Q_G \quad (2.10)$$

where all terms are fluxes, in the unit of W m^{-2}.

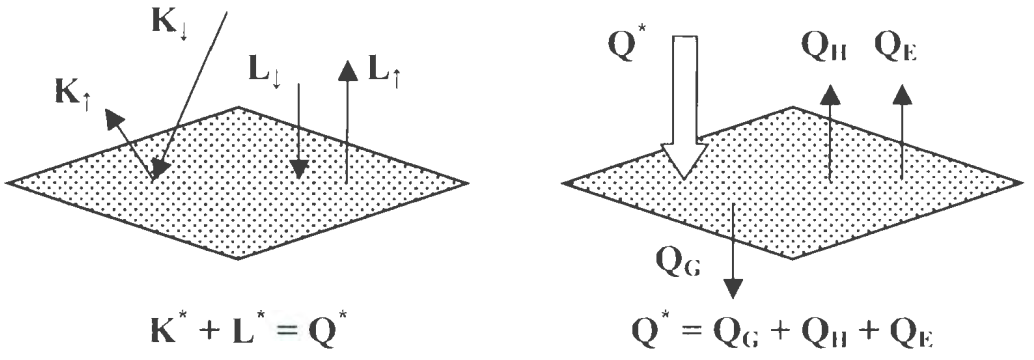

Figure 2.1 Schematic summary of the fluxes involved in the radiation budget and energy balance of an ideal site by day. From Oke (1987).

Figure 2.1 provides a schematic summary of the terms involved in the surface radiation and energy budgets. The sign convention employed is that radiative fluxes (i.e. K and L) directed into the surface are positive while non-radiative fluxes (i.e. Q_H, Q_E, and Q_G) directed away from the surface are positive.

2.2 Water Balance

Water is an important climatological substance with a number of unusual properties: high heat capacity, existence in all three phases at normal atmospheric temperatures, very strong covalent bonds, asymmetric molecular structure, hydrogen bonding, and other anomalous physical and chemical characteristics. These properties make it common in the earth-atmosphere system. In changing between ice, water and water vapour, latent heat is taken up or liberated and as a result the energy and water balances become enmeshed (Oke, 1987).

Analogously, water flow in the earth-atmosphere system conforms to the conservation of mass, so the annual global cycle of water can be written in the water balance equation:

$$P = E + R + \Delta S \qquad (2.11)$$

where P is precipitation in liquid and solid forms to the surface, E is evapotranspiration to the atmosphere from all sources (i.e. open water, soil and vegetation), R is the runoff including ground water and surface stream flows, and ΔS is the change in all forms of storage (liquid and solid) over the time period. The units of all terms are in mm s^{-1}, which can be easily connected to the unit of energy fluxes. The water balance system is not a zero thickness surface as in the energy balance. Normally, all the soil layers are included

in the unsaturated zone. A schematic representation of these terms of the water balance is shown in Figure 2.2.

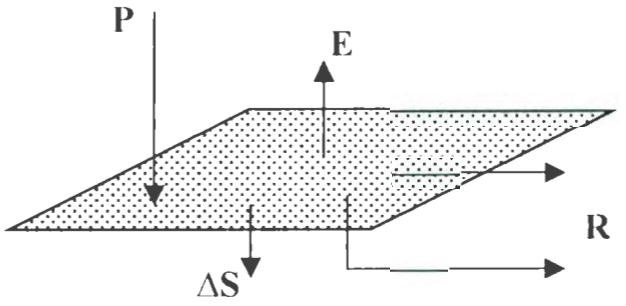

$$P = E + R + \Delta S$$

Figure 2.2 Schematic diagram of the components of the water balance of a natural surface.

All water enters the land phase of the hydrologic cycle as precipitation (Dingman, 2002). Globally, about 62% of the precipitation that falls on the continents is evapotranspired, amounting to 72,000 km^3 yr^{-1} (Shiklomanov and Sokolov, 1983). Of this, evaporation is always accompanied by latent heat transport, which is part of the energy balance. Heat energy is absorbed to break the hydrogen bonds when evaporation occurs, and it is released when the bonds are formed upon condensation. Therefore, evaporation is the common term in the water and energy balances. The fluxes of mass (E) and energy (Q_E) associated with evaporation are linked by the relation:

$$Q_E = \lambda_v E \tag{2.12}$$

where λ_v in J kg^{-1}, named the latent heat of vaporization, is the energy required to affect a change between liquid water and water vapour in unit mass. The units of E and Q_E can be

flux (W) or flux density (W m^{-2}). The energy flux is the rate of flow of energy (J s^{-1} = W), and flux density is the flux per unit area (m^2) of a plane surface. The value of λ_v is 2.48 at 10 °C, 2.45 at 20 °C and 2.43 at 30 °C in MJ kg^{-1}. To gain some insight into the energy amounts involved it should be realized that the energy locked-up in evaporating 1 kg of water is roughly equivalent to that necessary to raise 6 kg of water from 0 °C to 100 °C (Oke, 1987).

For hydrologic purposes, the mass flux density E is conveniently expressed in terms of an equivalent depth of water over time: mm s^{-1} or mm day^{-1}, which is then consistent with the regular unit of precipitation. The simple conversion:

$$1 \text{ mm s}^{-1}\ E = \lambda_v \text{ W m}^{-2}\ Q_E \tag{2.13}$$

$$\text{or} \quad 1 \text{ W m}^{-2}\ Q_E = \frac{1}{\lambda_v} \text{ mm s}^{-1}\ E \tag{2.14}$$

has been applied to the calculation between E with Q_E. Details of the conversion will be given in Chapter 6: Modelling Evaporation from Lichen and Moss Tundra.

2.3 CLASS Overview

CLASS is a physically-based numerical model developed at the Canadian Atmospheric Environment Service by Verseghy et al. (1991, 1993, 2000) for the Canadian GCM and used to evaluate the vertical transfer of energy and water between the land surface and three soil layers (Loukili et al., 2006). It belongs to the second-generation of land surface modelling schemes designed for use in atmospheric models. The history of CLASS can be dated from a few decades ago.

Land surface schemes specifically for use in large-scale climate applications first began to be developed for GCMs in the late 1960s (Manabe, 1969). At that time, GCMs had only a conceptually simple set of algorithms for the land surface due to limited computing power. In the 1980s, the land surface model in use in the Canadian GCM was fairly sophisticated for its time, incorporating the force-restore method for heat and the bucket approach for moisture, as well as the lumped treatment of vegetation and snow (Boer et al., 1984). With the increasing use of GCMs for climate change studies, numerous investigations have demonstrated that simulations of surface climate by GCMs are very much dependent on the formulation of their land surface schemes: e.g. with regard to the treatment of soil moisture and snow cover (Verseghy, 1991). Thus, efforts began among the GCM groups worldwide to develop so-called "second-generation" land surface models, which were characterized by more soil thermal and moisture layers (typically between two and four), and a separate treatment of the vegetation canopy (Verseghy, 2000). The first two land surface models of this type were the Biosphere-Atmosphere Transfer Scheme (BATS) (Dickinson et al., 1986), and the Simple Biosphere scheme (SiB) (Sellers et al., 1986).

Following those land surface models, CLASS was developed to simulate Canadian northern areas. The assessment of CLASS focuses on a number of important surface climate parameters, including net radiation, albedo, sensible and latent heat, canopy temperature, bulk stomatal resistance and soil moisture (Bailey et al., 2000). Compared to the old scheme, CLASS has many new characteristics: multiple soil layers, thermally and hydrologically separate vegetation cover and snow pack, snow pack as a

fourth "soil" layer, explicit soil infiltration and subgrid-scale spatial heterogeneity. Testing experiments have been carried out in coupled mode with GCMs. CLASS is shown to perform quite well, incorporating realistic treatments of snow and frozen soil processes for subarctic region of the northern hemisphere.

Table 2.1 traces the stages of development of CLASS over the past twenty years. Various refinements to the code have been implemented during this period, but the basic structure of the model remains unchanged. The latest version is 3.4 released in April 2008.

A schematic diagram of the model organization is presented in Figure 2.3. Each modelled grid cell can have up to four subareas, representing bare soil, vegetation covered, snow covered and snow-and-vegetation covered "patches" of the landscape (Verseghy, 2000). The energy and water balances are graphically described in this figure: the energy is from the Sun, travelling through the atmosphere and vegetation, arriving at the surface, and then part of the energy transmits to the deeper ground, while the other goes back to the atmosphere in the terms of sensible or latent heat; water is falling to the surface as precipitation, infiltrated to the subsurface, and then goes back to the atmosphere by evaporation and transpiration. CLASS treats the land surface as a composite of three main elements: vegetation, soil and snow (Bailey et al., 2000). The soil is divided into three layers for the purposes of heat and moisture transfer with thicknesses of 0.1, 0.25 and 3.75 m, respectively. Snow is modelled as analogous to a fourth, variable-depth "soil" layer, which is deep in the winter and becomes thinner during the melting season. Note that the runoff generated by soil drainage is included in the infiltration part.

Table 2.1 Development of CLASS Code. Modified from Verseghy (2008).

Version	Date of release	Major features and enhancements
1.0	April 1989	Basic thermal and hydrological model of soil and snow.
2.0	August 1991	Addition of thermal and hydrological model for vegetation.
2.1	May 1993	Full vectorization of code to enable efficient running on [vector] supercomputers.
2.2	April 1994	Augmentation of diagnostic calculations. Incorporation of in-line comments throughout the code. Development of an off-line, single-point, stand-alone version of the model
2.3	December 1994	Revisions to diagnostic calculations. Incorporation of new surface stability functions of Abdella and McFarlane (1996).
2.4	August 1995	Water budget diagnostic calculations completed. Preliminary parameterizations of rock and organic soils introduced. Code modifications to allow for inhomogeneity between soil layers. Incorporation of variable surface detention capacity.
2.5	January 1996	Completion of energy budget diagnostic calculations.
2.6	August 1997	Revisions to implementation of surface stability functions.
2.7	December 1997	Incorporation of variable soil permeable depth; calculation of soil properties based on texture; modified surface temperature iteration scheme.
3.0	December 2002	New soil evaporation parameters to fix underestimation; ability to handle thermal and hydraulic properties of organic soils; lateral flow of water in soils.
3.1	April 2005	Faster iteration scheme for surface and canopy temperatures; modification to snow interception and sublimation.
3.2	May 2006	Third layer can be subdivided into 7 finer layers; explicit treatment of liquid water content in snow pack; revised canopy transmission and aledo calculations.
3.3	December 2006	Separate temperature profile curve fit for snow and soil; multiple-layer option for ice sheets; water and energy balance checks for each time step; modifications to soil hydraulic conductivity calculations.
3.4	April 2008	Streamline and clean up code; updated soil thermal conductivity calculations; revisions to handling of water stored on vetetation.

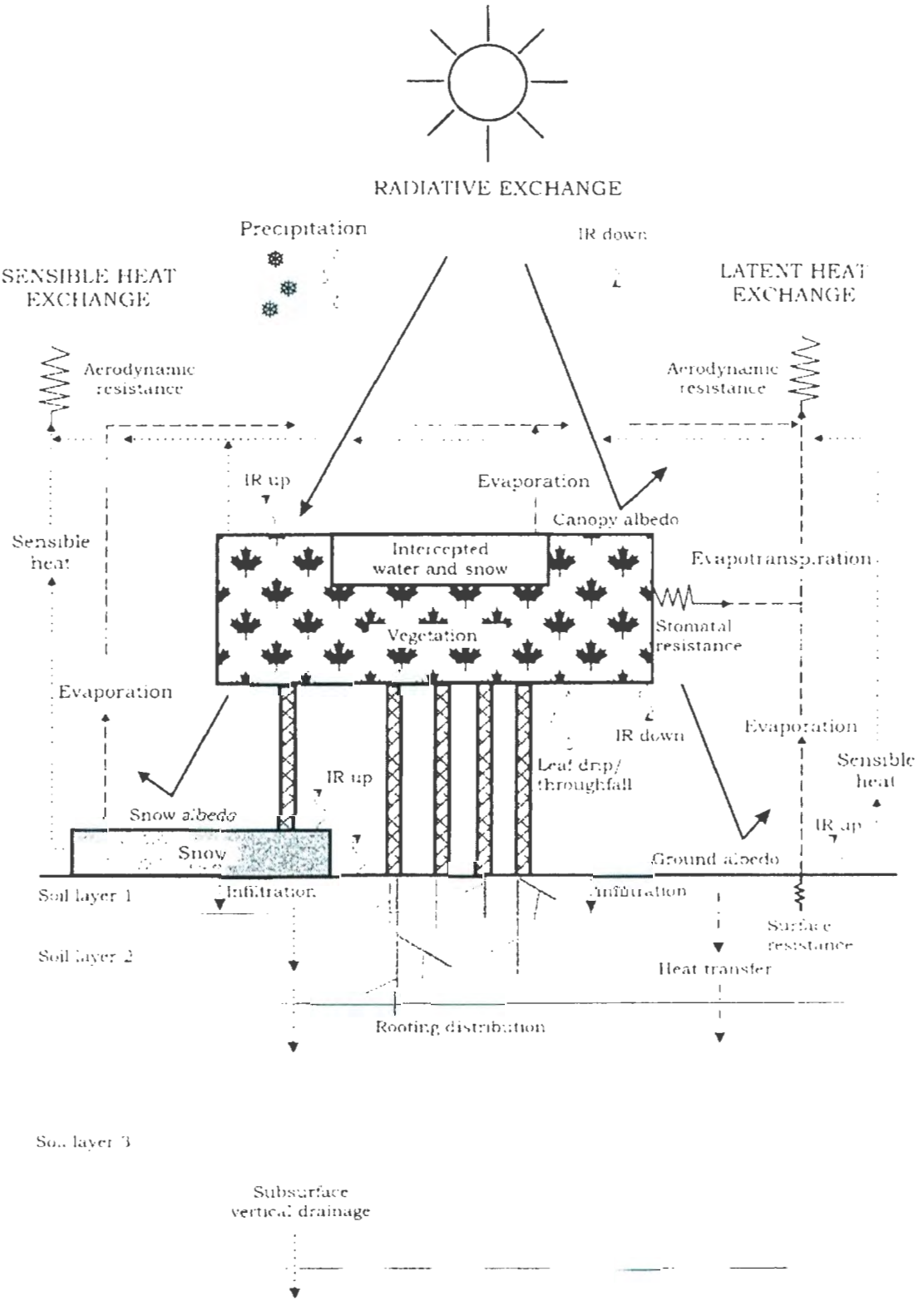

Figure 2.3 Schematic diagram of CLASS. From Verseghy (2000).

One of the significant modifications to CLASS is the inclusion of organic soil parameters used to define three different types: undecomposed fibric peat (highly permeable), an intermediate hemic peat and a deeply humified sapric peat. Given that the characteristics of peat vary with depth or humification, representative values of porosity and other thermal and hydraulic properties for each of three organic soil classes are required. Letts et al. (2000) determined the parameter values associated with the three organic soil types after thoroughly reviewing the literature on peat characteristics. Table 2.2 shows the hydraulic parameters for the three peat classes employed in CLASS.

Table 2.2 Hydraulic parameters for the three classes of peat used in the organic soils version of CLASS developed by Letts et al. (2000).

		Fibric	Hemic	Sapric
Hydraulic conductivity (m s^{-1})	k_s	2.8×10^{-4}	2.0×10^{-6}	1.0×10^{-7}
Porosity	θ_P	0.93	0.88	0.83
Residual soil water content	θ_{lim}	0.04	0.15	0.22
Suction at saturation (cm)	φ_s	1.03	1.02	1.01
Soil Texture parameter	b	2.7	6.1	12.0

In CLASS, vegetation is assigned to one of four major categories: coniferous trees, deciduous trees, crops and grass. The moisture transfer from these vegetation types is by the vascular pathway of root, stem and leaf, while evaporation from non-vascular plants is presently not included. For most vegetation, precipitation can fall directly through canopy gaps to the surface. Otherwise, the precipitation intercepted by canopy first fills the interception store until the capacity is exceeded, at which point any excess is

allowed to run off and drip to the ground. The water within canopy is either transpired from leaves or translocated through the stem to the ground. Of this, transpiration is controlled by the bulk canopy stomatal resistance, which is a function of leaf area index, incoming solar radiation, atmospheric vapour pressure deficit, temperature, and soil moisture tension (Verseghy, 2000).

To run CLASS, three input files are required: the parameter initialization file that contains the particulars of the site being investigated, the meteorological data file that includes seven variables, and a soil layer file. Chapter 4: CLASS Testing, will show the entire operation of CLASS for a specific site.

3. Deer River Basin Study Area

The Churchill region is situated on the west coast of Hudson Bay (Figure3.1). This locale is especially good for examining the northern Canadian landscape because most of the permafrost forms associated with subarctic conditions are not only found here but can be reached by the existing road network (Dredge, 1992). As an access to subarctic, it is strongly influenced by the Hudson Bay environment, which is extremely sensitive to global scale climate variability and change. Fully understanding the linkages with the heavily impacted southern watersheds and the role that water regulation plays in the processes of Hudson Bay is of practical significance.

There are many watershed drainage basins in the Churchill region, even though the land there is very flat and wet. A variety of studies on basin topography, geology, biology, ecosystem, climatology and hydrology have been carried out to manage the development of northern Manitoba. The Deer River, a tributary of the Churchill River, is of interest to our research. The station of Deer River North of Belcher at latitude 58° 0' 54" N and longitude 94° 11' 44" W is chosen as a basin outlet to delineate the Deer River

watershed from the U. S. Geological Survey (USGS) Digital Elevation Models (DEMs) with RiverTools software. The resulting watershed boundary is compared to published basin information from Water Survey of Canada ([WSC], 2007).

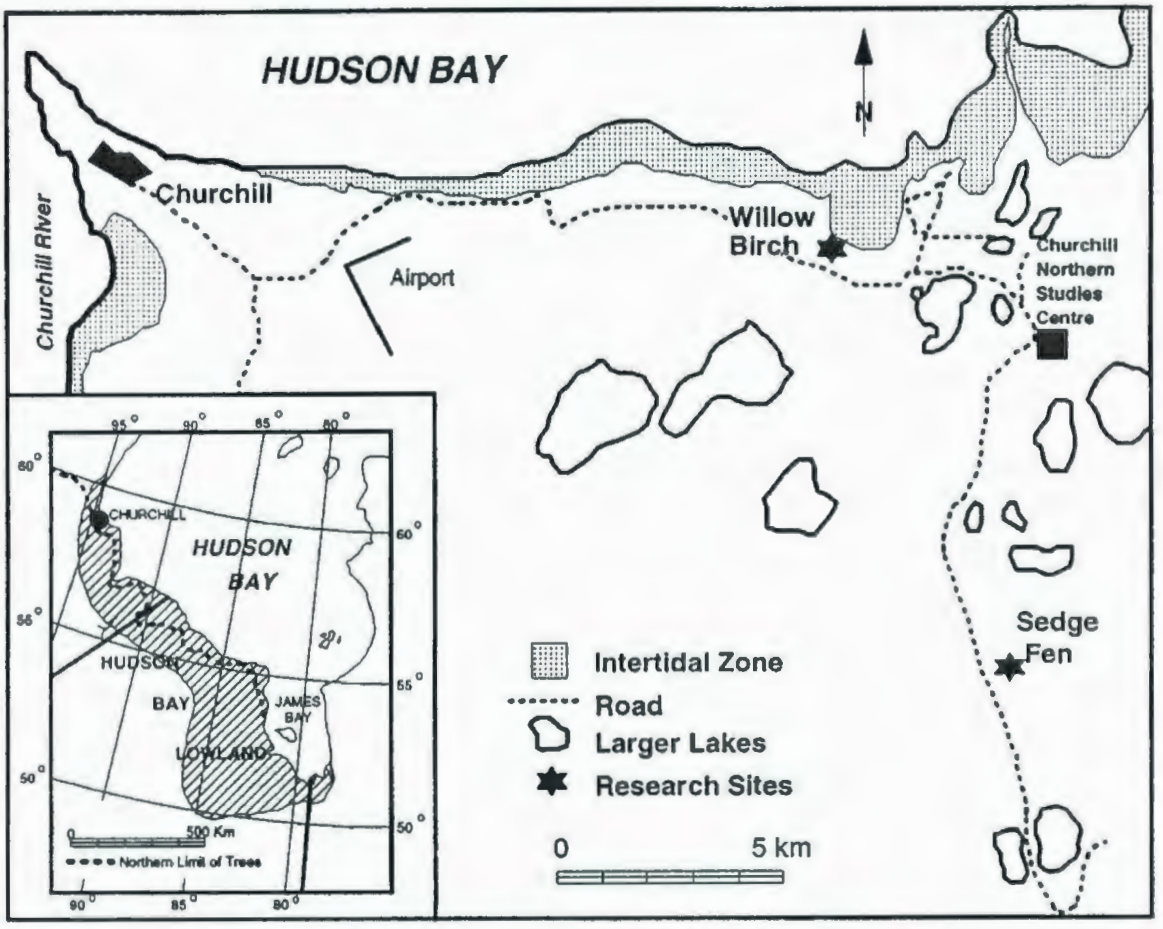

Figure 3.1 Location of Churchill, Manitoba, within the Hudson Bay Lowland (inset map) and the location of study sites. From Blanken and Rouse (1995).

3.1 Basin Description

The Deer River watershed basin, covering approximately 1890 km^2 (WSC, 2007), is a major sub-basin of Canada's largest watershed in subarctic Hudson Bay. It is located within the Churchill region near the Hudson Bay railway, with the basin outlet at Deer

River North of Belcher (Figure 3.2). Much of the terrain in this region gradually slopes downward inland toward the coast. Drainage is exceptionally poor because of the extremely flat land, low local relief and general impermeability of the fine grained, ice bonded substrate. Many streams flow in either shallow or poorly defined channels. Moreover, standing water covers more than 50% of the land surface in summer. However, permafrost features such as frost polygons, palsas, ice wedges, and hummocks and hollows caused by the growth or decay of ground ice, provide most of the microrelief in the area (Dredge, 1992). Figure 3.3 displays a group of photos of land coverage in the Deer River watershed basin, and gives a broad overview of those features in the Churchill region. The locations of the photos are marked on the map in Figure 3.2.

Churchill is a unique place where the natural environment extends from tundra to boreal forest and marine ecosystems, consisting largely of forest, peat plateau, fens, lakes and ponds. A tundra zone characterized by subarctic shrubs and scattered spruce covers the northeastern part of the region. Sphagnum and sedge peatlands supporting heath lichen and moss vegetation are widespread in coastal lowlands (Dredge, 1992). The treeline region is dominated by white spruce, although pine, birch, tamarack and alder are also common. Land is continually emerging from Hudson Bay through isostatic uplift and permafrost intrusion at a rate of about 40 cm per century (Hansell et al. 1983). The topography on the coastal side is flat and well drained, while inland, peat accumulation appears associated with the development of hummocks and thermokarst ponds.

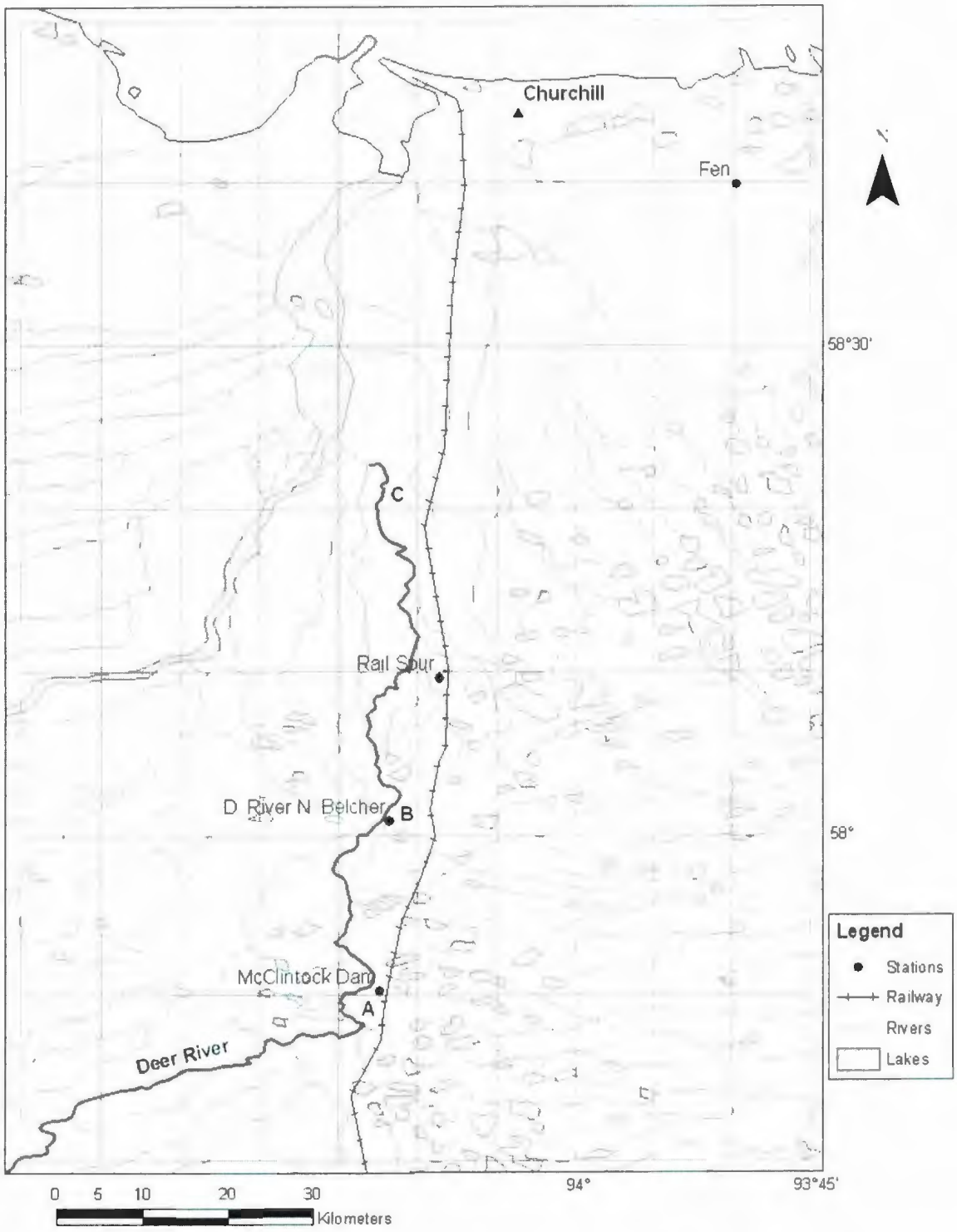

Figure 3.2 Map of the Churchill area showing lakes, rivers and the railway, and locations of flux and meteorological monitoring stations and stream monitoring stations. Map drawn using ArcGIS 9.1 and Global Data VMAP0.

A

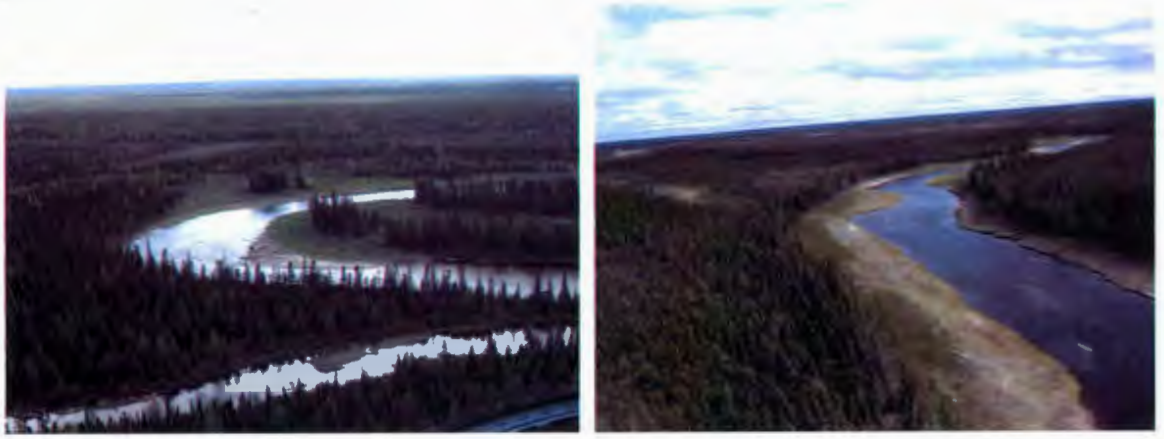

B

C

Figure 3.3 Land coverage in up- (A), mid- (B), and down-stream (C) regions in the Deer River watershed. Photos taken by Bing Chen and Liang Jin, in 2007. Locations are marked in Figure 3.2.

Churchill now experiences a marine subarctic wetland climate and is strongly influenced by air masses in Hudson Bay. The mean annual air temperature is -7.3 °C and daily means range between 12 °C for July and -28 °C for January. Average annual precipitation is 400 mm at the Churchill airport, while about half of the precipitation falls as snow. The prevailing winds are from the northwest in both winter and summer (Dredge, 1992). During the growing season, defined as days with the mean daily temperature greater than 5 °C, the 30-year mean daily temperature and total precipitation are 10.7 °C and 109 mm, respectively (Blanken and Rouse, 1995).

At Churchill, the average surface temperature of both rock and mineral soil is -2 °C to -4 °C, and the temperature change with seasons is not great. Most of area lies in the region of continuous permafrost. The thickness of permafrost is about 80 m, thickening inland and disappearing offshore. The depth of the active layer with seasonal thawing depends on the water content. It increases from about 50 cm in the relatively dry peat to 60 cm in moist peat, and to about 15 m in fens. Peat continues to accumulate each year, accompanied by an increase in permafrost thickness each winter.

3.2 Watershed Delineation

The Deer River watershed is delineated from the surrounding landscape using a 3 arc seconds USGS Digital Elevation Model (DEM) and an automated program: RiverTools software. This watershed delineation distinguishes areas that contribute solutes and water to the Deer River from those that contribute constituents to neighboring drainages. RiverTools extracts DEM data to predict water flow paths and channel networks for hydrologic modelling, and to determine the location of drainage basin boundaries.

Elemental watershed properties such as basin area and relief are defined for the Deer River after the delineation. Also, the watershed boundaries can be used to guide future sampling or experimental design by defining topographic, soil, land cover and precipitation of the basin.

3.2.1 Methods

Delineation of the Deer River watershed is performed with RiverTools using a USGS DEM. DEMs are gridded representations of the earth's surface with each grid cell assigned an elevation, and have the advantage of being continuous, regular surfaces (Kinner, 2000). DEM data is a uniform matrix of elevation values indexed to specific points on the ground. The USGS DEM data used for the Deer River watershed delineation was collected by the Shuttle Radar Topography Mission (SRTM) for Earth Resources Observation and Science (EROS). The horizontal datum is the World Geodetic System 1984 (WGS 84) and the vertical datum is mean sea level as determined by the WGS84 Earth Gravitational Model (EGM 96) geoid. The values are spaced 3 arc seconds apart in both latitude and longitude, which is the finest resolution that is publicly available for the Canadian northern area, and the map scale is 1: 250,000.

RiverTools is one of the most popular software applications that can manipulate topographic data in the form of DEMs; it not only makes attractive maps and images, but also derives a trove of useful quantitative information, for example, the lengths and slopes of channel segments, the number of streams of a given order and the contributing area of a watershed. The robust extraction method used in RiverTools is the D8 algorithm, which assumes that the flow direction is into only one of the eight surrounding cells for

the steepest slope between cell centers. Due to its simplicity and effectiveness, the D8 algorithm is widely applied to DEM analysis. Figure 3.4 shows how the D8 algorithm works. The first diagram gives a general view of the D8 algorithm. In the second, the value of the blocks indicates the relative elevation from the center cell. Flow path is from the center to the lowest adjacent cell.

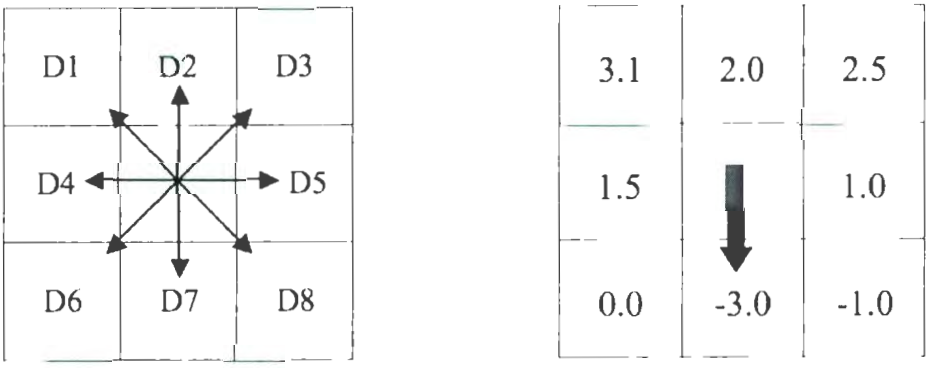

Figure 3.4 Schematic diagram showing the principle of D8 algorithm.

The four essential steps are listed below for a delineation procedure using RiverTools.

1. Importing a DEM. DEMs in many standard formats can be imported and converted into a RiverTools grid (RTG) file, which is a binary file with the compound extension "_DEM.rtg".
2. Extracting drainage networks. First, create a RiverTools D8 flow grid file which is needed to delineate watersheds and extract information for a river network. Second, choose a precise location as the basin outlet to specify the watershed of interest. Third, generate a vector-formatted treefile that stores basic attributes and

network topology for each pixel from the D8 flow grid. Fourth, use a pruning method and threshold to automatically compute and archive channel sources.

3. Exporting vector. The spatial coordinates and attributes of channel links and boundaries can be exported to an ESRI shapefile.
4. Displaying images. RiverTools can display the original DEMs, a density plot, a contour plot, a surface plot, a shaded relief, a shaded aspect, river networks and a multi-layer plot. When the multi-layer plot is used, the geodetic datum of each image should be identified to avoid shifting.

Strictly defining watershed boundaries and drainage networks is difficult because of limited DEM resolution for the areas where topography is subtle. When a continuous land surface is discretized to create a DEM, features smaller than a pixel can no longer be resolved. Therefore it is important to realize that it is mathematically impossible to uniquely recover the original surface from a discretized version. Pits and flats result from horizontal and vertical discretization, respectively.

Another cause of inaccurate comparisons is the Geodetic datums and coordinate systems. Geodetic datums define the size and shape of the earth and the origin and orientation of the coordinate systems used to map the earth. They range from flat-earth models used for plane surveying to complex models used for international applications. Coordinate systems specify locations on the surface of the earth using lines of latitude and longitude. The most commonly used coordinate system today is the latitude, longitude, and height system. Referencing geodetic coordinates to the wrong datum may result in position errors of hundreds of meters. Hence, comparison of difference maps

should be based on only one coordinate system and geodetic datum. The Global Positioning system is based on WGS 84. Datum conversions from other datums are completed by ArcGIS.

3.2.2 Results

A DEM of the lower Churchill ranging latitude 57° 10' N to 58° 10' N and longitude 94° 4' W to 95° 23' W was selected for the Deer River watershed delineation. Figure 3.5 shows the delineated watershed boundary and river networks bounded in the basin using RiverTools Version 3.0. The DEM at a scale of 1:250,000 is displayed with a density plot

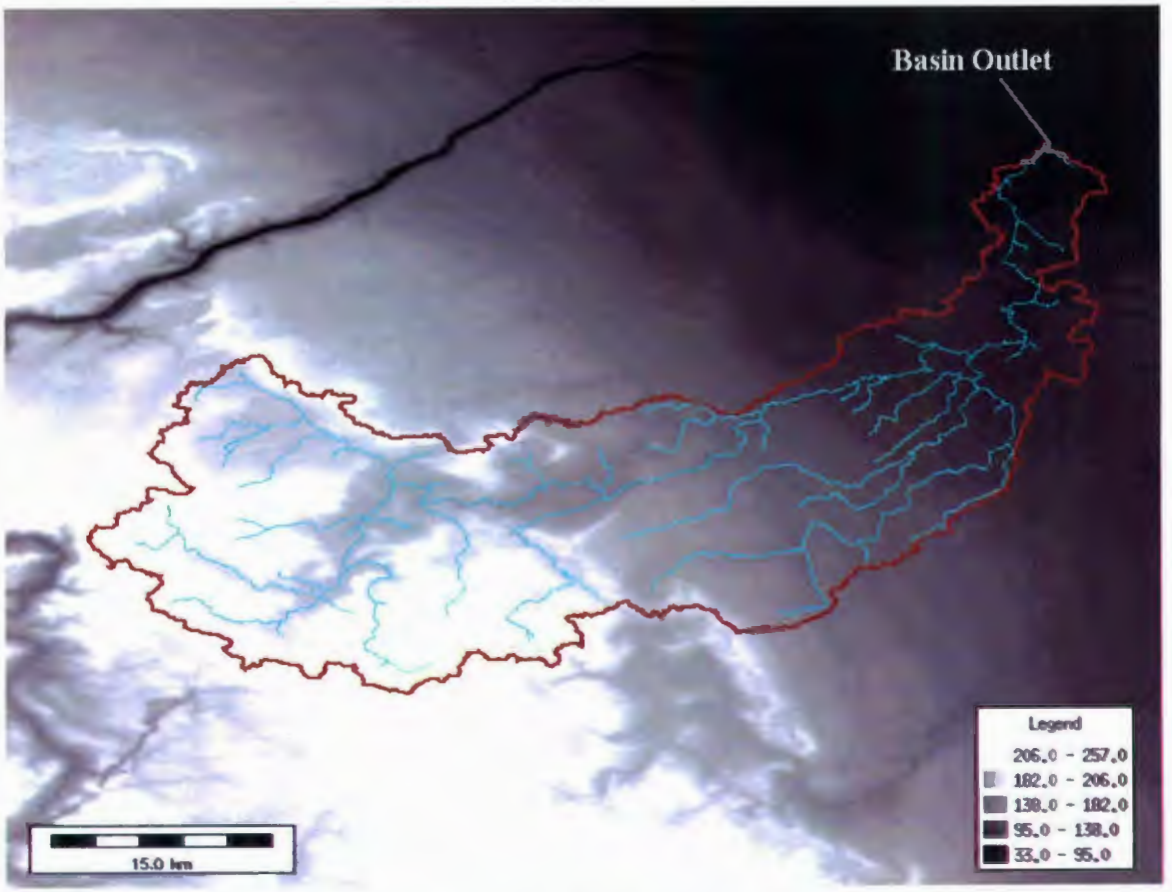

Figure 3.5 Map of the Deer River watershed boundary and the river networks with pruning threshold 6, with the background of the DEM density plot.

as background, where darker shades designate lower elevations (see the legend for spectrum details). The basin outlet chosen at Deer River North of Belcher (58° 0' 54" N, 94° 11' 44" W) is marked in the figure. From this figure, it can be seen that the river networks depict only two or three heads of channels due to the pruning threshold set to 6, which means the end 6 river trees have been pruned. The larger the pruning threshold selected, the more limited the river network is generated by the program.

In addition to the delineation plots, RiverTools derives basin information as well. Figure 3.6 describes the basic information from the DEM used for basin delineation. The number of columns and rows indicates the total cells of the DEM: 1206×1581; X-size and Y-size indicate the map resolution is 3 arc seconds (90 m) in both latitude and longitude; the upright block shows the four direction edge values of the DEM in the unit of degree; and the downright block shows the minimum and maximum elevation: 33 m and 257 m, respectively.

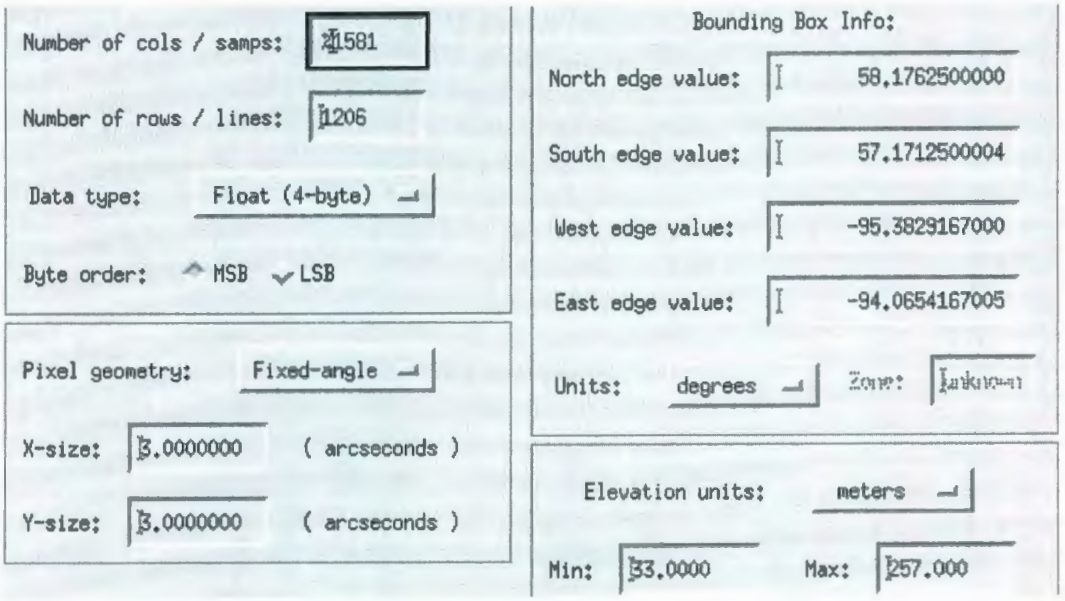

Figure 3.6 DEM map information obtained from RiverTools.

When the DEM analysis is finished, RiverTools will calculate the basin attributes shown in Figure 3.7. The basin outlet is located at the x-y coordinates of (-94.194, 58.015) with the elevation of 67 m. The Deer River watershed has a computed area of 1950.34 km^2. The watershed relief as measured from the highest point to the basin outlet is 174 m. The number of stream networks is 1213 and the longest channel length is 154.95 km. Drainage density, defined as the total channel length divided by the basin area, is 1.272 km^{-1}. It is noted that the pruning threshold shown in the figure is 4, because this threshold was recommended when RiverTools extracted the river network. To display river networks, a larger pruning threshold (i.e. 5 or 6) was used to distinguish channels for different needs, for instance, Figure 3.5 with a pruning threshold of 6, Figures 3.8 and 3.9 with a pruning threshold of 5.

Attributes of the 90501090 Basin

Outlet x-coordinate:	-94.193750
Outlet y-coordinate:	58.015417
Outlet pixel ID:	304978
Outlet parent pix. ID:	303398
Outlet elevation:	67.0000 (m)
Basin area:	1950.3394 (km^2)
Basin relief:	0.17400000 (km)
Pruning method:	Order
Pruning threshold:	4.00000
Strahler order:	6
Network magnitude:	1213
Network diameter:	177
Longest channel length:	154.94775 (km)
Total channel length:	2481.5242 (km)
Drainage density:	1.2723551 (km^-1)
Source density:	0.62194306 (km^-2)

Figure 3.7 Attributes of the basin derived from RiverTools.

Validation of the watershed boundary derived from RiverTools is difficult because there is no definitive map of the Deer River watershed boundary. One approach to assessing the accuracy of the boundary is to compare the basin area estimate with the contributing area reported in the WSC website. From the resulting attributes listed above, it can be seen that the derived basin area of 1950.34 km^2 is very close to the WSC published area of 1890 km^2, differed by only 3.19%. However, it is not possible to establish that this boundary is geographically correct as different shapes might result in similar areas, even the same area.

Another indication that the map is relatively accurate is that the river network from the National Topographic Data Base (NTDB) does not cross the derived boundary. The original NTDB map is based on the North American Datum of 1983 (NAD 83), while the DEM is based on WGS 84, so a datum conversion from NAD 83 to WGS 84 is employed using ArcGIS to make the comparison exact. If the map is not based on the right geodetic datum, a shift will be caused for the comparison. The distance for the shift depends on the two different kinds of datum performed. Figure 3.8 displays the comparative map of the watershed basin and a global map based on the North American Datum of 1927 (NAD 27). Figure 3.9 shows the derived watershed is overlaying with the same scale and datum NTDB map, which includes lakes, rivers and a railway. It is seen that most of rivers are matched together, although a few streams shift a little bit and few streams rarely cross the boundary. However, the streams do cross the lakes in the map, because the D8 algorithm cannot determine lakes using DEM. Figure 3.10 zooms into the tail part of the watershed for a close view.

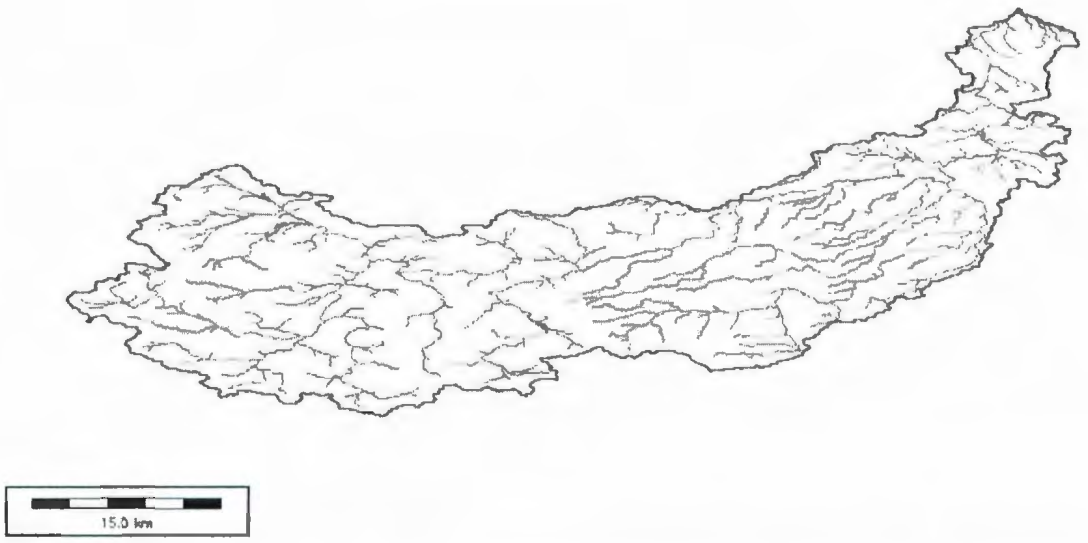

Figure 3.8 Map of the Deer River watershed boundary and the river networks with pruning threshold 5, compared to the digital map based on NAD 27.

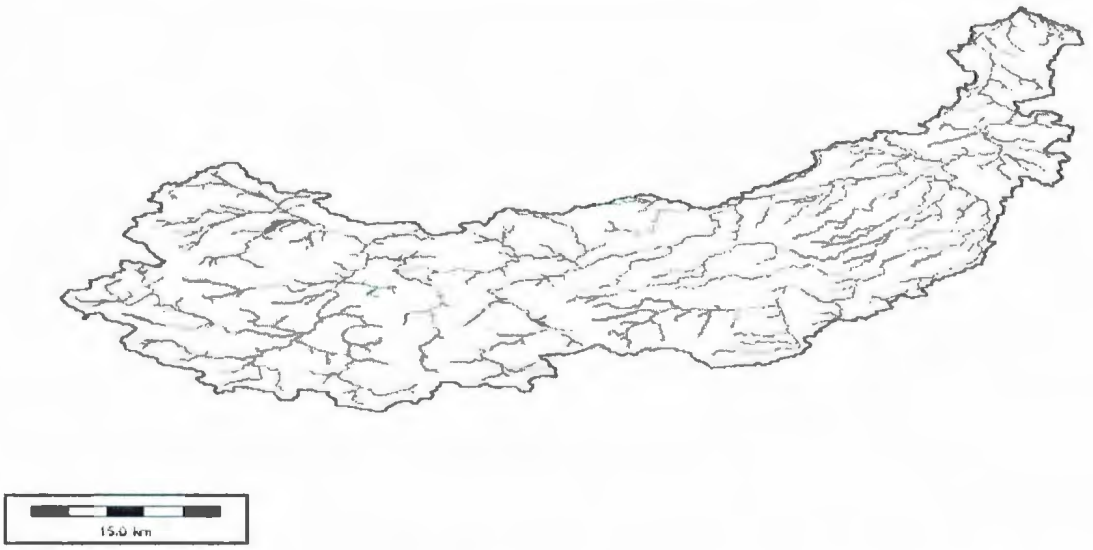

Figure 3.9 Map of the Deer River watershed boundary and the river networks with pruning threshold 5, compared to the digital map based on WGS 84.

The comparison between the derived watershed using a DEM and RiverTools and the published information and data provides verification of the DEM analysis algorithms. Existing differences are due to the choice of algorithms and DEM construction. The use of a USGS DEM and RiverTools to delineate the Deer River watershed was successful, and the resulting boundary and river networks are comparable to the river streams from the NTDB map. To improve the results, ANUDEM, a software program, has been designed to produce regular grid DEMs with sensible shape and drainage structure from arbitrarily large topographic data sets (Hutchinson, 2006). This program will solve the problem with lake boundaries via a drainage enforcement algorithm, and its application will be considered in future work.

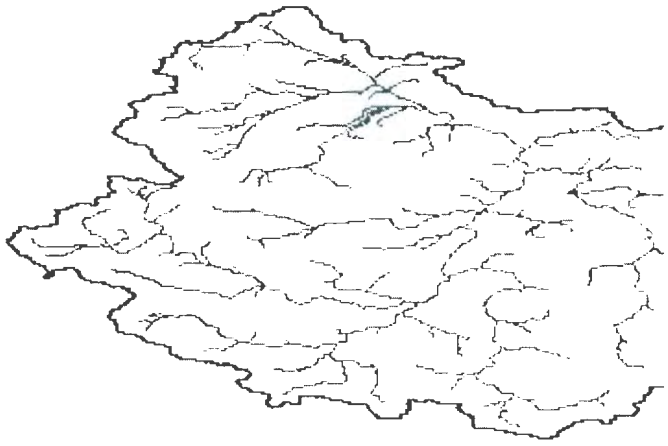

Figure 3.10 Tail part of the Deer River watershed.

4. Canadian Land Surface Scheme (CLASS) Testing

CLASS was originally designed for the four vegetation categories: coniferous trees, deciduous trees, crops and grass. The moisture transfer from these vegetation types is via the vascular pathway of root, stem and leaf. Therefore, to test the performance of CLASS, the datasets collected from the Fen site are used. The Fen site is primarily comprised of a mixture of sedges (*Carex* spp.), which are set to the grass category. Although the goal of this thesis is to model a lichen and moss site at Rail Spur, the Fen site is considered as providing a useful representative test of CLASS to determine how well it simulates vascular plants in a Canadian northern wetland compared to hourly or half-hourly field observations. Two simulations during the growing season (i.e. June to September) of 2006 and 2007 are employed and each contains different degrees of realism in model initialization. After a complete CLASS run, comparisons with measurements and examining the closure of the energy balance are required to estimate the accuracy of the model for further modelling.

4.1 Site Description

The field sites at which data were collected for CLASS modelling are Fen and Rail Spur in Churchill, Manitoba (Figure 3.2). Both are located within the Hudson Bay Lowland and are underlain by continuous permafrost. Patches of open woodland near the experimental area mark the edge of the northern boreal tree line and the transition to open tundra (Griffis et al., 2000). The Fen site (58° 39' 54.8" N, 93° 49' 51.6" W) is characterized by nonpatterned hummock-hollow terrain, predominately covered by the sedge species (*Carex aquatilis* and *C. Limosa*), with a moss base, separated by small open water pools. The water table at this site is at or near the surface throughout the whole year. The top of the permafrost layer is over 1 m from the surface during the late summer, and is closer to the surface in winter. The peat soil averages 25 cm thickness and is underlain by material of marine origin, consisting of fine silts and clays interspersed with layers of carbonate shingles.

According to a micrometeorological survey, small hummocks constitute 47%, hollows 48% and large hummocks 5% of the landscape with respect to the water table position (Griffis et al., 2000). The height of hummocks range between 0.07 m and 0.44 m, and the maximum vertical height difference between hummocks and hollows is approximately 0.75 m. The configuration and height of the hummocks and hollows determines the depression storage of surface water. A maximum amount of water storage occurs at a mean height 0.08 m above the base of the hollows (depression storage surface) (Rouse, 1998). As the water table rises above this equilibrium level, lateral drainage of water begins (Griffis et al., 2000).

The average water table height relative to the hummocks and hollows has an important influence on the distribution of vegetation (Billings 1987b; Bubier et al., 1995). On small hummocks, the vascular species (*Carex aquatilis, C. Limosa, C. Saxatilis* and *C. Gynocrates*) are the dominant vegetation, with a limited moss cover (*Tomenthypnum nitens*). Larger hummocks support vascular species (*Betula glandulosa, Ledum decumbens, Salix arctophila* or *Carex* spp.) and non-vascular species of lichen (*Cladina stellaris* and *C. rangiferina*) and moss (*Dicranum undulatum*). Brown moss (*Scorpidium turgescens*) as a base is usually found in the wet hollows.

A tower-based eddy covariance system was installed at Fen to obtain surface scalar fluxes for the growing season. Fluctuations in wind speed in the three directions (x, y, z) and virtual sonic temperature were measured using a three-dimensional sonic anemometer CSAT3. Water vapour fluctuations were measured using an open-path infrared gas analyzer (IRGA) LI-7500 (Figure 4.1). The open-path eddy covariance setup allows ambient air to pass freely between the IR source and detector of the IRGA. To be able to measure the gas concentration fluctuations it is

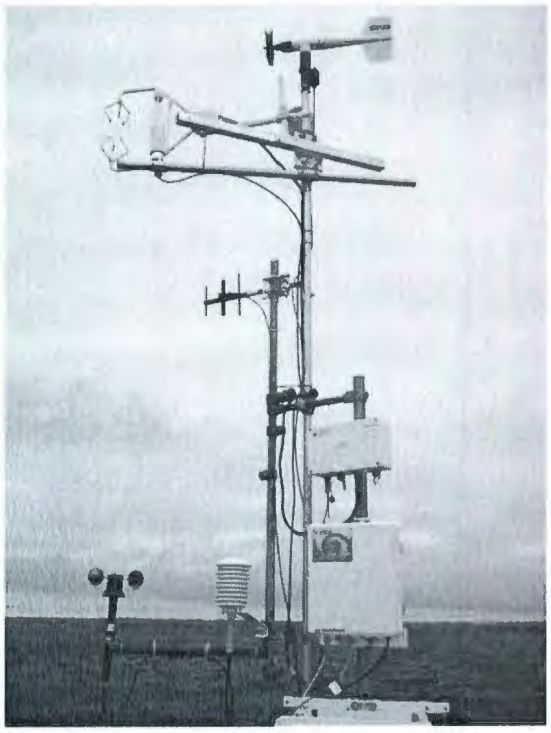

Figure 4.1 Open-path eddy covariance system with a Gill Windmaster sonic anemometer and a Licor LI-7500 open-path IRGA, installed at Fen. Photo taken by Kyle Swystun, in 2007.

essential that the open-path IRGA be located close to the sonic (Anthoni et al., 2002). The measurements for the CSAT3 and LI-7500 were taken at a height of 3.9 m above the surface. Barometric pressure was obtained using an RM Young Barometric Pressure Sensor 61205V, located in the data logger enclosure at a height of 1.5 m above the surface. Measurements were taken at a frequency of 20 Hz for these instrumentations (CSAT3, LI-7500 and 61205V) and logged using a Campbell Scientific Data Logger CR5000.

Lower frequency measurements were taken every 3 seconds and averaged over the half hour using the CR5000 and included: air temperature and relative humidity (HMP45CF and HMP45212) at 3.4 m and 1.8 m above the surface, respectively; wind speed at 4.1 m (RM Young 05103) and 1.8 m (Met One 013); wind direction (RM Young 05103) at 4.1 m; photosynthetically active radiation (PAR LITE); shortwave radiation from 0.285 μm to 2.8 μm (Eppley PSP), longwave radiation from 3.5 μm to 50 μm (Eppley PIR), and net radiation from 0.25 μm to 60 μm (Q-7.1-L: REBS net radiometer). Given these wavelengths measured by the different instruments, the shortwave (0.285-2.8 μm) and longwave (3.5-50 μm) ranges do not cover the same wavelength bands as the net radiation (0.25-60 μm) inclusive.

Soil measurements were taken every 3 seconds and averaged over the half hour using a Campbell Scientific Data Logger CR23X and included: two thermocouple rods, one soil moisture probe (ML2x), and three soil heat flux plates (Middleton CN3), and three 5cm depth thermocouple measurements.

Two datasets are available for use in CLASS, from the growing seasons of 2006 and 2007. Measurements for 2006 are from June 1 to October 31, including: vapor pressure, concentration of CO_2, sensible heat flux, latent heat flux, Bowen ratio, flux of CO_2, friction velocity, horizontal wind speed, air temperature, saturation vapor pressure, relative humidity, net radiation, photosynthetically active radiation, longwave radiation, incident solar radiation, reflected solar radiation, albedo, wind direction, ground heat flux and weather. They are all in hourly time step. Measurements for 2007 are from May 24 to October 12, including: air temperature, relative humidity, wind speed, wind direction, standard deviation of wind direction, downwelling shortwave radiation, upwelling shortwave radiation, downwelling longwave radiation, net radiation, ground heat, pressure, vapor prssure, specific humidity, sensible heat flux and latent heat flux. Part of them are hourly and others are half-hourly.

4.2 CLASS Simulation

For this simulation, CLASS ran in stand-alone mode (not coupled to a GCM), using identical surface forcing and ground initial conditions. It requires three input files for complete operation: an initialization file, a meteorological forcing file and a soil layer file. The initialization file contains the specific parameters of the site being investigated at the beginning of the data period; the meteorological file contains all the data required to run CLASS; and the soil file contains the thickness of each of the three soil layers. Details of these files will be discussed in the subsequent sections.

4.2.1 Model Initialization

The preparation of the initialization file for CLASS is a critical and sensitive step. It includes background information on the soil and vegetation types at the site, initial values for soil temperatures and moistures, and other initial conditions for each type of vegetation present (fractional coverage, maximum and minimum leaf area index (LAI), roughness length, visible and near infrared albedos, above ground standing biomass, and rooting depth). Taking the Fen site during the 2006 growing season as an example, the entire content of the initialization file is presented in Table 4.1.

Table 4.1 Parameters used in the CLASS initialization file for Fen during June 8-14, 2006.

```
 1 Fen 2006
 2 Churchill Manitoba
 3 June 8-14
 4    58.67    266.17      4.03      3.38     50.00   -1.0    1    1    1
 5  0.000   0.000   0.000   1.000   0.000   0.000   0.000   0.000   1.000
 6  0.000   0.000   0.000  -3.507   0.000   0.000   0.000   0.000   1.000
 7  0.000   0.000   0.000   0.040   0.000   0.000   0.000   0.000   0.130
 8  0.000   0.000   0.000   0.080   0.000   0.000   0.000   0.000   0.100
 9  0.000   0.000   0.000 150.000           0.000   0.000   0.000  30.000
10  0.000   0.000   0.000   0.500           0.000   0.000   0.000   0.400
11  0.000   0.000   0.000 100.000           0.000   0.000   0.000   5.000
12  1.000   4.100   1.000
13 3.5E-2  0.3E+0  2.0E+3  0.1E-4       1
14     -2.0      -2.0       5.0
15      0.0       0.0      55.0
16      1.0       2.0       0.0
17     0.94     -0.12     -2.97      2.70      0.00      0.00
18    0.930     0.150     0.225     0.000     0.730     0.275     0.100
19   0.0000    0.0000      0.00     0.000    0.0000     1.000
```

The first three lines display the test site information, such as the site name, location and the time period to run. Line 4 shows the basic site information: the latitude (58.67) and longitude (266.17) of the site, of which the longitude is measured in degree

east from 0° (i.e. 360° - 93.83° for Fen); measurement height for wind speed is 4.03 m and for temperature and humidity is 3.38 m; the blending height for aggregating surface roughness is set to a reasonable value of 50 m; ground cover code is set to -1 (-1 for land, 0 for ocean, 1 for sea ice); switch to specify whether the input refers to incoming or net longwave radiation at the surface (set to 1 as incoming longwave radiation is provided, else -1); the number of grid-cells being run and the number of mosaic tiles being used are all set to 1 for a single test site.

The following seven lines are related to vegetation parameters. There are four broad classification categories for vegetation: needleleaf trees, broadleaf trees, crops, and grass. Beside these four, CLASS has a fifth land cover type: urban areas, whose parameters are placed in the middle only four lines. The four columns before and after the middle one indicate parameters for the four vegetation categories respectively. At Fen, sedges and grasses comprise approximately 80% of total live vegetation, with the remaining 20% comprised of other vascular and non-vascular plants. It was decided that the fraction of the Fen site occupied by grass be set to 1, since the contribution by others is small. The leaf area index (LAI) is very low for the grassy site (i.e. LAI = 0.1-0.3), although it varies between summer and winter. As CLASS assumes a closed canopy and therefore does not allow LAI less than 1.0, maximum and minimum LAI (the last number of line 4 and 5 respectively) for the present short and sparse vegetation site are assigned a lower limit of 1.0 in order to avoid possible numerical instabilities in the prognostic equations for temperature (Bellisario et al., 2000). The roughness length is a measure of the aerodynamic roughness of the surface and defined as the height at which the neutral

wind profile extrapolates to a zero wind speed (Oke, 1987). It is about 0.1 of the average vegetation height according to the logarithmic wind profile. The height of sedges averages 0.3 m, so natural logarithm of the roughness length for Fen is -3.507.

CLASS divides the solar spectrum equally between visible and near infrared radiation. The all-wave albedo (α_A) is partitioned into values for the visible (α_{VIS}) and near infrared (α_{NIR}) albedo by making use of the observation that for most soils the near infrared is typically twice that of the visible albedo (Dickinson, 1983). The all-wave soil and vegetation albedo is obtained from the measured upward shortwave radiation ($K_\uparrow$) divided by downward radiation ($K_\downarrow$). Since the partitioning of solar radiation into visible and near infrared is approximated as 1:1 on average, visible and near infrared albedos can be calculated as:

$$\alpha_A = K_\uparrow / K_\downarrow \quad (4.1)$$

$$\alpha_{VIS} = 2\,\alpha_A / 3 \quad (4.2)$$

$$\alpha_{NIR} = 2\,\alpha_{VIS} \quad (4.3)$$

The all-wave albedo of Fen at the beginning of this time period was calculated as 0.06, so the visible and near infrared albedos are 0.04 and 0.08, respectively. The standing biomass density of the site is 0.13 kg m^{-2} and rooting depth is assigned 0.1 m for sedges.

Lines 9 to 11 are concerned with bulk stomatal resistance and its coefficients corresponding to the influence of natural environments. The minimum stomatal resistance (r_{min}) of a vegetation category is dependent on the vegetation properties under an unstressed condition. This minimum value for sedge tundra is set to 150 s m^{-1} from the National Centers for Environmental Prediction (NCEP). Environmental factors may lead

to stresses on the canopy to cause the stomata to close to prevent excessive transpiration, thus increasing the stomatal resistance. The effects of these stresses are expressed by functions of the incident solar radiation (light or $K_{\downarrow}$), the air temperature (T_a), the air vapour pressure deficit (Δe), and the soil moisture suction (φ_s). The general form of canopy stomatal resistance (r_c) are derived by incorporating these functions:

$$r_c = r_{min} \cdot f(K_{\downarrow}) \cdot f(T_a) \cdot f(\Delta e) \cdot f(\varphi_s) \qquad (4.4)$$

The coefficient governing the response of stomata to light is the value of visible radiation at which stomatal resistance is twice the minimum value. It was decided to use 30 for the Fen site because it has been found that a value of 30-50 works for a variety of vegetation ("Appendix D," n.d.). The coefficients governing the response of stomatal resistance to vapour pressure deficit (VPD) are set to 0.5 and 0.4, which are selected by adjusting the resulting latent heat flux with field measurements. Suggested values of 100 and 5 are utilized as the coefficients governing the response to soil water suction due to a lack of test datasets for this function.

Line 12 shows three values: a drainage index, set to 1.0 to allow the soil physics to model drainage, and to a value between 0 and 1.0 to simulate impeded drainage, the permeable depth of the soil, usually set to 4.1 m or less, and the fractional area that this tile represents when running a mosaic. In line 13, the first four values are WATFLOOD parameters, which are used if WATFLOOD algorithms are running. The switch IWF for employing these parameters is in the RUNCLASS file (1 on and 0 off). The last value of line 13 is a mosaic tile identifier, which has a value of 1 for land.

Lines 14 to 16 supply information on soil texture that could be used to calculate thermal and hydraulic properties for the site. The three columns indicate the three soil layers defined by CLASS. Lines 14 and 15 indicate the percentage sand and clay contents of each soil layer. At Fen, the top two layers are treated as organic (peat) with the soil type flag -2 (-2 for organic soil, -3 for impermeable rock, and -4 for an ice sheet), and the third layer are mineral (silt and clay) soil with percentage sand and clay contents assigned values of 5 and 55 respectively from observations. Hydraulic conductivity is the most variable of the peat parameters (Letts et al., 2000). Literature values of k_s were categorized into fibric, hemic or sapric peat classes (1 denotes fibric, 2 denotes hemic, and 3 denotes sapric) based on descriptions of peat quality (Table 2.2). Fibric peat is defined as having high porosity, usually greater than 0.9, sapric peat is the most deeply humified organic soil, and hemic peat is between them. The percentage of organic matter in the mineral soil layer is assumed to be zero. The hydraulic conductivity of the mineral soil will be automatically calculated by CLASS according to the percentage sand, clay and organic matter contents.

Line 17 presents the temperatures of each soil layer, canopy, the snowpack and ponded water on the surface, respectively, and line 18 presents fractional volume of liquid and frozen water in the three soil layers and depth of water ponded on the surface, respectively. Field measurements of soil temperatures at depths of 0, 0.05, 0.1, 0.25, 0.5 and 0.75 m, and volumetric soil moistures at depth of 0.1 and 0.25 m provide accurate estimates for the two upper soil layers. The value corresponding to the midpoint of the layer is chosen as the layer temperature. Since the measured soil temperature and

moisture do not extend very far into the third layer, the ability to accurately define the characteristics of this layer is limited. The temperature of the third layer (T_3) is initialized based on the trend in the soil temperature profile, typically using linear extrapolation from the last two deepest measured values to the middle depth of the layer. This method is deemed a reasonable approximation due to high variation of soil temperature with depth though no accuracy has been assessed till now. For example, there are measured soil temperatures (°C) at each depth respectively, on June 8, 2006, at 6:00 AM from the McClintock site, which is close to the Fen site:

T_0 = 1.227, T_5 = 0.941, T_{10} = 0.363, T_{25} = -0.122, T_{50} = -0.655, T_{75} -0.991

where the subscripts designate the measurement depth in mm, and the thicknesses (m) of each soil layer: Z_1 = 0.1, Z_2 = 0.25, Z_3 3.75

For the first soil layer: $T_1 = T_5$ = 0.94 °C

For the second soil layer: $T_2 = T_{25}$ = -0.12 °C

For the third soil layer, this equation is generated from linear extrapolation:

$$\frac{T_{75} - T_{50}}{0.75 - 0.5} = \frac{T_3 - T_{75}}{Z_3/2 - 0.75} \tag{4.5}$$

so that: T_3 = -2.97 °C

For Fen in 2006, soil temperature and moisture data were lacking, so data from McClintock are used instead. The canopy temperature is difficult to measure directly. Hence, CLASS is usually initialized at midnight with the initial canopy temperature set to air temperature. An air temperature of 2.7 °C was observed for the Fen site.

The Fen site has a water table position on the surface throughout the year and is underlain by permafrost. Frozen water on the surface began melting in June when the air

temperature increased. The soil moisture of the first layer at Fen was set at saturation, equal to the porosity of fibric peat 0.93. Since the second and third layers were still frozen, the liquid moisture was set to the residual water content and the remainder was frozen water content. The residual water contents for hemic peat and mineral soil are 0.15 and 0.225 respectively, obtained from the notes by Lee and Pielke (1992), so the volumetric frozen water contents in these two layers are 0.73 and 0.275 respectively corresponding to the porosity of hemic peat (0.88) and mineral soil (0.5). Depth of water ponded on the Fen surface was set to 0.1 m at that time.

The last number of line 19 is the vegetation growth index. This has a value of 1 in full leaf, and 0 during dormant and leafless periods; the transition between the two is estimated. Grass is assigned a growth index of 1 throughout the year, since its annual variations in height and leaf area index can be considered as negligible (Verseghy et al., 1993).

All of the parametrizations required in the CLASS initialization file for Fen were described in details above, including examination approaches and real values applied. For each run, only one initialization file is required, and there is no need to update the parameters in the file, as CLASS updates them internally while the model is running. To run other test periods at Fen, most of initialized parameters are common to all datasets as they belong to a single site. However, from site to site the attributes vary greatly due to different site characteristics.

4.2.2 Data Preparation

In addition to the initialization file described in the last section, a meteorological forcing file and a soil layer file are also needed. The meteorological forcing file contains eleven columns of datasets, each of which represents one variable. They are hour, minute, day (year day), year, incoming solar radiation (W m^{-2}), incoming or net longwave radiation (W m^{-2}), precipitation rate (mm s^{-1}), air temperature (°C), specific humidity (dimensionless), wind speed (m s^{-1}), and atmospheric pressure (Pa). The seven meteorological variables required as input to CLASS have a time step of 30 minutes and are contiguous. Hourly measurements will be duplicated once to make them half-hourly.

Two datasets during the 2006 and 2007 growing seasons at the Fen site are examined for CLASS performance, because they have all the measured energy and heat fluxes that can be used to generate diurnal energy closure in order to evaluate CLASS simulation results. However, field measurements from the site during each growing season are not absolutely continuous. Some data are missing for almost all variables, so the gaps have to be filled in using linear interpolation to make the data successive in separate short periods. As to long-term missing data, the 2006 growing season has been divided into three periods: June 8-14 (158 data), June 21-25 (96 data), August 2-5 (75 data), and the 2007 growing season has been trimmed to a period of May 28-September 12 (5156 data). The 2006 measurements are at an hourly timescale, and part of the 2007 measurements are hourly and part of half-hourly. In addition, no data for atmospheric pressure was available in 2006, and the pressure measured from the Churchill airport was then substituted. Previous tests showed little sensitivity on the part of CLASS to this

variable. Neither in 2006 nor in 2007, Fen measured the time series of rainfall, so instead the precipitation rates from Rail Spur were used.

Another requirement for the input variables is that the specific humidity needs to be calculated from other parameters. Specific humidity, q, is the concentration of water vapour expressed as the mass of water vapour per unit mass of air (Dingman, 2002):

$$q = \frac{\rho_v}{\rho_a} = \frac{0.622 e_a}{p} \tag{4.6}$$

where ρ_v is the vapour density, ρ_a is the mass density of the air, e_a is the actual vapour pressure, and p is the atmospheric pressure. ρ_v and ρ_a are in the same units, kg m^{-3}, and e_a and p are in the same units, kPa or Pa. A mismatch in the generation of saturated humidity for CLASS can lead to prolonged downward gradient of moisture for extended periods during the winter and results in very large accumulations of snow on the land surface owing to a near continuous condensation process (Snelgrove, 2002). Thus, when the temperature goes below zero, q can be calculated as:

$$q = \frac{0.622 e_a}{p - e_a(1 - 0.622)} = \frac{0.622 e_a}{p - 0.378 e_a} \tag{4.7}$$

CLASS currently divides the soil column into three layers with thicknesses of 0.1 m, 0.25 m and 3.75 m. The depths of the bottom of the soil layers down from the surface are 0.1 m, 0.35 m and 4.1 m, respectively. This division can adequately reproduce the soil thermal regime: a shallow surface layer to store diurnal temperature changes, an intermediate layer to resolve the temperatures in the middle vegetation rooting zone, and a deeper layer for annual variations (Verseghy, 1991). These values are contained in the soil layer file to be applied in the codes associated with the soil surface fluxes and

variations of temperature and soil water content. The depth of soil layers in this file can be manipulated. However, the default values for the three soil layers are maintained for all CLASS runs in this thesis.

4.3 Bowen-Ratio Approach

The energy balance closure is a useful method to examine all the energy components as a whole. Generally, one hundred percent closure is unrealistic for field measurements. This is a result of not being able to resolve the entire spectrum of eddies owing to instrument limitations. With respect to the process of improving the eddy covariance program, which calculates the fluxes to include many of the spectral corrections, it was found that the processed data have higher values for Q_E and Q_H (Swystun, July 11, 2008). In Figure 4.2, the energy balance test on the measured data at Fen during the 2007 growing season is shown. It can be seen that K^*+L^* is greater than the measured Q^*, and both are greater than $Q_H+Q_E+Q_G$. Theoretically these terms should be all equal. Energy balance closure is apparently not closed, which might be due to problems with gap filling and inherent measurement problems of the turbulent fluxes in low wind speeds.

Since the measured turbulent fluxes contained obvious errors, it was decided to try and close the energy balance using the Bowen-ratio approach, which computes Q_H and Q_E based on K^*+L^* or Q^*, and Q_G. Given the fact that K^*+L^* does not equal Q^*, the result of different instruments measuring slightly different bands at varying locations, taking the average of the two offer a compromise (Swystun, July 16, 2008). In reality, it is common to have 10-20 W m^{-2} differences in the daytime hourly fluxes.

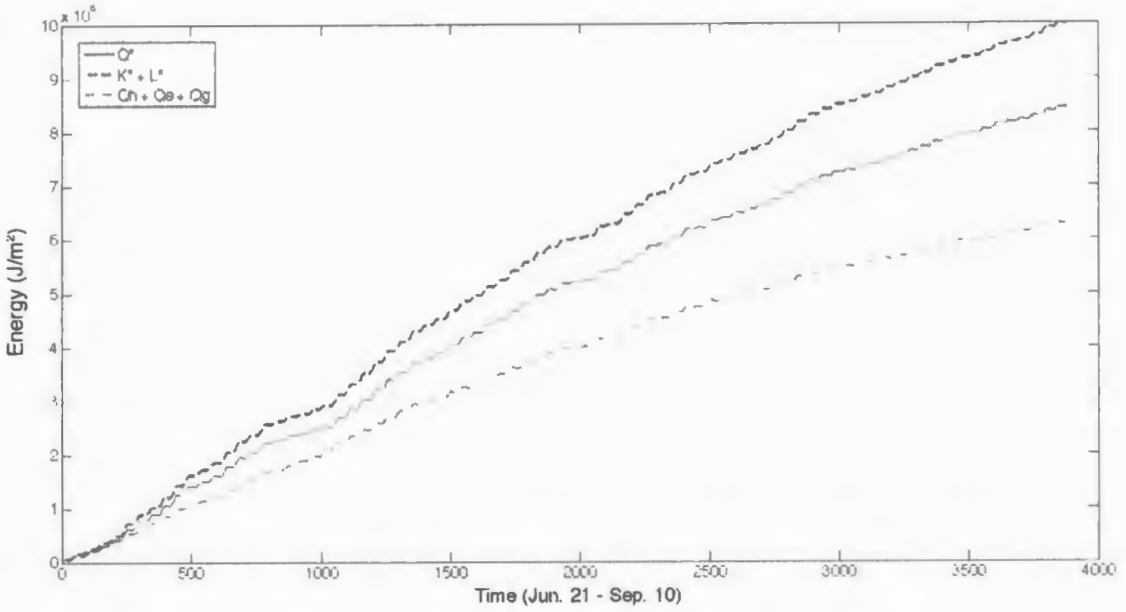

Figure 4.2 Cumulative net radiation from measured data for Fen 2007.

The ratio of Q_H to Q_E, originally formulated by Bowen (1926), is called the Bowen ratio:

$$B \equiv \frac{Q_H}{Q_E} = \gamma \cdot \frac{T_1 - T_2}{e_1 - e_2} \tag{4.8}$$

where γ is the psychrometric constant (see Subsection 6.3.1 for details), 0.066 kPa K^{-1} commonly used, T is air temperature, e is vapour pressure, and the subscripts refer to measurements at two levels in the air above the surface. The energy balance can be written as:

$$K^* + L^* - Q_H - Q_E - Q_G = 0 \tag{4.9}$$

Making use of the Bowen ratio and rearranging the equation yield:

$$Q_E = \frac{K^* + L^* - Q_G}{1 + B} \tag{4.10}$$

$$Q_H = B \cdot Q_E \tag{4.11}$$

Applying the measurements from Fen 2007, Q_E and Q_H were calculated, assuming the measured Q_G is accurate, and the energy balance must be closed. A comparison of the original measurements of Q_H and Q_E to the calculated is presented in Figure 4.3. The plot agrees with the analysis result from the data processing in the field, demonstrating underestimates of both fluxes, especially for Q_H, which is much lower than the expected. The percentage biases for Q_H and Q_E between the measured and calculated are 139.22% and 15.36%, respectively. Based on the resulting consistency of the data analysis and the calculations from the Bowen-ratio approach, and given the energy balance closure, it is decided to choose the calculated Q_H and Q_E as the true values to be used to evaluate CLASS simulation results.

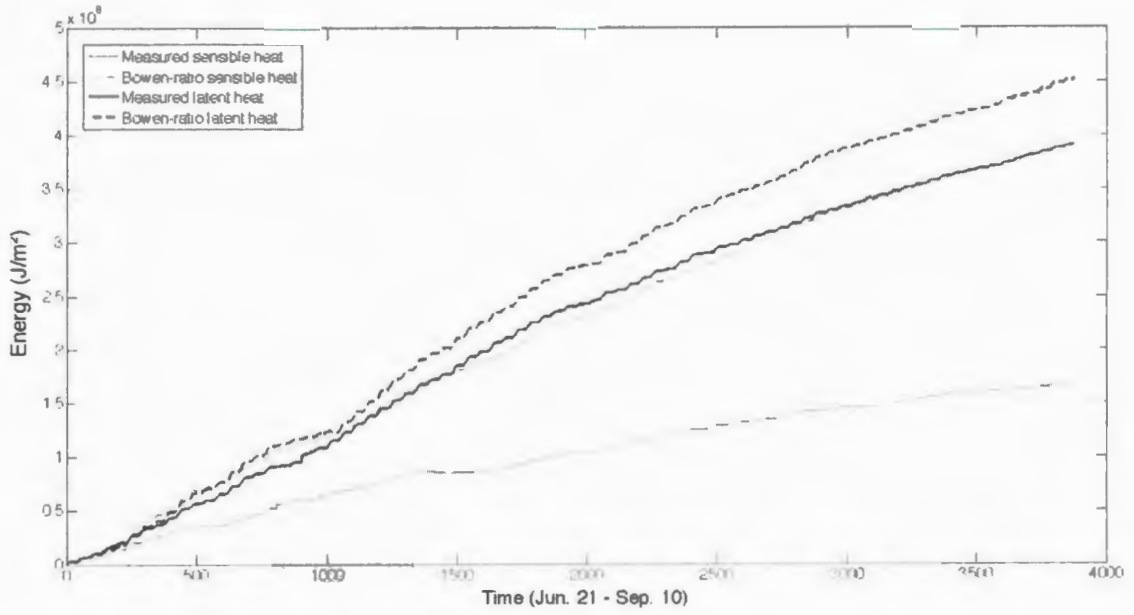

Figure 4.3 Cumulative heat flux from measured data versus the Bowen-ratio approach.

The net all-wave radiation is the most important energy exchange because for most systems it represents the limit to the available energy source or sink (Oke, 1987). To

ensure that the averaged Q^* used for the calculation is more accurate than the measured K^*+L^* or Q^*, a comparative plot of measured and CLASS modelled net radiation is displayed in Figure 4.4. It is shown that the averaged Q^* is closest to the modelled value from CLASS. However, the differences between the measured Q^* and K^*+L^* are expected, and researchers rely on the direct measurement when it is available. Hence, the measured Q^* is still used to compare the modelled value.

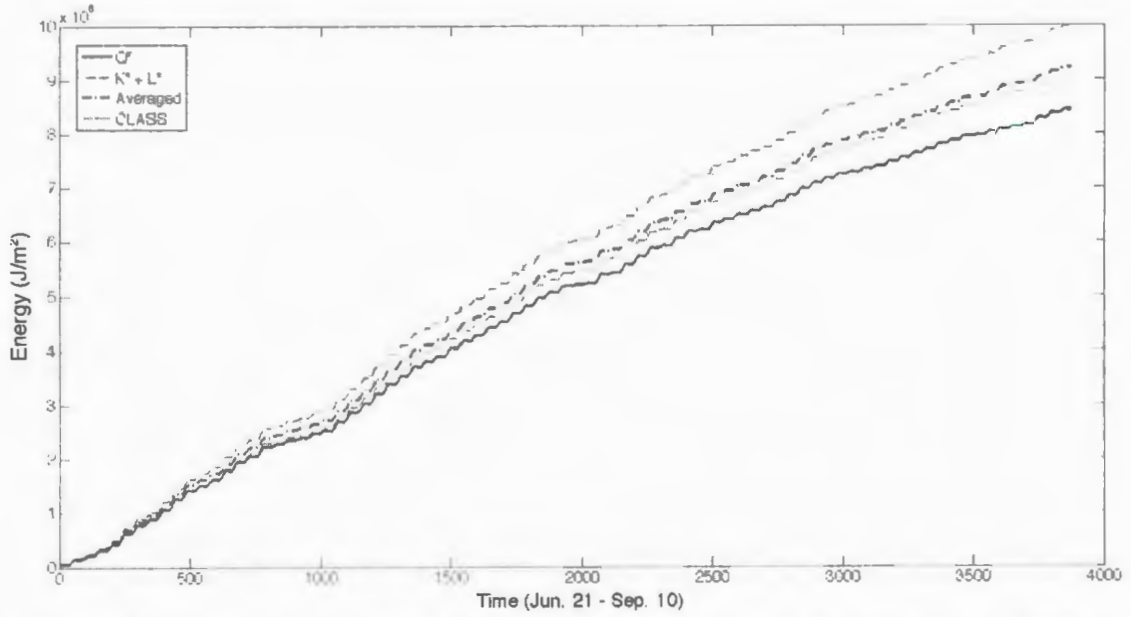

Figure 4.4 Cumulative net radiation from measured data versus CLASS for Fen 2007.

4.4 Analysis of Results

In this research, the analysis of results will concentrate on the components of the surface energy balance: net shortwave radiation (K^*), net longwave radiation (L^*), net radiation (Q^*), sensible heat (Q_H), latent heat (Q_E), and ground heat (Q_G). For each run, cumulative observed and simulated values of the above variables were comparably plotted. The biases of the modelled versus measured comparisons at the end of the data period were

calculated to evaluate the CLASS performance. Good modelling will have low values of all biases. Moreover, there are enough variable data at Fen to form the average diurnal cycles of the modelled and measured energy balance terms. The resulting average model outputs for energy and heat fluxes are compared with the observed averages.

Primarily, the CLASS runs are dependent on the correction of the resultant Q_E according to the measured values, as Q_E is the most important energy balance component, which links the energy and water balance equations. To examine this term, Figure 4.5 shows the diurnal plot of modelled versus measured Q_E fluxes for Fen 2006 during June 8-14. It can be seen that the half-hourly time series trends from CLASS and measurements are almost identical, although modelled results are sometimes overestimated or underestimated during this period. Taking the peaks of each day for example, for the days with low Q_E peaks, CLASS overestimated them, and for the days with high Q_E peaks, CLASS underestimated them. Due to this situation, the cumulative

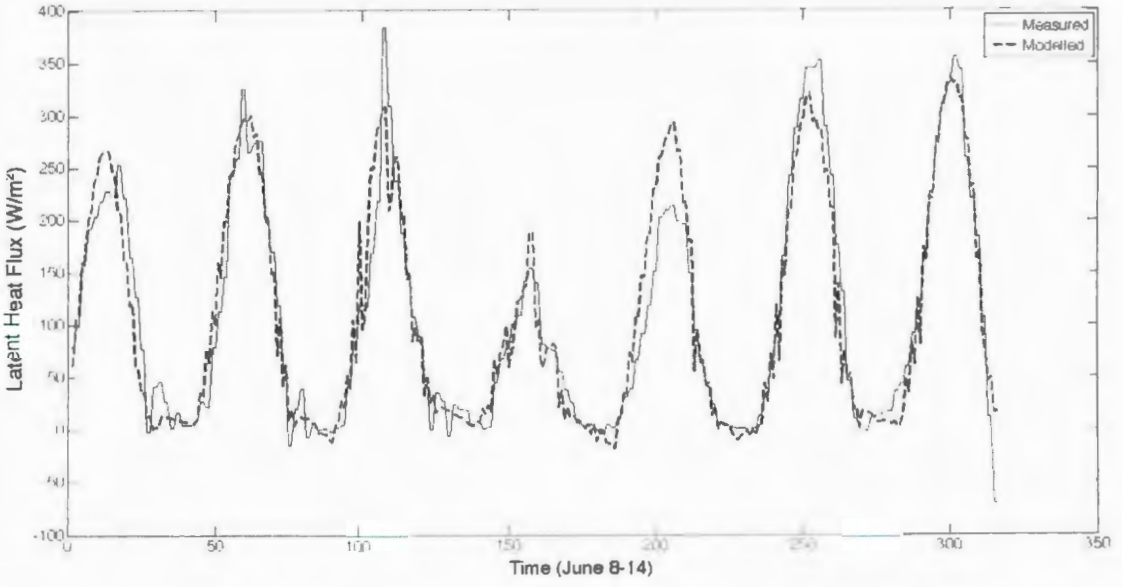

Figure 4.5 Modelled values of latent heat flux versus measured data for Fen 2006.

energy difference is not big when positive and negative errors cancel out. The cumulative Q_E plot of measured and modelled for the same period of Fen 2006 is presented in Figure 4.6. The cumulative Q_E from CLASS converges to the same value of cumulative field measurements at the end of each period, which illustrates a good overall estimation of Q_E by the model. This Q_E simulation represents evaporation modelling using CLASS for the sedge Fen tundra in Churchill.

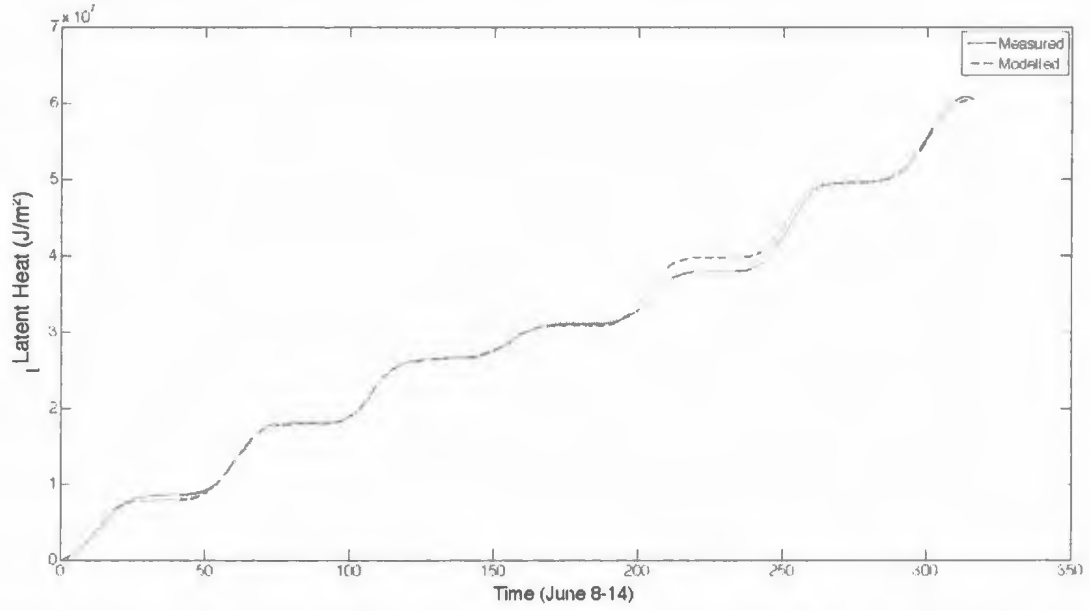

Figure 4.6 Cumulative latent heat from CLASS versus measured data for Fen 2006.

Only examining Q_E is not sufficient to evaluate CLASS. Given the relative long term full data period of Fen 2007 from June 21 to September 10 (3876 data), it is more representative to display the simulation of the 2007 growing season. Hereafter, all the energy balance components of measured or calculated and modelled for Fen 2007 are cumulatively plotted in Figure 4.7, and the corresponding biases appear in Table 4.2. Note that the Q_H and Q_E used for the comparison were actually calculated from the

a)

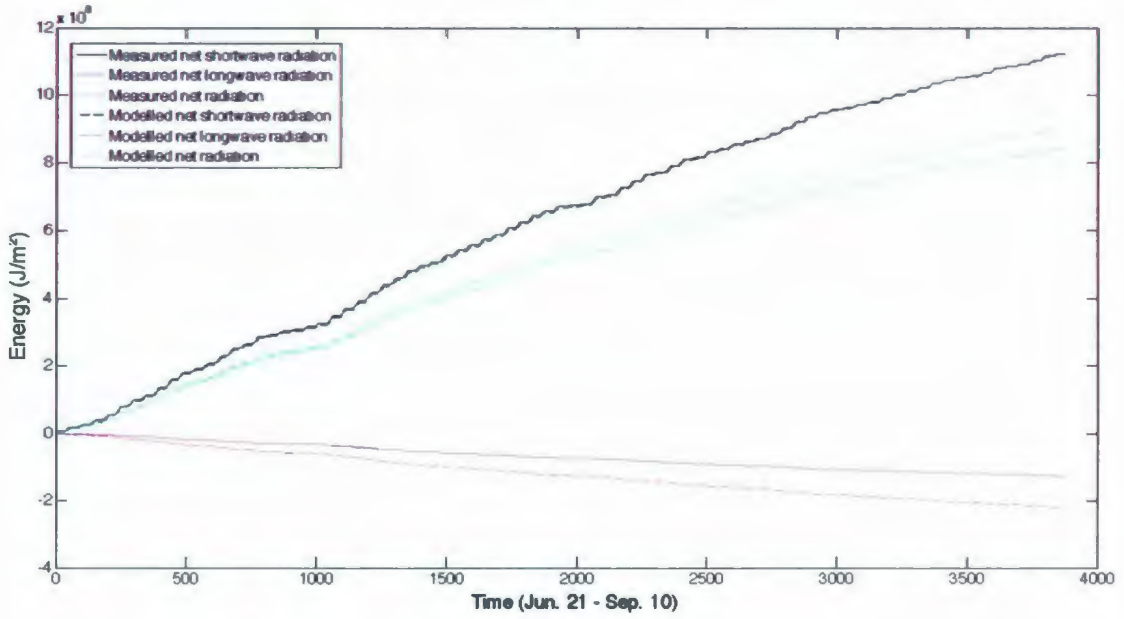

b)

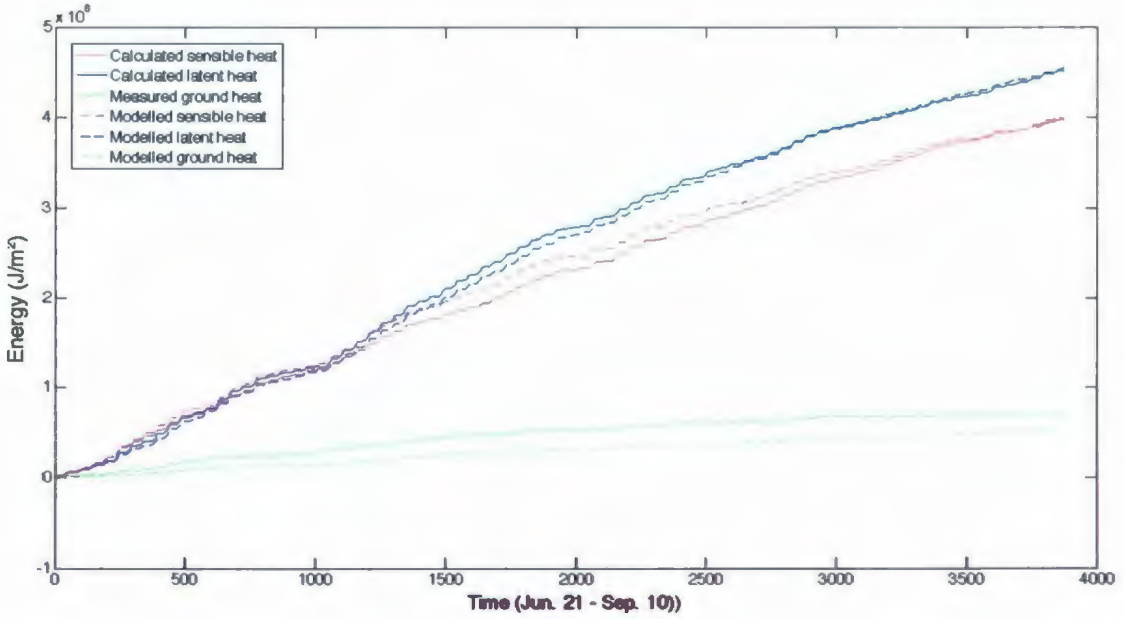

Figure 4.7 Cumulative energy budget of CLASS versus measured data for Fen 2007. a) Energy fluxes; b) Heat fluxes.

Table 4.2 Cumulative bias comparison of modelled versus measured energy balance results for Fen 2007. The units are J m^{-2}, except errors.

	Modelled	Measured	Bias	Error (%)
K^*	1.123×10^9	1.124×10^9	-9.49×10^5	-0.08
L^*	-2.198×10^8	-1.263×10^8	-9.35×10^7	74.05
Q^*	9.035×10^8	8.429×10^8	6.054×10^7	7.18
Q_H	3.983×10^8	3.978×10^8	4.57×10^5	0.11
Q_E	4.545×10^8	4.513×10^8	3.26×10^6	0.72
Q_G	5.069×10^7	7.138×10^7	-2.07×10^7	-28.99

Bowen-ratio approach that was discussed in the last section. From the Figures, it is observed that K^*, Q_H and Q_E are modelled very well by CLASS. Plots show good fits with low errors, generally within 1%. Q^* is overestimated somewhat, but L^* and Q_G are underestimated (negative denotes away from surface). L^* and Q_G are directly related to soil temperature. The high errors in L^* represent the low measured value, which means the surface temperature is lower than the modelled value. The lower modelled Q_G means too much energy is emitted from the surface. The soil temperature should be lower than the expected. For CLASS, the energy balance is absolutely closed (Figure 4.8), because the program codes were designed based on the energy and water balances. The cumulative plot shows that the two lines of $K^* + L^*$ and $Q_H + Q_E + Q_G$ are exactly overlapped with each other. This balance can also explain why the Bowen-ratio approach provides more reasonable results than the eddy covariance measurements.

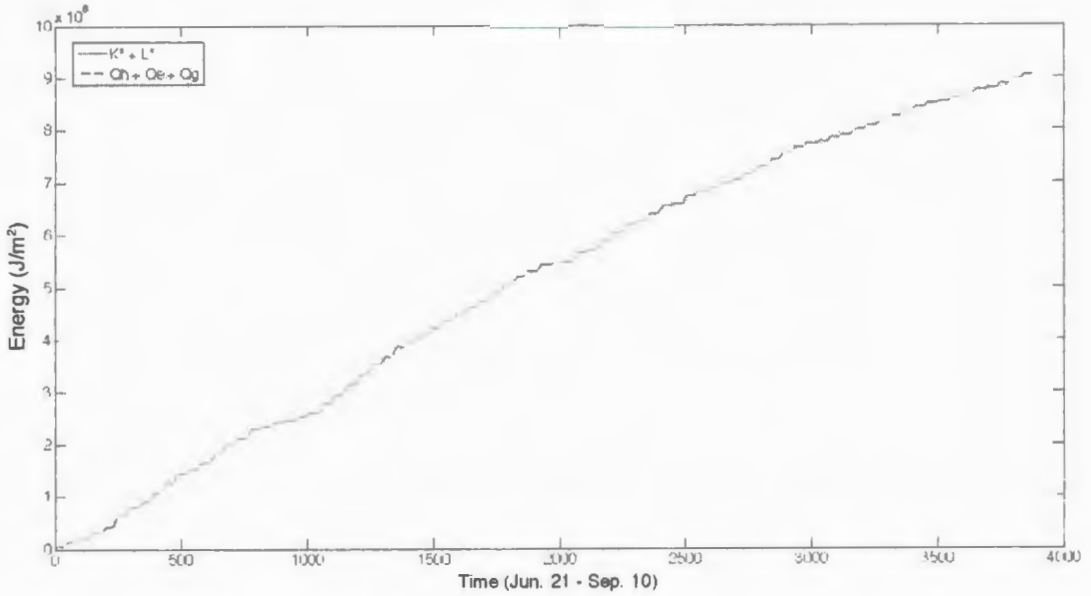

Figure 4.8 Energy balance test for CLASS for Fen 2007.

Another way to examine meteorological data is to form the diurnal energy balance. Diurnal cycles reflect energy fluctuations during a 24-hour time span. Diurnal plots of the mean half-hourly measured or calculated and modelled energy and heat components were generated for the Fen 2007 simulation, and are shown in Figure 4.9. The maximums of K^* and Q^* occur around local solar noon, with the minimum of L^*. K^* is controlled by the azimuth and zenith angles of the sun, and the surface albedo. It only has positive values during the daytime (from sunrise to sunset), but zero at night. Figure 4.9 a) visually shows a quite good fit of the measured and modelled K^*. The value of L^* is usually negative and relatively small if the surface and air temperatures are not significantly different (Oke, 1987). The modelled L^* is lower than the measured, which means the surface temperature in CLASS is higher than the actual temperature. This difference in L^* must cause the difference in Q^* because of the equation: $Q^* = K^* + L^*$.

a)

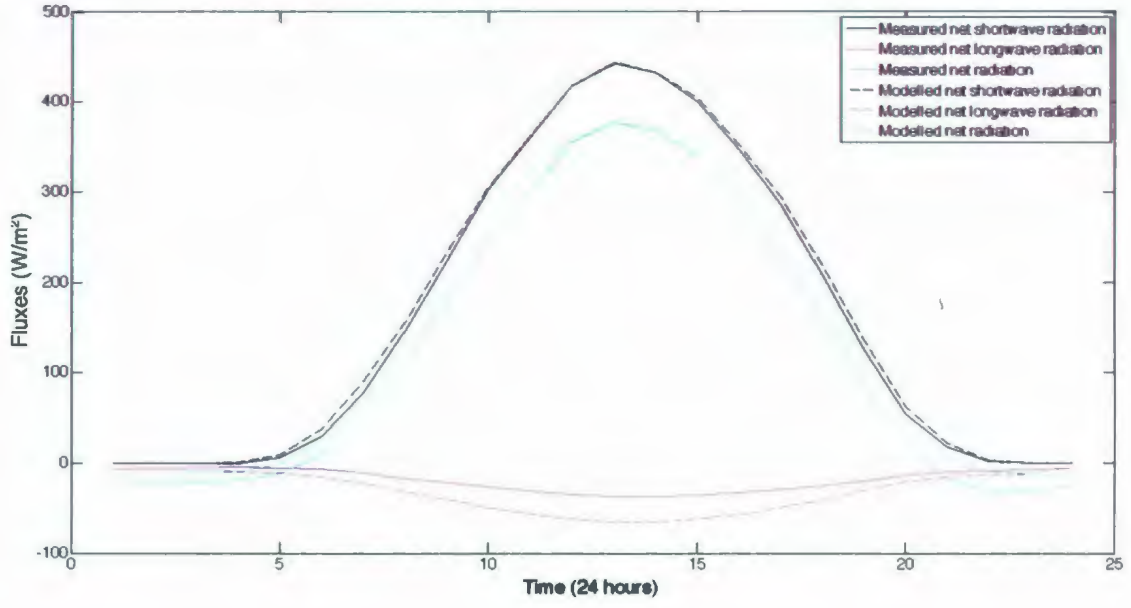

b)

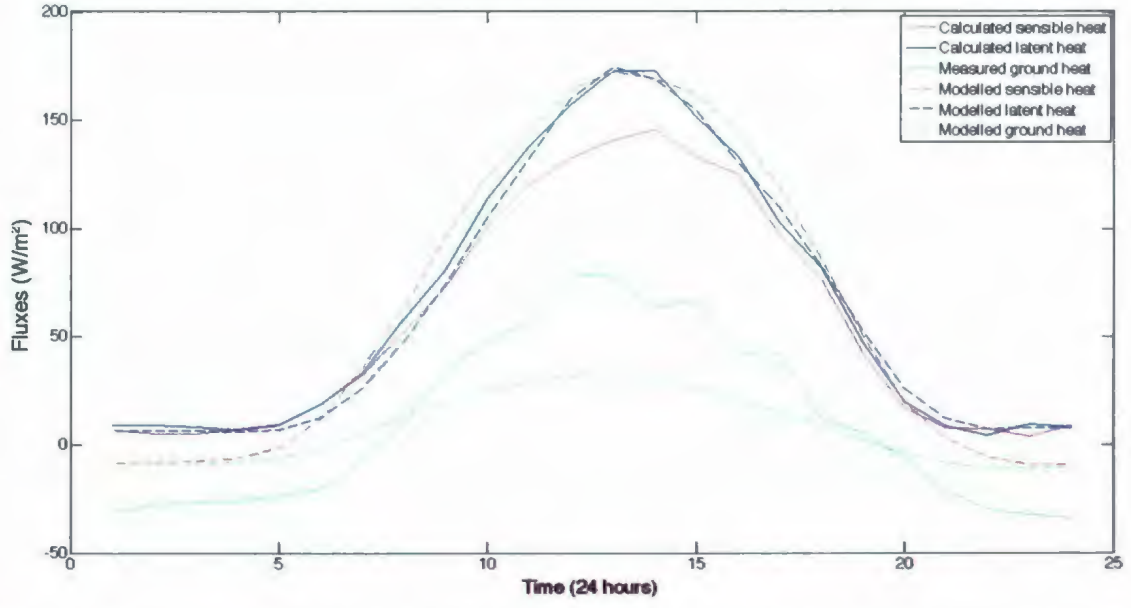

Figure 4.9 Average diurnal variation of measured and modelled surface energy fluxes for Fen 2007. a) Energy fluxes; b) Heat fluxes.

The typical diurnal course of Q^* involves a daytime surface radiant surplus and a nocturnal surface deficit. The modelled Q^* is matched to the measured around the middle of a day, but begins to overestimate the measured towards both sides. This is because the heat capacity of the surface is higher than that in CLASS, so that the ground can hold more energy by day to increase the temperature, and emit more longwave radiation at night.

Heat fluxes are the most difficult parts of the energy balance to be simulated. From Figure 4.9 b), it is seen that Q_E is modelled quite well, but Q_H and Q_G are not, even though the cumulative plots showed acceptable fits for them. The modelled Q_H is overestimated during the daytime and underestimated during the nighttime, while Q_G is overestimated during the nighttime and underestimated during the daytime. These opposite quantities for each term cancel out in the cumulative plots and result in an overall energy balance, although the measured data fluctuate more than the modelled. The differences caused by CLASS may result from the low surface heat capacity used in CLASS. The surface temperature should be higher by day and lower by night in order to agree with the Q_H and Q_G measurements.

5. Modelling Longwave Radiation

Longwave radiation, a component of the energy balance, is a form of energy with wavelengths in between 4 and 20 μm emitted by materials at near-earth-surface temperatures. It is determined by the emissivity and temperature of the material based on the Stefan-Boltzmann Law. Incoming longwave radiation flux is required as an input variable to run CLASS, but field measurements are not available at the Rail Spur site where evaporation is modelled from wetland lichen and moss tundra. Fortunately, longwave radiation is measured at Fen so that the relationship between incoming longwave radiation and the degree of cloud cover can be sought, which is related to weather conditions. Hence, longwave radiation at Rail Spur can be modelled corresponding to the weather conditions on site.

Two models used to simulate incoming longwave radiation are the traditional Stefan-Boltzmann equation which considers the effects of cloud and the modified combination of Efimova (1961) and Jacobs (1978) formulations. The Stefan-Boltzmann equation is a common means to estimate the rate of energy emission, while the modified

Efimova-Jacobs combination method is specific for the northern arctic environment. After applying both models to the Fen site, the degrees of cloud cover were associated with the weather conditions, and the results were compared to field observations in order to determine which model is better for modelling longwave radiation at the sites.

5.1 Clear-sky and All-sky

A number of numerical models have been developed to estimate the incoming longwave radiation at the surface. These models are used to calculate longwave radiation exchanges in the atmosphere due to the absorption and emission by water vapour, CO_2 and ozone (Oke, 1987). Initially they were undertaken assuming cloudless skies, but later the formulae were modified to incorporate the effects of cloud using the observed cloud distribution. Many empirical formulations have been generated for atmospheric emissivity that takes cloud coverage into account, because the effects of cloud are difficult to model.

The rate at which longwave radiation is emitted by the atmosphere, clouds and overlying canopy (i. e. incoming longwave radiation flux $L_{\downarrow}$) is given by the Stefan-Boltzmann Law:

$$L_{\downarrow} = \varepsilon_{at} \cdot \sigma \cdot (T_{at} + 273.2)^4 \qquad (5.1)$$

where ε_{at} is the integrated effective emissivity of the atmosphere and canopy, σ is the Stefan-Boltzmann constant, equal to 5.67×10^{-8} W m^{-2} K^{-4}, and T_{at} is the effective radiating temperature of the atmosphere and canopy in °C. To estimate the value of $L_{\downarrow}$, ε_{at} and T_{at} are required. At the sites, T_{at} was measured, so the major problem in employing the Stefan-Boltzmann equation is to find the expression for ε_{at}.

The value of ε_{at} is a dimensionless quantity dependent on various conditions of cloudiness and forest cover. Since the effect of forest canopy was ignored due to a lack of forest at the site, sky cloudiness is the only factor affecting the estimation of longwave radiation. Sky cloudiness can be roughly divided into clear-sky and all-sky conditions. Clear-sky is defined as occurring when the cloud cover of a sky is less than 10%, otherwise all-sky conditions exist. It is noted that the most important absorbers and emitters of longwave radiation in the atmosphere are CO_2 and water vapour (Dingman, 2002). As the concentration of CO_2 is quite constant over time, downward flux of longwave radiation under clear-sky and no forest is dependent largely on humidity. An empirical function expressing this relation was given by Brutsaert (1975):

$$\varepsilon_{at} = 1.72 \cdot \left(\frac{e_a}{T_a + 273.2}\right)^{1/7} \tag{5.2}$$

where e_a is atmospheric vapour pressure in kPa and T_a is air temperature in °C.

Clouds act almost as black bodies emitting longwave radiation at a rate determined by the temperature of the cloud base, and their presence greatly increases the effective emissivity of the atmosphere (Dingman, 2002). Thus under cloudy conditions emissivity ε_{at} is determined by the degree of cloud cover C. Kustas et al. (1994) gave an empirical equation expressing this relation:

$$\varepsilon_{at} = 1.72 \cdot \left(\frac{e_a}{T_a + 273.2}\right)^{1/7} \cdot (1 + 0.22C^2) \tag{5.3}$$

It can be seen that this equation is the combination of the equation for clear-sky emissivity with cloud effects, and provides the all-sky longwave radiation. Incoming longwave radiation will increase associated with clouds.

5.2 Modified Combination Model

The modified model is still based on the form of the Stefan-Boltzmann Law. The change is in the treatment of the atmospheric emittance and the cloud effects. It was proven that adjusting the cloudy-sky emissivity improved the estimated fluxes (Hanesiak et al. 2001). There are various empirical formulae developed for calculating incident longwave radiation under clear-skies or cloudy-skies, such as Ohmura (1981), Maykut and Church (1973), and Efimova (1961) forms for $L_{\downarrow clr}$, and Jacobs (1978) and Maykut and Church (1973) forms for $L_{\downarrow all}$. Hanesiak et al. (2001) tested the performance of these five longwave simulation models using unique observations from the 1998 International North Water (NOW) Polynya Project between March and July, in order to find out a good parametrization scheme for the arctic marine environment. They found that a combination of the forms of Efimova (1961) for $L_{\downarrow clr}$:

$$L_{\downarrow clr} = \sigma (T_a + 273.2)^4 (0.746 + 0.066e_a) \tag{5.4}$$

and Jacobs (1978) for $L_{\downarrow all}$:

$$L_{\downarrow all} = L_{\downarrow clr} (1+0.26C) \tag{5.5}$$

gave the best results for longwave radiation. Given different air and surface circumstances in the northern marine terrain, they suggested that the clear-sky atmospheric emissivity was adjusted downward, roughly from 0.746 to 0.7, and the cloud emissivity needed to be increased from 0.26 to 0.275. The formulations were modified as:

$$L_{\downarrow clr} = \sigma (T_a + 273.2)^4 (0.7 + 0.066e_a) \tag{5.6}$$

$$L_{\downarrow all} = L_{\downarrow clr} (1+0.275C) \tag{5.7}$$

From the above equations, it can be seen that downwelling longwave radiation is a function of near surface temperature (i.e. air temperature T_a) and vapour pressure (e_a). An increase in $L_{\downarrow}$ is caused by the effect of clouds expressed by the degree of cloud cover C, which can be linked with sky or weather conditions. Sky conditions provided reflect the observation of total cloud amount. They are typically stratified into four classes based on the amount (in tenths) of cloud covering the dome of the sky: clear (0 to1 tenths), mainly clear (1 to 4 tenths), mostly cloudy (5 to 9 tenths), and cloudy (10 tenths) (National Climate Data and Information Archive, 2004). Besides, rain, drizzle, fog, smoke, ice crystals, snow and other types of atmospheric conditions are existent in this region as well. Therefore, the degrees of cloud cover were related to five weather conditions, including the four sky conditions described above and a condition of 'others' that contains other possible weather phenomenon.

5.3 Testing Methods

Resulting incoming longwave radiation fluxes for each model were generated for both Fen 2006 and 2007 runs, and statistics were compiled to evaluate the relative performance of the two models. Two sets of degrees of cloud cover, one for each run, from the selected model were applied to each other to calculate $L_{\downarrow}$ in order to determine which set of values is better. Following a comparison of the results, the better set was chosen as the representative values corresponding to weather conditions to calculate $L_{\downarrow}$ for the Rail Spur site as a CLASS input in Chapter 6: Modelling Evaporation from Lichen and Moss Tundra.

The primary comparative statistics: mean bias error (MBE) and root mean square error (RMSE), were calculated for both models, together with the index of agreement (d), proposed by Willmott (1982). MBE and RMBE respectively describe the systematic and nonsystematic errors. MBE is useful for identifying when a modelled variable is systematically under or overestimated, while RMSE gives an indication of the overall magnitude of the variation between the individual observations and predictions. The d statistic is a relative measure and is most powerful when used to judge the ability of different models to simulate a given variable, ranging between 0 and 1, with 1 indicating a perfect fit of modelled to measured values (Bellisario et al., 2000). These statistic values are computed by the equations as follows:

$$MBE = \frac{\sum (P_i - O_i)}{n} \tag{5.8}$$

$$RMSE = \sqrt{\frac{\sum (P_i - O_i)^2}{n}} \tag{5.9}$$

$$d = 1 - \left(\frac{\sum_{i=1}^{n} (P_i - O_i)^2}{\sum_{i=1}^{n} (|P_i - \overline{O}| + |O_i - \overline{O}|)^2} \right) \tag{5.10}$$

where P_i and O_i are ith values of the predicted (modelled) and measured quantities respectively, n is the number of observations, $\overline{O}$ is the mean observed value, and the sidebars represent absolute values. Good agreement between observed and modelled data would result in low values for MBE and RMSE, and a high fractional value for d.

5.4 Simulation Results

The objective of this simulation is to relate weather conditions to appropriate degrees of cloud cover, which can be reapplied to calculate longwave radiation for other sites that lack those measurements but have weather information. Fen 2006 and 2007 measured longwave flux data were used to evaluate the two incoming longwave radiation models: traditional (Model 1) and modified (Model 2). The time series data and cumulative fluxes were plotted compared with field measurements, and the corresponding statistics for the two models were also computed. Thereafter, the more accurate model was chosen to generate the degrees of cloud cover for the five weather conditions: clear, mainly clear, mostly cloudy, cloudy, and others. These values are used for the Rail Spur site to calculate longwave radiation, which is lacking there.

5.4.1 Model Comparison

It is known that clouds are one of the main sources for the emission of atmospheric longwave radiation, so that their effects are an important factor to be considered when calculating $L_{\downarrow}$. To see the difference between $L_{\downarrow clr}$ and $L_{\downarrow all}$, $L_{\downarrow clr}$ was calculated for Fen 2007 from May 27 to September 12 (5159 half-hourly data) using the two clear-sky models, and then plotting them against the measured $L_{\downarrow all}$ of the site (Figure 5.1). It can be seen that the simulated $L_{\downarrow clr}$ from both models are very close, and only in a few periods around the lowest values, the values of model 1 is under model 2. Compared to the measured $L_{\downarrow all}$, $L_{\downarrow clr}$ is lowered about one third of the magnitude. This is the part of longwave radiation affected by clouds.

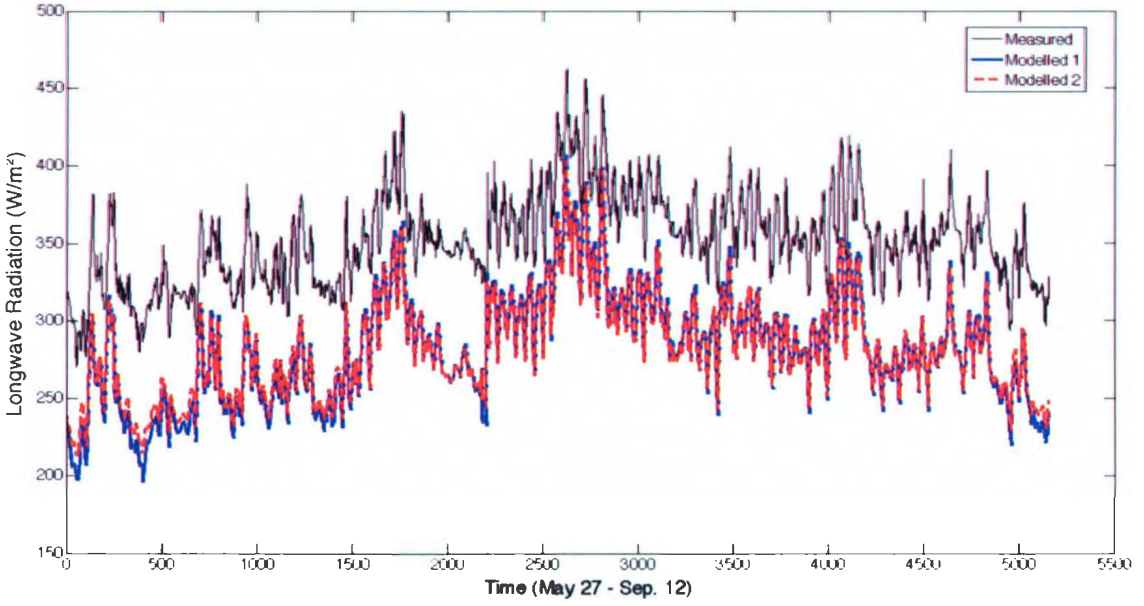

Figure 5.1 Modelled clear-sky longwave radiation versus measured data for Fen 2007.

There are measured $L_{\downarrow all}$ from the Fen site, and the two models to calculate $L_{\downarrow clr}$ dependent on known T_a and e_a. It is convenient to obtain the degree of cloud cover using $L_{\downarrow all}$ and $L_{\downarrow clr}$ values for the two models. When the degrees of cloud cover are separately linked to the weather conditions, five sets of C values are classified for each model. To generate a single set of degrees of cloud cover corresponding to the five weather conditions, the averaged C of each class is calculated as the representative value. The mean C values of the five classes from the two models are shown in Table 5.1. Generally, the degree of cloud cover is increasing with cloud amounts. However, the values shown below are not exactly in that order due to the combination of many weather conditions into the 'others' class. One can also see that the degrees of cloud cover calculated by Model 2 are slightly smaller than those by Model 1. Most of the values are greater than one, which is anticipated by both cloud cover models.

Table 5.1 Calculated degrees of cloud cover related to the five weather conditions for Fen 2006 and 2007 from the two models.

	Clear	Mainly Clear	Mostly Cloudy	Cloudy	Others
Fen 2006					
Model 1	1.1387	1.0747	1.1166	1.1063	1.1280
Model 2	1.0062	0.9382	1.0032	1.0071	1.0331
Fen 2007					
Model 1	1.1118	1.0342	1.0927	1.1621	1.1769
Model 2	0.9112	0.8358	0.9397	1.0408	1.0785

When the degrees of cloud cover are obtained, $L_{\downarrow all}$ is recalculated using both models and compared with the measurements. Figures 5.2 and 5.3 show the modelled and measured $L_{\downarrow all}$ and cumulative fluxes for the Fen site, respectively, and the corresponding statistics are presented in Tables 5.2 and 5.3. For Fen 2006, parts of the modelled $L_{\downarrow all}$ are underestimated and the values from Model 2 are a little higher than those from Model 1, but the cumulative plots for all the three periods are quite well matching. For Fen 2007, both models performed very well in longwave radiation modelling, due to the good fits of the flux and cumulative plots to the measurements. From these figures, it is difficult to tell the difference between one model and the other, because the results are so similar that the two plots overlie each other.

Statistical comparison of measured versus modelled $L_{\downarrow all}$ demonstrates an overall excellent performance by both models. The models have low MBE (less than 2) and RSME (less than 20) values, and high agreement indices (over 0.93). This indicates that the two models are reasonable and acceptable for modelling longwave radiation at the Fen site. Despite the slight difference between them, it is believed that the model with the lowest MBE and RSME, and highest *d* is the best. From the statistical results shown in

a)

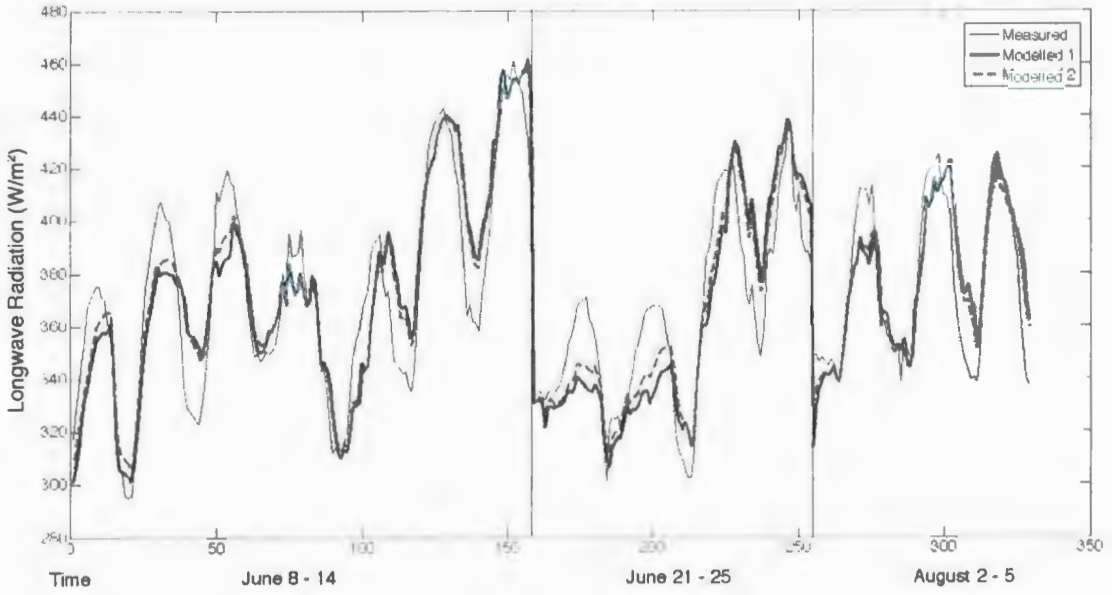

b)

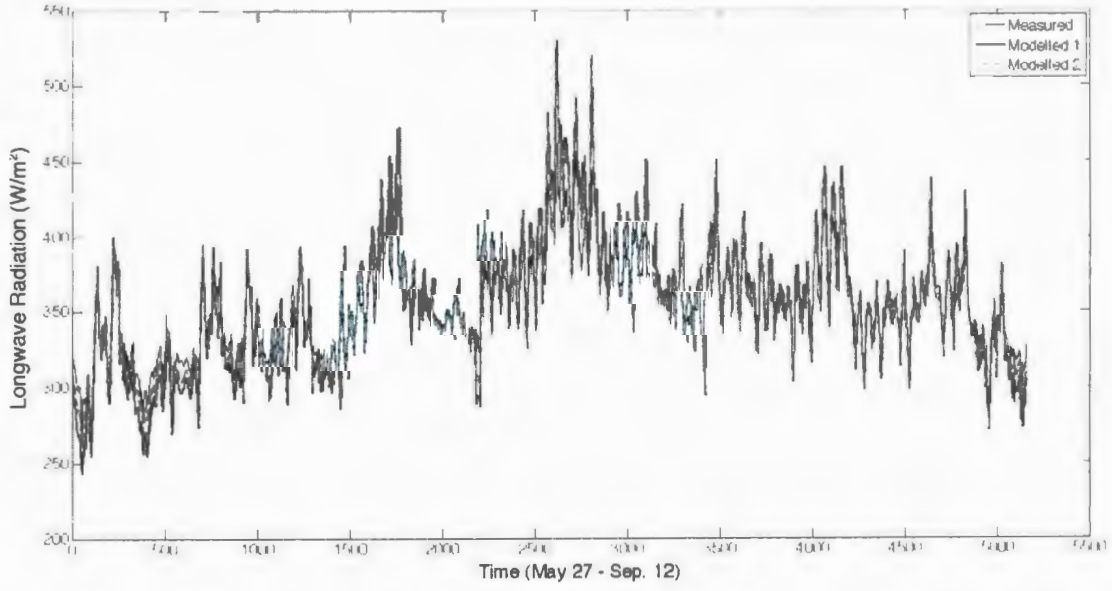

Figure 5.2 Modelled incoming longwave radiation fluxes versus measured data for a) Fen 2006; b) Fen 2007.

a)

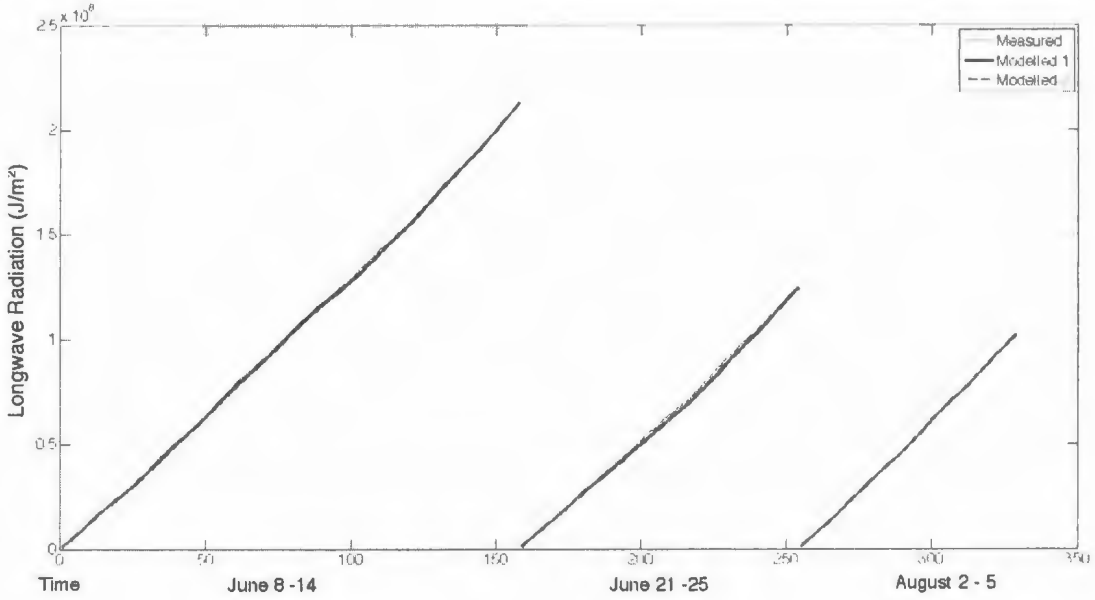

b)

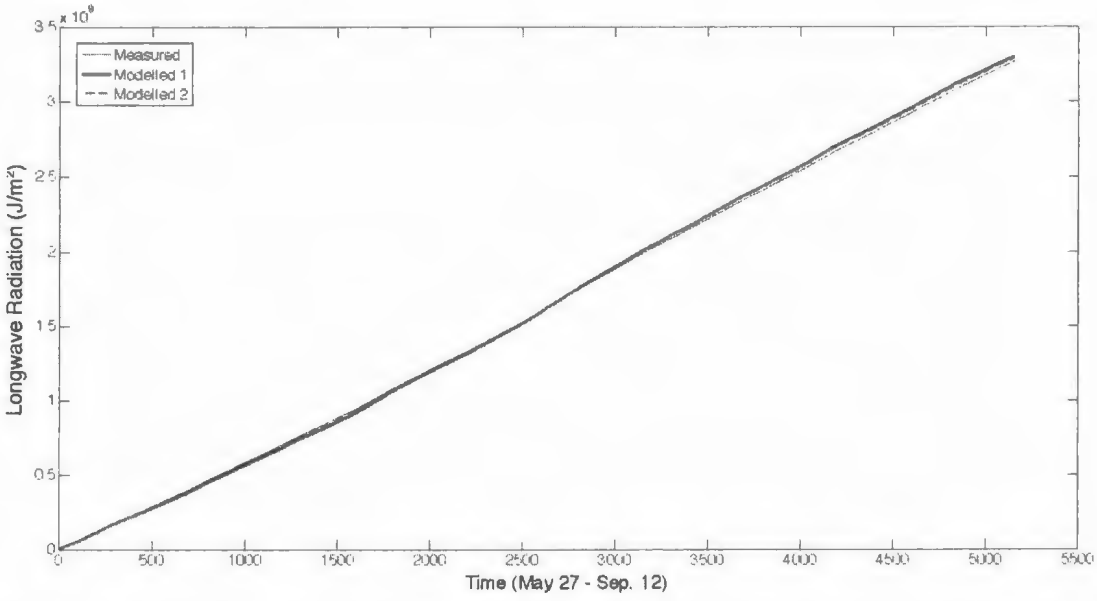

Figure 5.3 Cumulative longwave radiation from modelled versus measured data for a) Fen 2006; b) Fen 2007.

Table 5.2 Statistics for longwave radiation modelling evaluation. The units are W m^{-2}, except n and d, which are dimensionless.

	n	$\overline{O}$	$\overline{P}$	MBE	RSME	d
Fen 2006						
Model 1	329	371.36	370.85	-0.51	17.97	0.938
Model 2	329	371.36	371.61	0.25	15.30	0.953
Fen 2007						
Model 1	5159	347.99	349.06	1.07	17.43	0.947
Model 2	5159	347.99	349.15	1.16	12.42	0.969

Table 5.3 Cumulative longwave radiation comparison of measured and modelled values for Fen 2006 and 2007. The units are J m^{-2}, except errors (%).

	Fen 2006			Fen 2007
	June 8-14	June 21-25	August 2-5	May 27-Sep. 12
Measured	2.127×10^{8}	1.254×10^{8}	1.017×10^{8}	3.268×10^{9}
Model 1	2.129×10^{8}	1.243×10^{8}	1.020×10^{8}	3.298×10^{9}
Bias	2.001×10^{5}	-1.128×10^{6}	3.215×10^{5}	3.051×10^{7}
Error (%)	0.094	-0.900	0.316	0.934
Model 2	2.133×10^{8}	1.251×10^{8}	1.018×10^{8}	3.291×10^{9}
Bias	5.508×10^{5}	-3.389×10^{5}	8.235×10^{4}	2.365×10^{7}
Error (%)	0.259	-0.270	0.081	0.724

the tables, it is apparent that Model 2 performs better than Model 1. Additionally, the cumulative $L_{\downarrow all}$ results show very low total bias for each time period, and all the errors do not exceed 1% of the measured total. Except June 8-14 of Fen 2006, the errors from Model 2 are less than those from Model 1. It is concluded that Model 2 is the more accurate model for the Canadian northern marine environments.

5.4.2 Degree of Cloud Cover

To obtain $L_{\downarrow all}$ for the Rail Spur site, the degrees of cloud cover calculated in Subsection 5.4.1 need to be taken into consideration. Two sets of C values are available from Model 2, one for each year run. It is necessary to determine the better set of values by applying the degrees of cloud cover into a different dataset. A feasible way is to substitute the set of Cs generated from one year run into the other year run, and to compare the results with the observations. The Cs (i.e. 0.9112, 0.8358, 0.9397, 1.0408, 1.0785) from Fen 2007 were first employed to calculate $L_{\downarrow all}$ for Fen 2006, and then the Cs (i.e. 1.0062, 0.9382, 1.0032, 1.0071, 1.0331) from Fen 2006 were employed to calculate $L_{\downarrow all}$ for Fen 2007. The comparisons of modelled with measured $L_{\downarrow all}$ for each year are presented in Figures 5.4 and 5.5, and the corresponding statistics are shown in Table 5.4.

From the plots in Figure 5.4, an underestimate of the fluxes by the model is detected, although the cumulative energy is very close, the estimated values being only a little lower. MBE, cumulative biases, and errors give negative values for these three sections. Compared to the statistics shown in Table 5.2 and 5.3, these values are higher, which indicates a weaker estimation from this model using the degrees of cloud cover from Fen 2007. In Figure 5.5, the data periods around the peaks are slightly overestimated, and the cumulative values are lower than the measurements during the first one third of the entire period, but are higher than the measurements in the remaining time. The statistics for Fen 2007 show a good agreement between the modelled and measured data. The agreement index (0.962) is higher than the result for Fen 2006. These

statistical comparisons imply a fact that the Cs obtained from Fen 2006 are improved over the values from Fen 2007.

a)

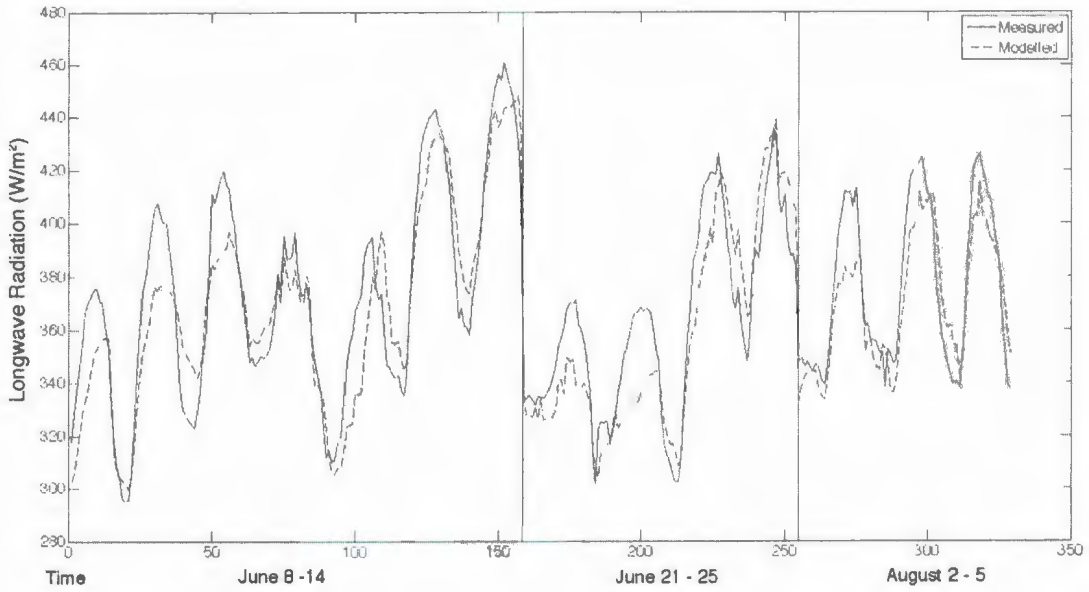

b)

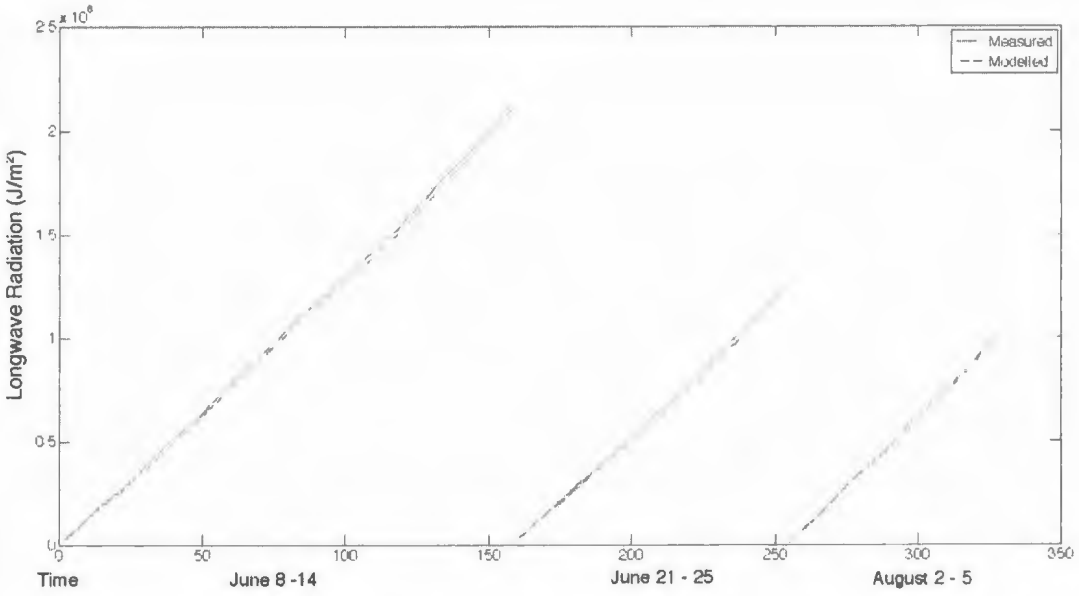

Figure 5.4 Modelled incoming longwave radiation versus measured data for Fen 2006. a) Radiation flux; b) Cumulative energy.

a)

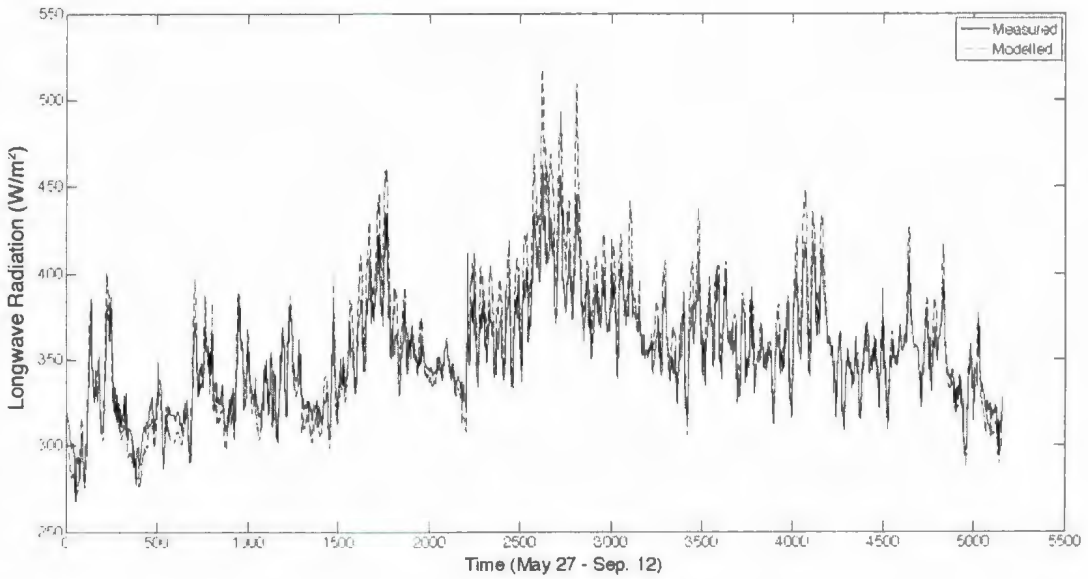

b)

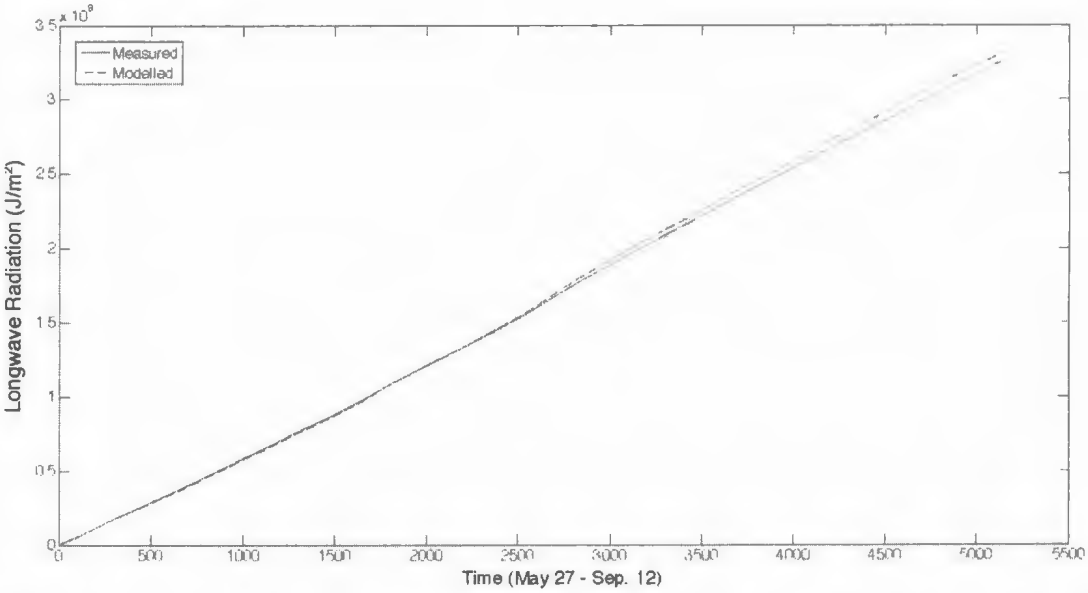

Figure 5.5 Modelled incoming longwave radiation versus measured data for Fen 2007. a) Radiation flux; b) Cumulative energy.

Table 5.4 Statistical and cumulative comparison for Fen 2006 and 2007. The units for $\overline{P}$, MBE, and RSME are W m^{-2}, for Modelled and Bias are J m^{-2}, and the others are dimensionless.

	$\overline{P}$	MBE	RSME	d	Modelled	Bias	Error (%)
Fen 2006	366.10	-5.25	16.63	0.944			
June 8-14					2.100×10^{8}	-2.711×10^{6}	-1.274
June 21-25					1.236×10^{8}	-1.848×10^{6}	-1.473
August 2-5					1.000×10^{8}	-1.663×10^{6}	-1.636
Fen 2007	352.05	4.06	14.01	0.962	3.319×10^{9}	5.103×10^{7}	1.562

Consequently, the degrees of cloud cover generated from Fen 2006 are chosen as the representative C values for further longwave radiation calculations. The five weather conditions: clear, mainly clear, mostly cloudy, cloudy and 'others', are therefore denoted by the values of 1.0062, 0.9382, 1.0032, 1.0071, and 1.0331, respectively. The model to be used to simulate $L_{\downarrow all}$ for Rail Spur will be the modified combination model by Hanesiak et al. (2001) for the arctic marine environment where sea-ice effects are severe. The simulation results illustrate that this longwave radiation modelling is successfully performed when combined with the accurate estimates of degrees of cloud cover.

6. Modelling Evaporation from Lichen and Moss Tundra

Lichens and mosses are typical non-vascular plants that are growing in the northern Canadian wetland tundra area. One of the characteristics of this type of vegetation is that evaporation of water is not by transpiration within the vascular pathways, such as roots, stems, branches, and leaves, but is directly from the plants depending on the canopy moisture capacity. This generates a different control on evaporation and makes the surface act in a very different manner with respect to moisture transport in comparison to a vascular dominated area. At Rail Spur (58° 09' 38" N, 94° 08' 35.4" W), 80% of land coverage is lichen and moss species. However, the current CLASS formulation considers all vegetated surfaces to be vascular with evapotranspiration limited predominantly by aerodynamic and canopy resistances (Comer et al., 2000). This appears adequate for the sedge Fen site, but definitely not for Rail Spur. Therefore, appropriate modifications of the canopy resistances for lichen and moss are required in CLASS to fit the non-vascular vegetation properties, in order to improve the model performance. To evaluate the CLASS simulation results, the Penman-Monteith approach was employed in this chapter.

The same canopy resistance modifications were applied to the Penman-Monteith model as well. Additionally, the daily averaged runoff generated from CLASS was compared to that from the Deer River Basin discharge published on WSC.

6.1 Canopy Resistance

It is known that there are no stomata on lichens or mosses, and these non-vascular species dominate peat polygons within a network of ice-wedge cracks in the Churchill region. The Rail Spur site is an example of a polygonal peat plateau. Figure 6.1 displays the lichen and moss tundra on the peat plateau near Rail Spur. In the photo, the light is lichens and the dark is mosses. They are pretty low on the ground, with the average height of 10 cm.

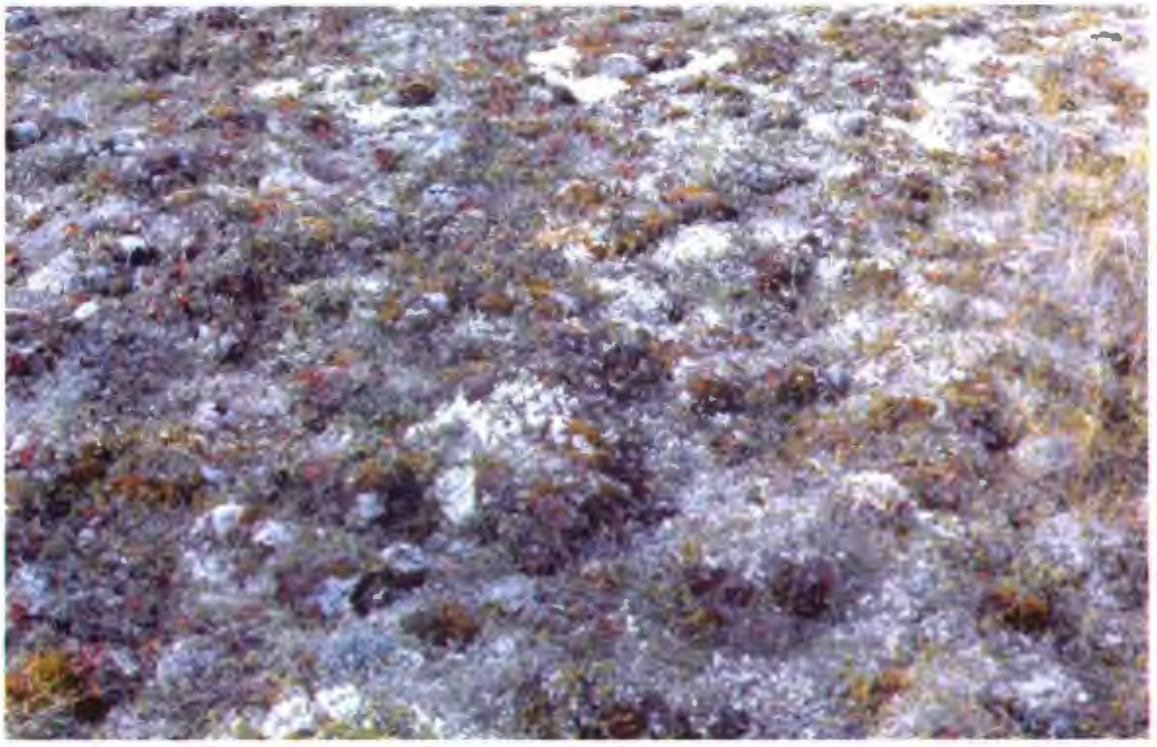

Figure 6.1 Lichen and moss tundra on the peat plateau near Rail Spur. Photo taken on August 27, 2007.

Despite the lack of stomata, lichen and moss do have a canopy resistance. The canopy resistance is usually defined as the combined resistance of all the stomata acting in parallel. In a vascular canopy, the resistance is under the physiological control of the plants through stomatal opening and closing. In non-vascular canopies, the canopy resistance relies on the passive control of the vegetation and represents the degree of difficulty to get water within the canopy up to the surface where it can be evaporated (Bello, November 5, 2007). Water transport to the evaporating surface is believed to be supplied by capillarity, which is dependent upon water table depth and vegetation wetness. The exterior of the plants have microscopic 'rills' that act as capillary tubes (Hayward and Clymo, 1983). As long as the supply of water is close to the surface, and the evaporation demand for water does not exceed the rate of capillary supply, then high evaporation can be maintained (Comer et al., 2000).

Based on the field experiments carried out in Churchill, the canopy resistance for lichens is expressed by the following relation (Bello, November 5, 2007):

$$R_c = -70.8 \cdot \ln(\frac{S}{S_m}) + 59.9 \qquad (6.1)$$

where S is the actual amount of water stored in the lichen canopy (mm) for a given time (i.e. half an hour), and S_m is the maximum amount of water the lichen canopy can store (mm), that is, canopy moisture storage capacity. This relation implies that the canopy resistance is only a function of canopy moisture. It is not affected by insolation, temperature, vapour pressure deficit (VPD), or CO_2 concentration, because there are no stomata to be affected by these variables.

To solve for S, it is assumed that there is no direct throughfall coefficient, which denotes the canopy gap fraction or sky view factor, and therefore all rain falling on the canopy is intercepted. Given the surface drainage, empirical tests in the laboratory indicate that all drainage occurs within one hour after the cessation of rainfall (Bello, November 8, 2007). So very little error is introduced by supposing that all rainfall which is not intercepted by the canopy will drain immediately. A variety of rainfall interception models can be applied to calculate S, such as Rutter's model, or Grace's version. The Liu model (Liu, 1997) for the prediction of rainfall interception is used in this chapter (see Subsection 6.3.2 for details).

The canopy storage capacity S_m is the maximum amount of water that the canopy can hold after gravity drainage. For non-vascular plants, S_m is related to the above ground biomass (AGB), not the leaf area index (LAI). The experiments carried out by Ashley Gade (honours undergraduate student of the University of Manitoba) near Churchill in 2005 (Bello, November 5, 2007) on lichens estimate that:

$$S_m = 2.15\ \mathrm{AGB} \tag{6.2}$$

where AGB is above ground biomass measured in kg m^{-2}, and S_m is in units of kg m^{-2} of water or mm of water. However, no information about AGB in the interior of the Hudson Bay Lowland where Rail Spur is located has been provided. Instead, the average lichen AGB of 2 kg m^{-2} near the Churchill Northern Studies Center (CNSC) is used for the Rail Spur site. The canopy storage capacity for lichens is calculated as 4.3 kg m^{-2}, or mm.

It is noted that no experiments have been carried out on the canopy resistance of mosses, so it is assumed that the relationship between R_c and S/S_m is the same as that for

lichens. Mosses hold more water per unit biomass than lichens and also have larger AGB than lichens. In Ashley Gade's research on the peat plateau, it was found that for the three dominant mosses S_m was related to AGB as:

$$S_{m1} = 12.2\ AGB_1 \tag{6.3}$$

$$S_{m2} = 8.5\ AGB_2 \tag{6.4}$$

$$S_{m3} = 3.6\ AGB_3 \tag{6.5}$$

where the subscript numbers indicate three different mosses. The above ground biomass ranged from AGB_1 = 1-1.75 kg m^{-2} for moss 1, AGB_2 = 1-2.25 kg m^{-2} for moss 2, and AGB_3 = 4.5-6.75 kg m^{-2} for moss 3. The mean value of AGB is used to calculate a representative S_m for each moss.

Unfortunately, no study has investigated the proportional coverage of lichens and each moss on the peat plateau at Rail Spur. But on the peat plateau near the CNSC the surface is covered about 30% with lichen, 15% with moss 1, 5% with moss 2, 25% with moss 3, and remaining 25% with vascular plants for which there are no data or experimentation information. The non-vascular coverage of 75% was converted into 100% coverage for the Rail Spur site, which means the entire surface at Rail Spur is occupied by lichens and mosses. The weighted total canopy moisture storage capacity, integrated from each portion, is 12.746 mm. The vegetation proportions on the peat plateau do not change significantly over months, and the biomass of lichens and mosses does not vary seasonally. Hence, the computed S_m value for lichen and moss tundra is reasonably applicable to the whole year simulations.

6.2 Modified CLASS Model

In current CLASS, all vegetation categories are treated as vascular plants, from which the evapotranspiration is through the vascular system into the atmosphere. The evaporation of water for these vascular plants takes place via stomata in the leaf surface. This process is controlled by the canopy stomatal resistance, which relies on the light intensity, ambient CO_2 concentration, VPD, leaf temperature, and leaf water content. But non-vascular plants: lichens and mosses, do not have stomata. Those functions in CLASS for the stomatal resistance responding to light, temperature, VPD, and soil moisture suction are never suitable to be employed for lichens and mosses. Thus, a new category of non-vascular plants is required for CLASS.

Replacing the grass category with non-vascular vegetation in the CLASS initialization file modifies the model and takes advantage of the original initialization format. The data period for Rail Spur is from July 16, 2006 to December 11, 2007 (12314 hourly data), about one and half years, which is long enough for the evaporation modelling. Measurement heights for wind speed, and temperature and humidity are 3 m and 2 m, respectively. The average height of lichen and moss is 0.1 m, so the natural logarithm of the roughness length for them is -4.605. The LAIs and rooting depth are set to zero, as non-vascular plants have neither true leaves nor true roots. All the coefficients governing the stomatal resistance in the file are assumed to be zero because of no stomata. The soil type at Rail Spur is also peat, whose characteristics are fibric, hemic and sapric for the three soil layers. Soil temperatures and moistures for the top two layers were measured in the field. The temperature was extrapolated to the mid-point of the

third layer as its soil temperature, and it was assumed that the moisture was frozen in that layer.

CLASS has one subroutine, named by "CANALB", which controls the canopy stomatal resistance. The new formulation of the canopy resistance for lichens is substituted into this file for the former functions of the vascular plants. When recalling the canopy resistance equation for lichens described in the last section, the only required inputs are S and S_m. S_m for the Rail Spur site has been calculated as 12.746 mm. CLASS generates the average liquid water stored on canopy for each half an hour, with the variable name of "RAICAN". It is not difficult to rewrite those codes related to the canopy resistance in this subroutine by:

$$R_c = -70.8 \cdot \ln(\frac{RAICAN}{12.746}) + 59.9 \qquad (6.6)$$

where RAICAN is in mm. Note that RAICAN should be recalled as a variable because it was not referred to in this file. The main problem with this formula is that the maximum water holding capacity for RAICAN is unknown. It is assumed to be 12.746 mm, but CLASS may cause it to drop off much below this value, so that RAICAN might never reach it.

Based on these modifications for non-vascular plants, CLASS can be used to run the datasets collected from wetland lichen and moss tundra as from Rail Spur. However, to evaluate the accuracy of the evaporation obtained from this modified CLASS model, a calculative evapotranspiration model – the Penman-Monteith equation – is employed in the subsequent section, and the results from both models are compared.

6.3 Application of the Penman-Monteith Model

Evapotranspiration includes evaporation of liquid water from rivers and lakes, bare soil, vegetative surfaces, and from within the leaves of plants (transpiration), and sublimation from ice and snow surfaces (Dingman, 2002). Owing to the fact that direct measurement of evaporation is difficult and expensive, numerous estimation approaches have been developed using measurable quantities, such as precipitation, streamflow and temperature. The Penman-Monteith model, which combines evaporation from a free-water surface and from a vegetated surface, is the most widely used method for estimating evapotranspiration. In this section, the Penman-Monteith model will be applied to the lichen and moss tundra, and be supplemented with the canopy resistance that fits the specific vegetated wetland surface of interest.

6.3.1 Model Description

Evapotranspiration connects the water and energy balances, so the use of the mass transfer and energy balance approaches is a good application. Penman (1948) first proposed that these two approaches could be combined to generate an evaporation equation that did not require surface temperature. This derivation assumes no water advected energy, no ground heat conduction, and no heat storage effects. Later on, Monteith (1965) modified the Penman equation to represent the evapotranspiration rate from a vegetated surface by incorporating canopy conductance. The modified combination model is known as the Penman-Monteith model:

$$ET = \frac{\Delta \cdot (K + L) + \rho_a \cdot c_a \cdot C_{at} \cdot e_a^* \cdot (1 - W_a)}{\rho_w \cdot \lambda_v \cdot |\Delta + \gamma \cdot (1 + C_{at} / C_{can})|} \tag{6.7}$$

where ET is the evapotranspiration rate in m s^{-1}, K and L are net shortwave and longwave radiation in MJ, c_a is the heat capacity of air, assigned a constant of 1.00×10^{-3} MJ kg^{-1} K^{-1}, W_a is relative humidity in fraction, ρ_w is the mass density of water, equal to 1.00×10^{3} kg m^{-3}, and the other terms are specified below. Note that the units used are not fixed, and they vary dependent on one another.

The maximum vapour pressure that is thermodynamically stable is called the saturation vapour pressure (e^*), which is a function only of temperature (Dingman, 2002). The saturation vapour pressure at the air temperature is calculated as:

$$e_a^* = 0.611 \cdot \exp\left(\frac{17.3T_a}{T_a + 237.3}\right) \tag{6.8}$$

where e_a^* is in kPa, and T_a is in °C. This equation is suitable for air temperatures greater than 0 °C, while for the case of temperatures less than 0 °C, the relation differs slightly:

$$e_a^* = 0.611 \cdot \exp\left(\frac{21.87T_a}{T_a + 265.5}\right) \tag{6.9}$$

This low temperature relation is rarely presented in textbooks and results in lower saturated vapor pressures when compared to its above zero degree counterpart (Snelgrove, 2002).

The slope of the relation between saturation vapour pressure and temperature is designated Δ. Its value can be found by taking the derivative of the saturation vapour pressure equation:

$$\Delta \equiv \frac{de^*}{dT} = \frac{2508.3}{(T + 237.3)^2} \cdot \exp\left(\frac{17.3T}{T + 237.3}\right) \tag{6.10}$$

where Λ is in kPa K^{-1}, and T is the air temperature in °C.

It is known that temperature, pressure and density in the atmosphere are related via the Ideal Gas Law:

$$\frac{p}{T_a \cdot \rho_a} = R_a \tag{6.11}$$

where p is atmospheric pressure in kPa, T_a is air temperature in K, ρ_a is the mass density of air in kg m^{-3}, and R_a is the gas constant for air. For the units given, the value of R_a is 0.288, so that ρ_a can be rearranged as:

$$\rho_a = \frac{p}{R_a T_a} = \frac{p}{0.288 \cdot (T_a + 273.2)} \tag{6.12}$$

where T_a is in °C.

C_{at} is the atmospheric conductance for water vapour, and is defined explicitly as:

$$C_{at} \equiv \frac{v_a}{6.25 \cdot \left[\ln\left(\frac{z_m - z_d}{z_0}\right)\right]^2} \tag{6.13}$$

where C_{at} is in m s^{-1}, v_a is wind speed in m s^{-1}, z_m is the height at which wind speed and air vapour pressure measured, z_d is the zero-plane displacement, and z_0 is the roughness height of the surface. z_m, z_d and z_0 are in the same units, and z_d and z_0 can be approximately related to the height of vegetation, z_{veg}, as:

$$z_d \quad 0.7\, z_{veg} \tag{6.14}$$

$$z_0 \quad 0.1\, z_{veg} \tag{6.15}$$

At Rail Spur, z_m is 3 m, and z_{veg} is 0.1 m for lichen and moss.

The latent heat of vaporization, λ_v, decreases as the temperature of the evaporating surface increases. This relation is given by:

$$\lambda_v = 2.50 - 2.36\times10^{-3}\cdot T \tag{6.16}$$

where λ_v is in MJ kg^{-1}, and T is set to T_a in °C.

γ is a factor called the psychrometric constant, but it is not strictly constant and follows this definition:

$$\gamma \equiv \frac{c_a \cdot p}{0.622\lambda_v} \tag{6.17}$$

where γ is in kPa K^{-1}, c_a is equal to 1.00×10^{-3} MJ kg^{-1} K^{-1}, p is in kPa, and λ_v is in MJ kg^{-1}.

C_{can} is canopy conductance, whose inverse term ($1/C_{can}$) is the canopy resistance (R_c). For lichens and mosses at Rail Spur, the canopy resistance was discussed in the last section. The only factor affecting R_c is the canopy moisture storage (S), which can be calculated by rainfall interception models.

6.3.2 Canopy Storage

Solving for the actual amount of water stored in the canopy, S, at any point in time requires the application of a rainfall interception model. The Liu model, developed in this thesis, is used here to calculate the amount of rainfall intercepted by lichen and moss. The dependent variables required for the model are canopy storage capacity (S_m), precipitation (P), ground coverage (k), the canopy dryness index (D), and evaporation between rainfalls (E). The canopy storage function at any time during rainfall is defined as:

$$S = S_m \left[1 - D_0 \cdot \exp\left(\frac{-kP}{S_m} \right) \right] \tag{6.18}$$

where D_0 is the canopy dryness index before the rainfall. D ranges from 0 (saturated) to 1 (fully dried), defined as:

$$D \quad 1 \quad S / S_m \tag{6.19}$$

From these formulae, a time series equation for S can be induced:

$$S_i = S_m \left[1 - D_{i-1} \cdot \exp\left(\frac{-k(P_{i-1} + P_i)}{S_m} \right) \right] \tag{6.20}$$

where the subscript i indicates ith values of the quantities, and i-1 indicates the values at the ith start. Also,

$$D_i \quad 1 \quad S_i / S_m \tag{6.21}$$

Usually, D is set to 1 at the beginning (i.e. D_0 1), which means the canopy is dried out before the first rainfall. Between rainfalls, the intercepted water from the previous event is vaporizing to the atmosphere, so S is decreasing over time until the next event begins. If the time between the two events is enough to evaporate all the intercepted water held by canopy, there would be no carry-over effect from the former rainfall event to the next (Liu, 1997). That is, D is reset to 1 when the new rainfall starts. Otherwise, the former event would have an impact on the next event, which is reflected by $D < 1$, or $S > 0$.

On lichen and moss tundra, the direct throughfall coefficient is assumed to be 0, which means that 100% of ambient rainfall strikes the canopy, and none misses and reaches the ground directly. Ground coverage k is therefore assigned 1. Drainage from the canopy does not start until $S > S_m$. Once $S > S_m$ drainage begins and it increases

exponentially with S - S_m. All the lab experiments on lichens indicate that because of drainage, S will return to S_m within about 70 minutes (Bello, November 8, 2007). Hence, it is simply assumed that if the rain was of sufficient magnitude to raise S over S_m, then S - S_m drained to the soil immediately, and S = S_m in the canopy. This is not a good assumption for forests, because drainage might persist for several days, and evaporation and drainage would be occurring simultaneously. But it is reasonable for lichen and moss tundra.

The evaporation E is the only manner of intereception loss from the canopy. It is the integral of the free water evaporation rate (e) over time, and e is calculated using the Penman model:

$$e = \frac{\Delta \cdot (K + L) + \rho_a \cdot c_a \cdot C_w \cdot e_a^* \cdot (1 - W_a)}{\rho_w \cdot \lambda_v \cdot (\Delta + \gamma)} \tag{6.22}$$

where all the parameters are in the same units as that used in the Penman-Monteith model, and e is in m s^{-1}. As e does not vary with time, the evaporation during a given time T is expressed by:

$$E = \int e dt = e \cdot T \tag{6.23}$$

Thus, between rainfalls, S is decreasing with the relation shown as:

$$S_t \quad S_{t-1} - e \cdot T_t \tag{6.24}$$

where T_t is the time between the two points associated with S_{t-1} and S_t. In the case that there is a moisture deficit in the canopy ($S < S_m$) before a rain, the deficit S S_m will exist to be replenished by the next rain. If the amount of the rain is less than S - S_m, the canopy will not be saturated when the evaporation subroutine starts.

6.4 Simulation Results

Based on the modification of canopy resistance for lichen and moss, CLASS generated the latent heat flux for each half an hour, and the Penman-Monteith model calculated the evaporation rates at the same timescale. Other accompanying assumptions were also made along with this modification. To evaluate the simulation results, a comparison of the two models was performed, and the daily average runoff from CLASS was compared to the published discharge of the Deer River basin. In the meantime, the corresponding differences (MBE, RMSE, and cumulative bias) between them were calculated to give a quantitative measure of goodness of fit.

6.4.1 Evaporation Comparison

To ease the comparison of the results from CLASS and the Penman-Monteith model, the latent heat fluxes generated from CLASS were converted to evaporation rates with a simple conversion equation (Vakkilainen and Karvonen, 2005):

$$1 \text{ W m}^{-2} = 0.0352 \text{ mm day}^{-1} \tag{6.25}$$

Sufficient data period, from July 16, 2006 to December 11, 2007, was provided at the Rail Spur site for the evaporation modelling. The evaporation rates and the cumulative evaporation from both models are presented in Figures 6.2 and 6.3, respectively.

From Figure 6.2, it can be seen that the plots from the two models are quite similar, and the magnitudes of the x-axis are the same. They both show that the evaporation rates in summer are very high and there is almost no evaporation in winter. CLASS has simulated negative values in the winter time, which might be because the extremely low temperatures in Churchill affect the specific humidity and vapor pressures.

a)

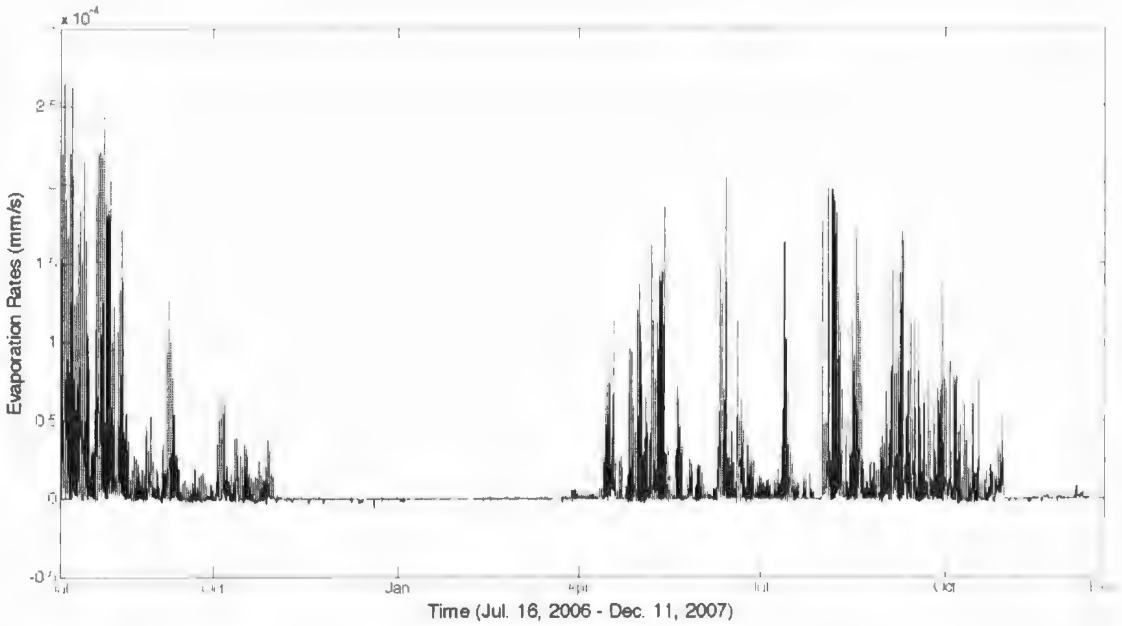

b)

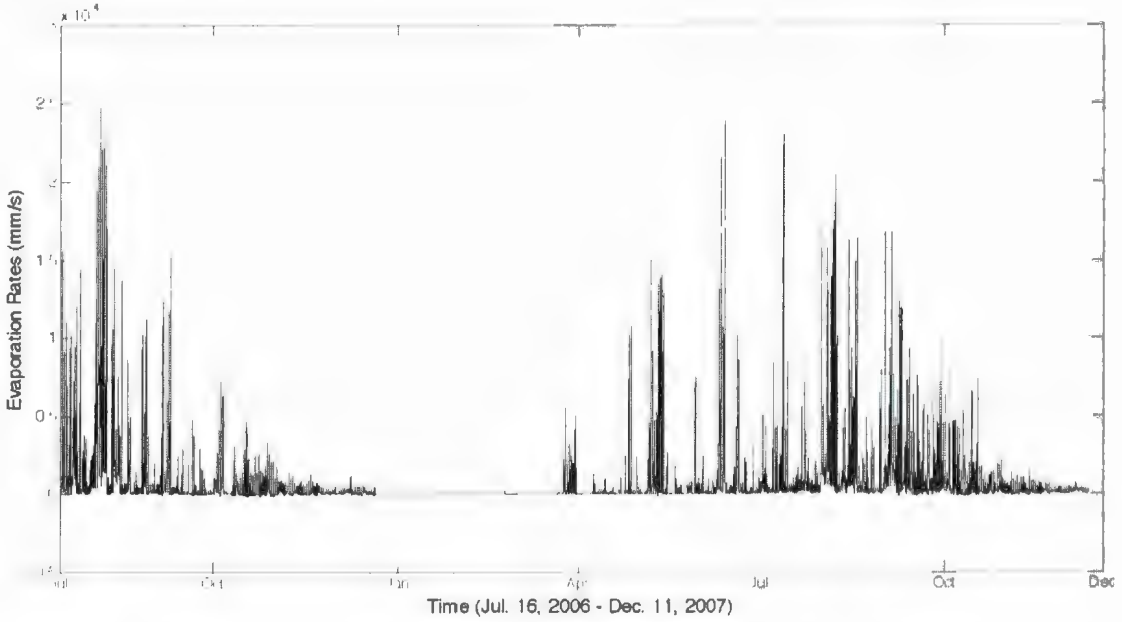

Figure 6.2 Modelled evaporation rates from a) CLASS; b) the Penman-Monteith model.

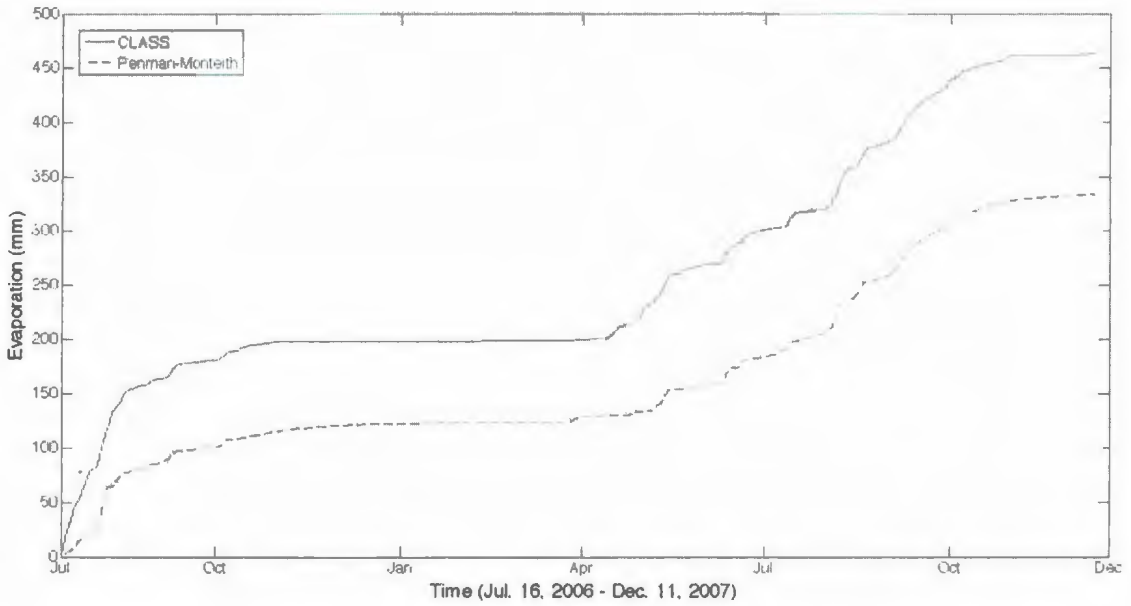

Figure 6.3 Cumulative evaporation from CLASS versus the Penman-Monteith model.

However, it is difficult to tell the differences between these evaporation rates plots, but the cumulative plots show a noticeable evaporation difference throughout this one and half years. The evaporation generated from CLASS is always higher than that from the Penman-Monteith model, although their shapes are similar, which means the evaporation trend during this time period is the same. The computed MBE, RMSE and cumulative bias between the two models are 2.906×10^{-6} mm s^{-1}, 1.966×10^{-5} mm s^{-1}, and 128.83 mm, respectively. MBE and RMSE are not high, as all the rates from both models do not exceed 3×10^{-4} mm s^{-1}, and the cumulative bias does indicate a big difference: the Penman-Monteith value is lower by 27.83% of CLASS.

From Figure 6.3, it is observed that the slope from CLASS is higher than that from the Penman-Monteith model at the beginning, and they become nearly parallel for the rest of the time period. This indicates that the big difference between the two

modelling results mostly occurred at the beginning. The fact is that there were differences between the initial canopy moisture content for both models. It was assumed that the plants were dry before the modelling in the Penman-Monteith model, while CLASS would not initialize the canopy moisture in that situation considering the soil moisture. Actually, the soil at Rail Spur was pretty wet in July 2006, due to large snowmelt after the melting season, and the lichen and moss canopy must intercept the melting water that did make canopy storage change but was not counted in the precipitation. Given the measured data for precipitation, the models do not include the precipitation type as rain versus snow, but this is acceptable since there is little energy in the winter for evaporation.

To determine the effect of the initialization, another plot with only the second year (2007) of data is created (Figure 6.4), and the bias error is calculated. The cumulative bias is 53.77 mm, comprising 41.73% of the total bias. Thus, 58.27% of the

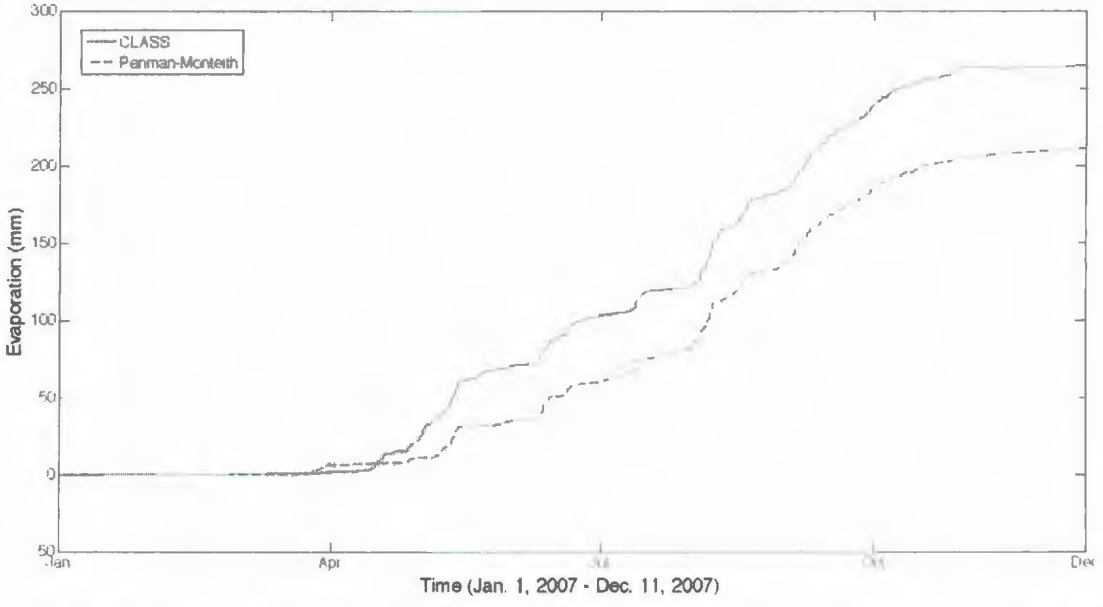

Figure 6.4 Cumulative evaporation from CLASS versus the Penman-Monteith model for 2007.

difference is caused by the inappropriate initial conditions. From the plot, it can be seen that the mismatching starts after April, when the snow was ready to melt and the soil got wet. In this situation, the modified Penman-Monteith model cannot consider the soil moisture and snowmelt factors, so evaporation was underestimated during the melting season until it was finished.

One reason for the difference between the two models may be the effect of the atmospheric conductance (C_{at}) that was computed for the Penman-Monteith model. In the calculation, C_{at} was considered to be under neutral atmospheric conditions, but this phenomenon is generally not valid for natural environments. Either stable or unstable conditions would affect C_{at} values. To solve for this problem, a feasible way is to induce the factors that are related to C_{at} from CLASS into the Penman-Monteith calculations, since CLASS simulates C_{at} based on a variety of possible situations. This initiative requires more investigations into CLASS codes and its subroutines, and will be carried out in future research.

Another reason might be the assumptions concerning of the ground cover. The ground information used was from the peat plateau located near CNSC, not from Rail Spur, the site for modelling evaporation. The percentage coverage is probably different, so that the canopy storage capacity calculated for lichen and moss was either bigger or smaller than the real value. In addition, the assumption that the canopy resistance function for lichens was also suitable for mosses, had not been examined by experiments for its reality. All these assumptions would result in simulation errors, even having a cumulative effect.

6.4.2 Runoff Generation

The production of runoff in the continuous permafrost area of continental Canada has been studied for decades. It was found that the frozen ground is relatively impervious to water movement, and the runoff from subarctic wetland basins is large during snowmelt seasons but with generally long recessions; even so flow can cease entirely in the summer except in response to rainfall (Roulet and Woo, 1988). As one variable of the outputs from CLASS, runoff is the grid cell average water excess from surface outflow and bottom drainage, in the unit of kg m^{-2} s^{-1} or mm s^{-1}. Due to the large evaporative loss of water from wetland tundra, the produced runoff is less than that from other land types. However, this is very preliminary work and beyond the scope of the thesis. The WATFLOOD runoff generation parameters were not employed in CLASS. This has the effect of increasing the evaporation from the model (Snelgrove, 2002).

CLASS can only run an individual point on the surface, so the generated runoff only covers the limited grid cell where the point is located. The runoff generated from CLASS is compared to the Deer River basin outlet discharge from WSC (Figure 6.5), along with a cumulative comparison (Figure 6.6). The basin outlet station at Deer River North of Belcher has collected daily discharge for 30 years, from 1978 to 2007. As the outlet discharge is contributed by the whole basin, the flow should be divided by the basin area (1890 km^2) when compared to the results of CLASS. A problem for this comparison is that the discharge data for 2006 are not continuous, of which July and most of August are missing. Thus, the comparative time was adjusted to a period of August 30, 2006 to December 11, 2007 (469 daily data) to fit both datasets.

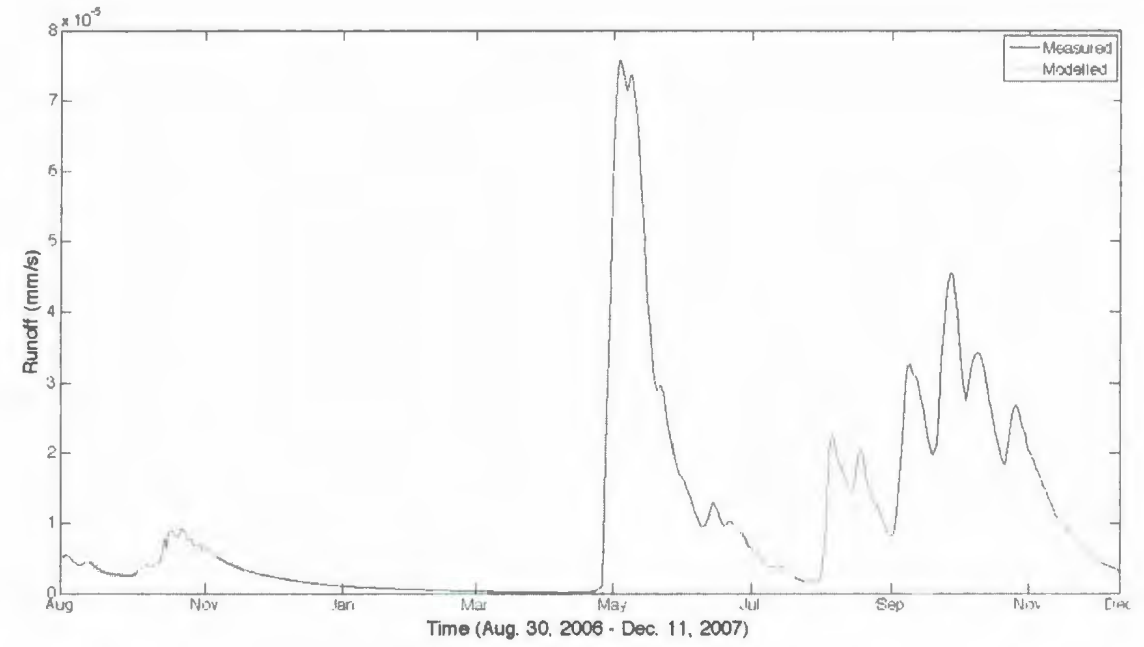

Figure 6.5 Daily average runoff generated from CLASS versus Deer River basin discharge.

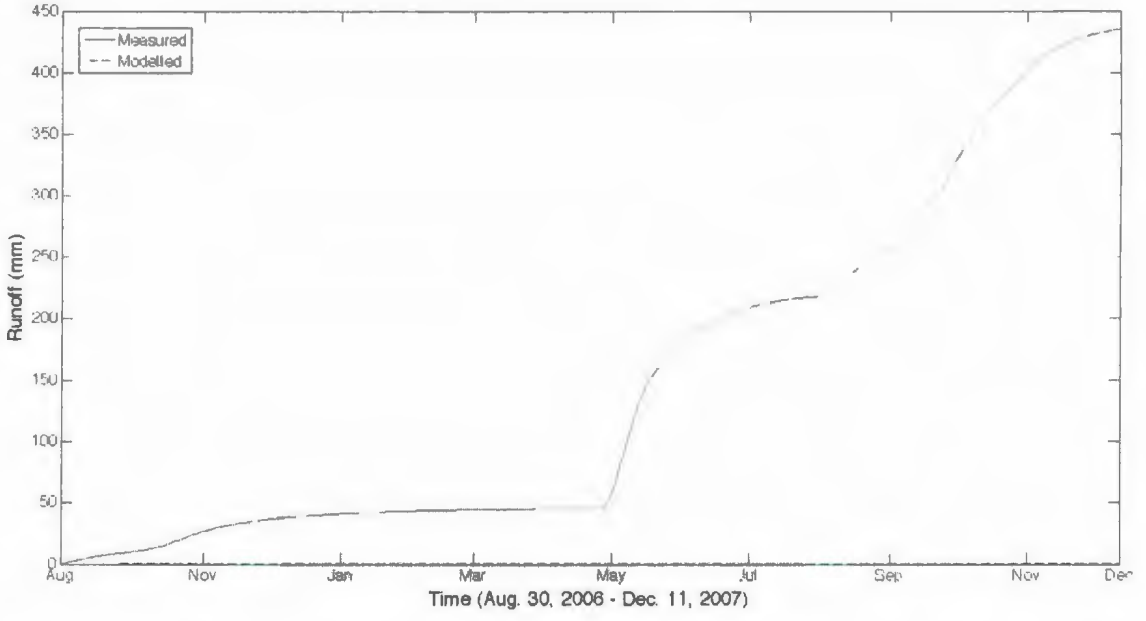

Figure 6.6 Cumulative runoff generated from CLASS versus Deer River basin discharge.

It seems only the basin discharge was presented in Figure 6.5, as the runoff from CLASS is so small that at most some dots can be detected. The basin discharge clearly shows a seasonal trend for runoff generation. The values are low at the beginning because the summer rainfall was over and most of water was lost from evaporation. Almost no runoff was produced during the winter time. The peak values occurred around May 2007 due to snowmelt, and around September 2007 due to rainfalls. From the cumulative plots, it can be seen that the CLASS generated runoff is still much lower than the basin discharge, even accumulated though the entire period. The cumulative bias was calculated as 435.32 mm. The winter and spring periods are anomalous because snow is not considered in the model. The assumption is that all the moisture that drips through the model runs off.

This part of results and analysis is beyond the scope of the thesis work, since there was no time to properly exercise the model capabilities. However, this section provides a good jumping off point for future research.

7. Discussion and Conclusion

Predicting evaporation from a wetland lichen and moss tundra in Churchill, Manitoba, was the goal of this research. CLASS was the major model used to simulate the energy and water balances. To efficiently evaluate the results from CLASS, comparisons with field measurements were applied both to flux data and cumulative values. Due to the fact that lichens and mosses are non-vascular plants, which do not have stomata to transpire water, their canopy resistance is different from that of vascular plants. It is only dependent on the canopy moisture storage, not insolation, temperature, vapor pressure deficit, or CO_2 concentration. A modification in canopy resistance made for lichens and mosses was proposed to fit this property. Along with CLASS, the Penman-Monteith model was used to calculate evaporation as a comparative approach.

Energy and water balances are primary concepts for modelling evaporation, because evaporation is the connecting term of both functions. Based on these balance principles, CLASS ran the 2007 growing season Fen data as a test of the model. It was observed that the components of the energy balance formed a closure, but there were

some discrepancies when compared to observations. High quality measurements are necessary for evaluating the model, but unfortunately, the measured Q_H and Q_E are not reliable to be used to assess the simulation results due to the instrumentation. Thus, the Bowen-ratio approach was employed to close the energy balance in order to calculate Q_H and Q_E. When compared to CLASS, the cumulative plots showed an improved fit to the originally measured data. It was then decided to replace the measured Q_H and Q_E with the calculated values as the truth to be used to evaluate CLASS performance.

Although CLASS has presented very good simulation results in the net shortwave radiation, net radiation, sensible heat and latent heat at the Fen site, the practical application of CLASS is still limited in several ways. The principal restriction for CLASS is that the heat transfers between the surface and the air are not modelled well, reflected by the low heat capacity of the surface. The cumulative plots have shown that the net longwave radiation and ground heat fluxes were lower than the expected values, and the sensible heat fluxes were higher by day and lower by night in the diurnal plot. This restriction could be caused by model undesigned surface types, since typical wetland surfaces consist of canopy, bare soil, and open water in varying proportions. The initialization that the LAI was set to 1 for grass was not appropriately applied to partial canopies within a wetland, as LAIs for Fen are really low, about 0.1 - 0.3, not close to unity. The temperature of the third soil layer was uncertain at the beginning. This might affect the distribution of the heat profile between the surface and the soil.

On the other hand, the Penman-Monteith model was not modelling as well as CLASS. It underestimated the evaporation of the total period about 30% of that from

CLASS. This might be because the Penman-Monteith model highly relied on an accurate representative estimate of surface resistance. It is especially advantageous for situations where canopy evaporation is dominant and other sources of evaporation are minimal (Wessel and Rouse, 1994). However, it is difficult to determine canopy resistance for a complex surface, such as lichen and moss tundra, on which little work has been undertaken. Due to a lack of information on site, only employing the function of the canopy resistance for lichens to represent the entire area was not sufficient, and could result in errors in the simulation. Few studies have focused on the canopy resistance for this special region, so not everything is perfectly parameterized or prescribed, but it will give us a place to start.

The Deer River basin was examined using RiverTools to delineate the basin boundary and create the river networks. The generated basin area and streams were quite consistent with the public information from WSC and the NTDB map. Similarity in area, stream overlapping on the map, and few streams crossing the boundary indicated a successful delineation. As for the runoff, the results from CLASS demonstrated that the wetlands were not appropriately modelled for runoff generation, particularly in the extremely flat Churchill region. But this part of thesis provides a good jumping of point for future research.

The lichen and moss tundra at Rail Spur was a special site for our evaporation modelling. Except those problems mentioned above, one cannot deny that the difficulty of assembling reliable data in the subarctic area is a critical reason for occurring discrepancies, as well as broad assumptions. Lacking soil information, vegetation

properties, and certain observations would lead to errors. For CLASS, longwave radiation was the only unmeasured input variable, which was calculated from the modified Efimova-Jacobs combination model. The method associating the degrees of cloud cover with known weather conditions to obtain incoming longwave radiation was the most successful portion of the experiment. The simulation results showed excellent fits of longwave radiation and its cumulative plots to the measurements.

In conclusion, CLASS can successfully model all the components of the energy balance for the wetland sedge Fen site, and can be modified to model evaporation from non-vascular ecosystems. Based on the Rail Spur site, CLASS appears to be better than the Penman-Monteith model in the prediction of evaporation, since the assumption for the initial canopy moisture content in the Penman-Monteith model was not proper for the site, and the Penman-Monteith model set the atmospheric conductance under a neutral condition, which is usually not realistic in natural environments. However, future research of these ecosystems is required to adjust the models further to remove discrepancies between the measured and modelled values. This research project in Churchill, Manitoba, was only the first step to start.

References

Abdella, K. and N. A. Mcfarlane (1996). Parameterization of the surface-layer exchange coefficients for atmospheric models. *Boundary-Layer Meteorology, 80*, 223–248.

Anthoni, P. M., M. Unsworth, B. Law, J. Irvine, D. D. Baldocchi, O. Kolle, A. Knohl and E.-D. Schulze (2002). Comparison of open-path and closed-path eddy covariance system.

Appendix D: CLASS 3.0 template used to create the class.ini initialization file used by WATCLASS. (n.d.). Retrieved July 17, 2006, from http://halfront.wxe.sk.ec.gc.ca/html/documents/store/dataFor_1_0/class_ini.doc

Bailey, W. G., I. R. Saunders and J. D. Bowers (2000). Application of the Canadian Land Surface Scheme to a full canopy crop during a drying cycle. *Atmosphere-Ocean, 38*(1), 57-80.

Bellisario, L. M., L. D. Boudreau, D. L. Verseghy, W. R. Rouse and P. D. Blanken (2000). Comparing the performance of the Canadian land surface scheme (CLASS) for two subarctic terrain types. *Atmosphere-Ocean, 38*(1), 181-204.

Bello, R. (2007). *Personal communication*, e-mail, November 5, and November 8. York University, Toronto, Ontario, Canada.

Blanken, P. D. and W. R. Rouse (1995). Modelling evaporation from a high subarctic willow-birch forest. *International Journal of Climatology, 15*, 97-106.

Boer, G. J., N. A. Mcfarlane, R. Laprise, J. D. Henderson and J.-P. Blanchet (1984). The Canadian Climate Centre spectral atmospheric general circulation model. *Atmosphere-Ocean, 22*(4), 397-429.

Bowen, I. S. (1926). The ratio of heat losses by conduction and by evaporation from any water surface. *Physical Review, 27*, 777-787.

Brutsaert, W. (1975). On a derivable formula for long-wave radiation from clear skies. *Water Resources Research, 11*, 742-744.

Comer, N. T., P. M. Lafleur, N. T. Roulet, M. G. Letts, M. Skarupa and D. Verseghy (2000). A test of the Canadian Land Surface Scheme (CLASS) for a variety of wetland types. *Atmosphere-Ocean, 38*(1), 161-179.

Dickinson, R. E. (1983). Land-surface processes and climate-surface albedos and energy balance. *Advances in Geophysics, 25*, 305-353.

Dickinson, R. E., A. Henderson-Sellers, P. J. Kennedy and M. F. Wilson (1986). Biosphere-Atmosphere Transfer Scheme (BATS) for the NCAR Community Climate Model. National Center for Atmospheric Research, Boulder, Colorado, NCAR/TN-275+STR, 69 pp.

Dingman, S. L. (2002). *Physical hydrology* (2nd ed.). Upper Saddle River, New Jersey: Prentice-Hall, Inc.

Dredge, L. A. (1992). *Field guide to the Churchill region, Manitoba.* Geological Survey of Canada, Miscellaneous Report 53.

Geology.com. (2008). [Canada Satellite Image]. Canada Maps. Retrieved from http://geology.com/world/canada-satellite-image.shtml

Griffis, T. J., W. R. Rouse and J. M. Waddington (2000). Scaling net ecosystem CO_2 exchange from the community to landscape-level at a subarctic fen. *Global Change Biology, 6*, 459-473.

Hamon, R. W. (1963). Computation of direct runoff amounts from storm rainfall. *International Association of Scientific Hydrology Publication No. 63.* Wallingford, Oxon., U.K.

Hanesiak, J. M., D. G. Barber, T. N. Papakyriakou and P. J. Minnett (2001). Parametrization schemes of incident radiation in the north water polynya. *Atmosphere-Ocean, 39*(3), 223-238.

Hansell, R. I. C., P. A. Scott, R. Staniforth and J. Svoboda (1983). Permafrost development in the intertidal zone at Churchill, Manitoba: A possible mechanism for accelerated beach uplift. *Arctic, 36*, 198-203.

Hutchinson, M. F. (2006). *ANUDEM version 5.2 user guide.* Centre for Resource and Environmental Studies, Australian National University, Canberra.

Kattenberg, A., F. Giorgi, H. Grassl, G. A. Meehl, J. F. B. Mitchell, R. Stouffer, T. Tokioka, A. Weaver and T. M. L. Wigley (1996). Climate Models Projection of future climate. In J. T. Houghton, L. M. Filho, B. Callander and N. Harris (Eds.), *Climate Change 1995, The Science of Climate Change* (pp. 285- 357). New York: Cambridge University Press.

Kinner, D. A. (2000). Delineation and characterization of the Boulder Creek watershed and its sub-watersheds. In *Comprehensive water quality of the Boulder Creek watershed, Colorado, during high-flow and low-flow conditions* (Chapter 2). Retrieved April 9, 2008, from http://wwwbrr.cr.usgs.gov/projects/SWC_Boulder_Watershed/WRIR_Chapter2.pdf

Kohler, M. A., T. J. Nordenson and W. E. Fox (1955). Evaporation from pans and lakes. *U.S. Weather Bureau Research Paper 38.* Washington, DC.

Kustas, W. P., A. Rango and R. Uijlenhoet (1994). A simple energy budget algorithm for the snowmelt runoff model. *Water Resources Research, 30*, 1515-1527.

Lee, T. J. and R. A. Pielke (1992). Estimating the soil surface specific humidity. *Journal of Applied Meteorology, 31*, 480-484.

Letts, M. G., N. T. Roulet and N. T. Comer (2000). Parametrization of peatland hydraulic properties for the Canadian Land Surface Scheme. *Atmosphere-Ocean, 38*(1), 141-160.

Linsley, R. K., M. A. Kohler and J. L. H. Paulhus (1982). *Hydrology for Engineers* (3rd ed.). New York, NY: McGraw-Hill Book Co.

Liu, S. (1997). A new model for the prediction of rainfall interception in forest canopies. *Ecological Modelling, 99*, 151-159.

Loukili, Y., A. D. Woodbury and K. R. Snelgrove (2006). Proceedings from 2006 AGU Fall Meeting: *AccuCLASS - an enhancement of the Canadian Land Surface Scheme for climate assessment over the Prairies.* San Francisco, CA.

Malmstrom, V. H. (1969). A new approach to the classification of climate. *Journal of Geography, 68*, 351-357.

Manabe, S. (1969). Climate and ocean circulation. I. The atmospheric circulation and the hydrology of the earth's surface. *Monthly Weather Review, 97*, 739 774.

Monteith, J. L. (1965). Evaporation and environment. *Proceedings of the 19th Symposium of the Society for Experimental Biology* (pp. 205-233). New York: Cambridge University Press.

Mortsch, L. (Ed.). (1990). Eastern Canadian Boreal and Subarctic wetlands: a Resource Document. *Climatological Studies No. 22*, Atmospheric Environment Service, Environment Canada. 169 pp.

National Climate Data and Information Archive. (2004, January 21). *Climate data online: Churchill, Manitoba*. Environment Canada's World Wide Web Site. Retrieved May 21, 2008, from http://www.climate.weatheroffice.ec.gc.ca/climateData/hourlydata_e.html?timeframe=1&Prov_MB&StationID=3871&Year=2008&Month=5&Day_20

Oke, T. R. (1987). *Boundary layer climates* (2nd ed.). Cambridge, Great Britain: University Press.

Papakyriakou, T. N. (n.d.). *The Hudson Bay Coastal Zone in a Changing Climate System*. Retrieved February 27, 2008, from http://www.arcticnetulaval.ca/index.php?fa=ResearchHome.showThemeProjects&theme=14&project_id=15&page=1

Penman, H. L. (1948). Natural evaporation from open water, bare soil and grass. *Proceedings of the Royal Society of London, Series A, 193*, 120-145.

Rizzo, B. and E. Wiken (1992). Assessing the sensitivity of Canada's ecosystems to climatic change. *Climatic Change, 21*, 37-55.

Roulet, N. T. and M.-K. Woo (1988). Runoff generation in a low arctic drainage basin. *Journal of hydrology, 101*, 213-226.

Rouse, W. R. (1998). A water balance model for a subarctic sedge fen and its application to climatic change. *Climatic Change, 38*, 207-234.

Rouse, W. R., M. S. V. Douglas, R. E. Hecky, A. E. Hershey, G. W. Kling, L. Lesack, P. Marsh, M. Mcdonald, B. J. Nicholson, N. T. Roulet and J. P. Smol (1997). Effects of climate change on the freshwaters of Arctic and subarctic North America. *Hydrological Processes, 11*, 873–902.

Sellers, P. J., Y. Mintz, Y. C. Sud and A. Dalcher. (1986). A simple biosphere model (SiB) for use within general circulation models. *Journal of Atmospheric Sciences, 43*, 505–531.

Shiklomanov, I. A. and A. A. Sokolov (1983). Methodological basis of world water balance investigation and computation. In *New Approaches in Water Balance Computations*. International Association for Hydrological Sciences Publication, No. 148. (Proceedings of the Hamburg Symposium).

Slatyer, R. O. and I. C. McIlroy (1961). *Practical Microclimatology*. Melbourne, Australia: CSIRO.

Snelgrove, K. R. (2002). Implications of lateral flow generation on Land-Surface Scheme fluxes (Ph. D. thesis, University of Waterloo, 2002). Waterloo, Ontario, Canada.

Swystun, K. (2008). *Personal communication*, e-mail, July 11 and July 16. University of Manitoba, Winnipeg, Manitoba, Canada.

Tarnocai, C. (1980). Canadian Wetland Registry. In C. D. A. Rebec and F.C. Pollett (Eds.), *Proc. Workshop on Canadian Wetlands* (pp. 9-39). Lands Directorate, Environment Canada. Ecological Land Classification Series No. 12. Ottawa, Ontario.

Thornthwaite, C. W. (1948). An approach toward a rational classification of climate. *Geographical Review, 38*, 55-94.

Vakkilainen, P. and T. Karvonen (2005, February 22). Leaf energy and water balance penman-monteith equation for calculating potential evapotranspiration rate. In *Influence of global climatic change on different hydrological variables* (Evapotranspiration). Retrieved August 24, 2007, from Helsinki University of Technology, Water Resources Engineering Web site: http://www.water.tkk.fi/wr/kurssit/Yhd-12.135/kirja/evapo.htm

Verseghy, D. L. (1991). CLASS—A Canadian land surface scheme for GCMs. I. Soil model. *International Journal of Climatology, 11*, 111-133.

Verseghy, D. L., N. A. McFarlane and M. Lazare (1993). CLASS—A Canadian land surface scheme for GCMs, II. Vegetation model and coupled runs. *International Journal of Climatology, 13*, 347-370.

Verseghy, D. L. (2000). The Canadian Land Surface Scheme (CLASS): its history and future. *Atmosphere-Ocean, 38*(1), 1-13.

Verseghy, D. L. (2008). *The Canadian Land Surface Scheme: technical documentation version 3.4*. Climate Research Division, Science and Technology Branch, Environment Canada.

Water Survey of Canada (2007, July 3). *Archived hydrometric data: deer river north of belcher*. Environment Canada's World Wide Web Site. Retrieved April 2, 2008, from http://www.wsc.ec.gc.ca/hydat/H2O/index_e.cfm?cname=graph.cfm&RequestTimeout=300

Wessel, D. A. and W. R. Rouse (1994). Modelling evaporation from wetland tundra. *Boundary-Layer Meteorology, 68*, 109-130.

Appendix A: CLASS Sample Data

Input datasets and format required by CLASS.

hour	min	day	year	$K_{\downarrow}$	$L_{\downarrow}$	rain	T_a	q	v_a	p
0	0	148	2007	0.00	320.70	0.0000E+00	0.84	3.811E-03	6.79	100300.00
0	30	148	2007	0.00	318.00	0.0000E+00	0.63	3.750E-03	6.85	100400.00
1	0	148	2007	0.00	315.90	0.0000E+00	0.42	3.693E-03	6.59	100400.00
1	30	148	2007	0.00	314.80	0.0000E+00	0.27	3.656E-03	6.71	100500.00
2	0	148	2007	0.00	315.80	0.0000E+00	0.19	3.644E-03	6.56	100500.00
2	30	148	2007	0.00	315.80	0.0000E+00	0.13	3.630E-03	6.98	100500.00
3	0	148	2007	0.00	315.60	0.0000E+00	0.12	3.604E-03	7.39	100600.00
3	30	148	2007	0.65	315.40	0.0000E+00	0.23	3.560E-03	7.09	100700.00
4	0	148	2007	6.27	315.40	0.0000E+00	0.23	3.532E-03	7.43	100700.00
4	30	148	2007	17.18	314.50	0.0000E+00	0.21	3.442E-03	7.73	100800.00
5	0	148	2007	26.37	314.00	0.0000E+00	0.19	3.418E-03	6.91	100900.00
5	30	148	2007	51.53	312.40	0.0000E+00	-0.03	3.361E-03	7.44	100800.00
6	0	148	2007	57.96	312.50	0.0000E+00	-0.29	3.358E-03	7.69	100900.00
6	30	148	2007	81.80	311.00	0.0000E+00	-0.57	3.303E-03	7.57	100900.00
7	0	148	2007	91.20	310.80	0.0000E+00	-0.52	3.165E-03	7.84	101000.00
7	30	148	2007	44.14	310.70	0.0000E+00	-0.69	3.100E-03	6.85	101100.00
8	0	148	2007	57.71	308.70	0.0000E+00	-1.08	3.049E-03	7.46	101200.00
8	30	148	2007	77.97	307.00	0.0000E+00	-1.34	2.966E-03	7.41	101200.00
9	0	148	2007	82.20	306.10	0.0000E+00	-1.55	2.932E-03	7.09	101300.00
9	30	148	2007	58.70	305.60	0.0000E+00	-1.81	2.892E-03	7.57	101300.00
10	0	148	2007	89.50	303.80	0.0000E+00	-2.26	2.841E-03	7.95	101300.00
10	30	148	2007	101.90	302.60	0.0000E+00	-2.57	2.792E-03	7.34	101400.00

Sample data cover 10 hours from Fen 2007 modelling. Symbols have the same meaning as those in the text. The units are W m^{-2} for $K_{\downarrow}$ and $L_{\downarrow}$, mm s^{-1} for rain, °C for T_a, dimensionless for q, m s^{-1} for v_a, and Pa for p.

Appendix B: Soil Temperature Figures

Comparative figures of soil temperatures at the surface, 5 cm, 25 cm, and 55 cm down from the surface, for Fen 2007.

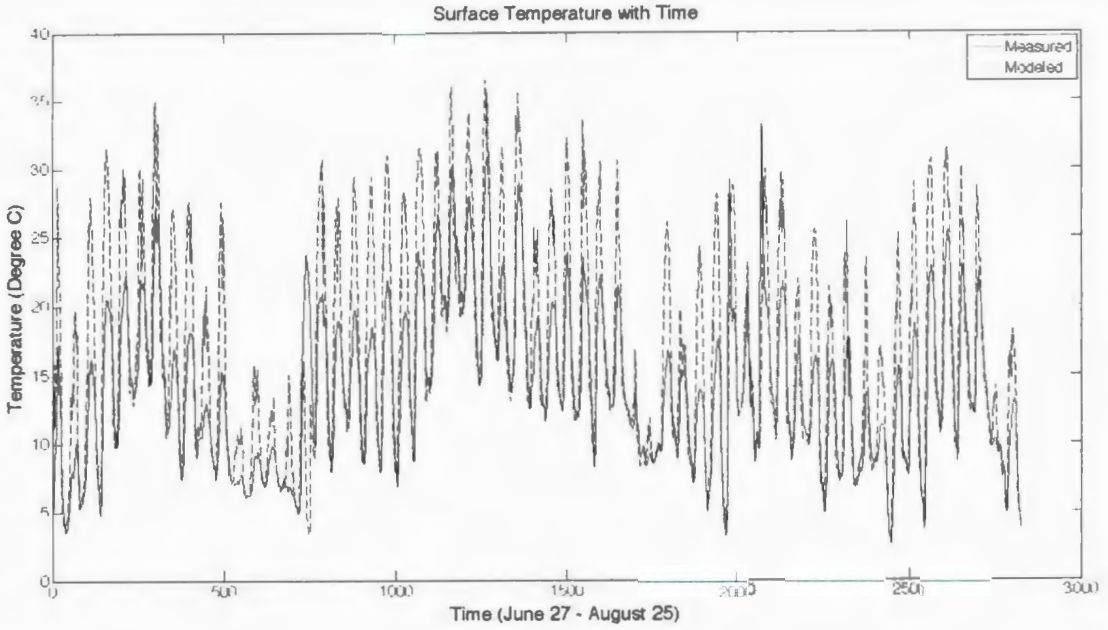

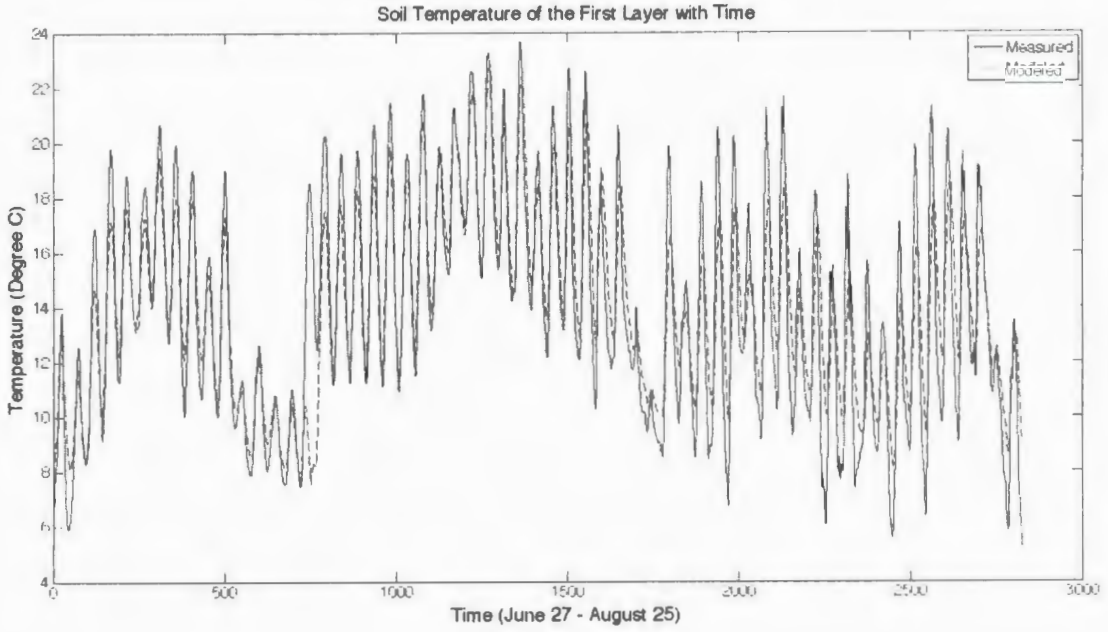

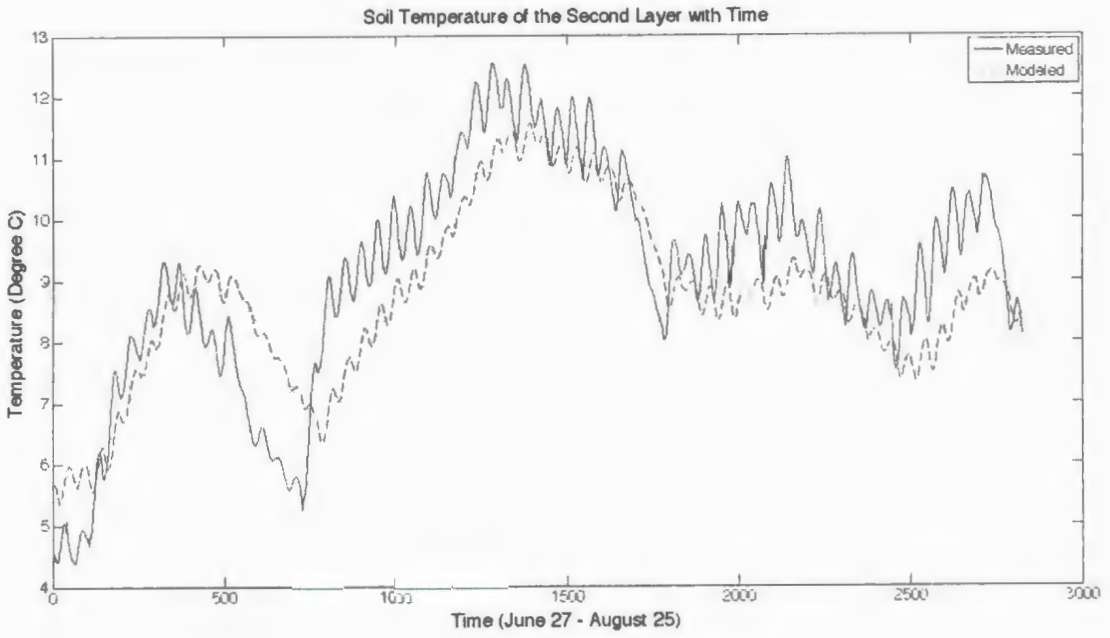

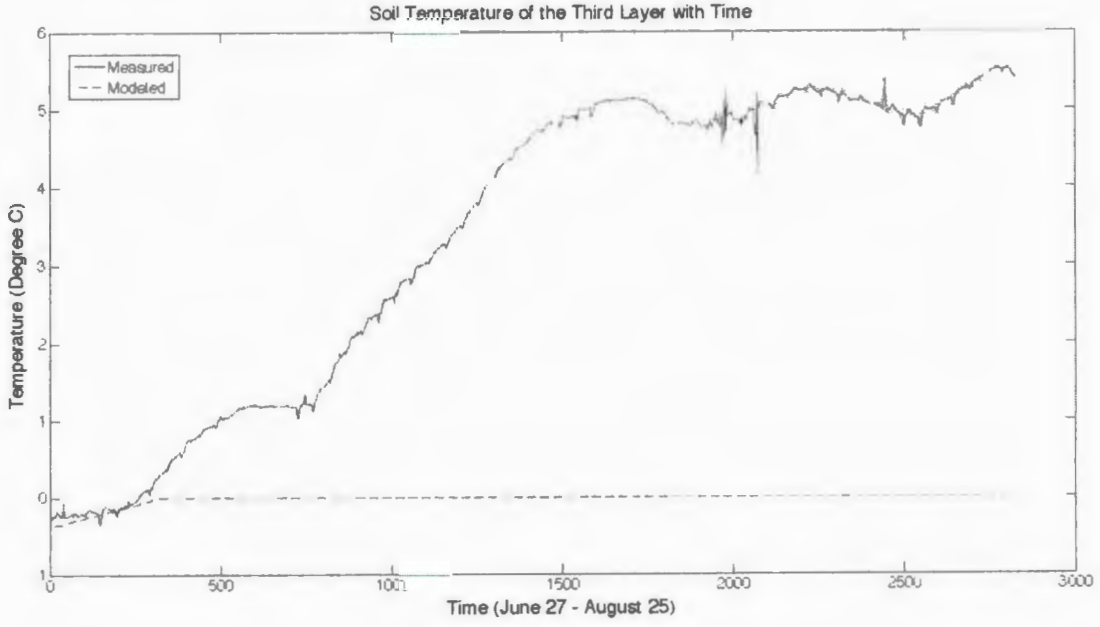

Note that the measured (55cm) and modelled (2.225m) depth of the third soil layer was not the same, so that the temperatures were not matching in the last figure.